universität wien

MASTERARBEIT

Titel der Masterarbeit

„Beams of high-mass organic molecules for matter-wave interferometry “

Verfasser

Uğur Sezer, BSc

angestrebter akademischer Grad

Master of Science (MSc)

Wien, 2014

Studienkennzahl lt. Studienblatt:	A 066876
Studienrichtung lt. Studienblatt:	Masterstudium Physik
Betreuerin / Betreuer:	Univ. Prof. Dr. Markus Arndt

I have tried to provide the information about the owner of pictures and figures in this thesis and obtained their approval. In the case of copyright infringement I ask you kindly for your declaration.

Ich habe mich bemüht, sämtliche Inhaber der Bildrechte ausfindig zu machen und ihre Zustimmung zur Verwendung der Bilder in dieser Arbeit eingeholt. Sollte dennoch eine Urheberrechtsverletzung bekannt werden, ersuche ich um Meldung bei mir.

This work is dedicated to my grandfather.
”The world is a cake. You just have to take one piece....”
Rıza Sezer

Acknowledgements

Mentioning a list of names on a sheet of paper is of course not enough to express my gratitude. However, throughout the years the section ”acknowledgements” has become a component of each thesis which no one can abandon. Hence, I don′t want to be an exception.
With these introductory words, I want to thank my family for their love and support. In particular I want to express my gratitude to my father who never stopped to motivate me for studying physics. This has been of upmost importance for me, as physics with all its beauty and power is not accepted and even not known as a profession in my familiar environment. Thus studying physics, working in a resarch group with high reputation and beeing more or less successful as a scientist has not only been my personal goal but also an important contribution to the culture and society in which I grew up.
Furthermore I want to express my thanks to my supervisor, Prof. Markus Arndt, not only for giving me the opportunity to work in his highly motivated and gifted research group, but also teaching me the scientific way of thinking, performing experiments and even writing. Equally I thank my laboratory colleague, Philipp Schmid, who hast not only shown the necessary amount of patience and gentleness in explaining me all the things an experimentator needs to know but who also has become a valuable personal friend.
Here also Lukas Felix and Prof. Mayor should be mentioned to whom I want to thank not only because they have synthesized the molecules which are the main subject of this work but also for their patience and endurance explaining chemistry to physicists.
Additionally, I want to express my gratitude to all my other colleagues, especially Christian Brand for proof-reading this manuscript, Joseph Cotter for his help in the analysis of some parts of the data and Jonas Rodewald for his productive contributions in our discussions.
Last but not least I want to emphasize my special thanks to Jofre Espigule Pons, Jana Hofer and Xiaxi Cheng for sharing the funny moments in my life. They have reminded me again and again of having a private life parallel to all these hours I have spent in the laboratory.

Abstract

The wave particle duality of light is one of the most exciting but at the same time also one of the most incomprehensible models in physics. In many textbooks it serves as an introduction to the spectacular world of quantum physics. For a long time, light was believed to be best described by the wave model until the photoelectric effect was well explained by a corpuscular theory through Einstein [1]. The simultaneous existence of these two models revolutionized the physical view of nature and surprised many scientists. However, besides that also de Broglie caused for a sensation by publishing his work in 1924. To each particle with a mass m and a center of mass velocity v, de Broglie assigned a wavelength $\lambda_{dB} = h/(m \cdot v)$ with h representing Planck′s constant [2]. Since 1924 many attempts have been made for proving the wave nature of massive and complex particles [3]. With the help of matter wave interferometry, the quantum nature of particles exceeding 10000 Da with more than 800 atoms has been shown [4]. These experiments explore the intriguing question whether there exists a boundary between the quantum and the classical world. This question is also motivated in particular by the incompatibility of general relativity with quantum theory. Further progress now requires designing heavier molecules and also new methods and techniques for the intact volatilization of heavy particles. This is in particular important for interference experiments, as interferometers impose many restrictions to the source. These include an intense and intact molecular beam with a low longitudinal and transversal velocity as this influences the de Broglie wavelength. Additionally strict longitudinal and transversal coherence criterions have to be fulfilled. Furthermore a high detection efficiency has to be guaranteed. Keeping these requirements in mind, colleagues around the chemist Prof. Marcel Mayor in Basel designed a new class of flourinated molecular libraries as perfluoroalkylated particles tend to show a higher volatility and robustness upon laser induced fragmentation. Here the word *library* describes molecules which posses a well defined core but a distribution of the number of attached fluorinated chains. Hence this leads to a mass distribution. First, library 1, a tetramer of Zinc Tetraphenylporpyhrins (TPP), with a most abundant mass of 11676 Da is discussed. Then library 2, a pentamer of TPPs with more than 40 attached perfluoroalkyl side chains building up a mass of 22152 Da is described in detail [5]. For testing the suitability of these molecules for matter-wave interferometry we have designed an automated set up and a dedicated analysis software. The heart of the experiment is a customized linear time of flight (ToF) mass spectrometer for the detection of single molecules. Laser desorption with 157 nm photoionization and subsequent ToF-detection of these particles led to mass spectra which prove the volatility and photoionizability [6]. Library 2 with a mass of up to 25000 Da represents currently the world largest photoionisable organic molecule. Increasing the mass of the interfering object requires a reduction of the forward velocity in order to resolve the de Broglie wavelength in current interferometers. For that reason we recorded the characteristic velocity distributions of the aforementioned molecules. For the most probable velocity of the molecular beam we get approximately 90 m/s for library 1 and 45 m/s for the second molecular library with a still intense tail reaching even down to 20 m/s. These values suggest a successful implementation into existing matter-wave interferometers such as the optical time domain matter-wave interferometer (OTIMA) [7] or the Kapitza-Dirac-Talbot-Lau interferometer (KDTLI) [8]. Apart from that, the efficiency for photoionization for both of the libraries was determined. This was done by recording the molecular signal intensity while the ionization laser energy was varied. Here we observed that for library 1 as well as for library 2 saturation of the molecular count rate is reached which indicates high detection efficiency.

These results show the suitability of both molecular libraries for OTIMA. Although these molecules seem to exhibit the proper stability, velocity and detection efficiency, further effort in increasing the overall signal intensity is needed. One parameter for the optimization is the desorption laser power. Thus, we started with the characterization of the signal yield with respect to the desorption laser energy and found interesting differences in the volatility and dissociation behaviour between library 1 and 2. Finally, I conducted first experiments on the characterization of the plume dynamics.

Zusammenfassung

Der Welle-Teilchen-Dualismus von Licht ist eines der aufregendsten und zugleich auch eines der unverständlichsten Modelle in der Physik. In vielen Lehrbüchern wird dieses Modell zur Einführung in die spektakuläre Natur der Quantenmechanik präsentiert. Lange Zeit glaubte man das Phänomen des Lichts am besten durch das Wellenmodel erklären zu können bis der photoelektrische Effekt durch Einstein anhand des Teilchencharakters des Lichts beschrieben wurde [1]. Die gleichzeitige Existenz dieser beiden Modelle revulutionierte die Weltanschauung in der Physik und führte zum Erstaunen vieler WissenschaftlerInnen. Für ein weiteres Aufsehen sorgte de Broglie als er seine Dissertation im Jahre 1924 veröffentlichte. In dieser Arbeit ordnete de Broglie jedem Teilchen einer Masse m und einer Schwerpunktsgeschwindigkeit v eine Wellenlänge λ_{dB} zu: $\lambda_{dB} = h/(m \cdot v)$ mit h der Planckschen Konstante [2]. Seit 1924 gab es und gibt es immer mehr Versuche das Verhalten von massiven und komplexen Teilchen mit dem Wellenmodell zu erklären. Mit der Hilfe von Materiewelleninterferometern gelang es kürzlich die Quanten-Delokalisierung von organischen Molekülen oberhalb von 10000 Da und mit mehr als 800 Atomen zu zeigen [4]. Diese Experimente untersuchen die Frage, ob es eine natürliche Grenze zwischen der klassischen Physik und der Quantenmechanik gibt. Diese Frage ist insbesondere durch die Inkompatibilität der algemeinen Relativitätstheorie mit der Quantentheorie motiviert. Um weiteren Fortschritt zu erzielen, ist die Synthese von neuartigen schwereren Molekülen und die Entwicklung und Entwurf von neuen Technologien zu deren Volatiliserung von Nöten. Letzteres ist insbesondere für Interferenzexperimente von essentieller Bedeutung, da diese eine Vielzahl von Anforderungen an Molekülquellen haben. Diese sind beispielsweise die Erzeugung eines intensiven und intakten Molekülstrahls mit einer ausreichend geringen longitudinalen und transversalen Geschwindigkeit, da diese die de Broglie Wellenlänge beeinflusst. Hinzu kommen strikte sowohl longitudinale als auch transversale Kohärenzbedingungen. Außerdem verlangt man eine hohe Detektionseffizienz. Unter Berücksichtigung all dieser Anforderung haben Kollegen um den Chemiker Prof. Marcel Mayor in Basel eine neue Klasse von organischen flourierten Molekularbibliotheken synthetisiert, da perfluoroalkylierte Teilchen eine erhöhte Volatiliserbarkeit mit gleichzeitiger Robustheit gegenüber Fragmentierung aufweisen. In diesem Zusammenhang bedeutet das Wort *Bibliothek* nichts anderes als die Tatsache, dass die synthetisieren Moleküle zwar immer den gleichen Kern aber eine unterschiedliche Anzahl von angehängten perfluoroalkylierten Seitenketten haben. Diese Zahl führt zu einer Massenverteilung. Als erstes, wird die Molekülbibliothek 1 bestehend aus einem Tetramer aus Zink Tetraphenylporphyrinen (TPP) mit einer wahrscheinlichen Masse von 11676 Da beschrieben. Im darauffolgenden Abschnitt wird die zweite Molekülbibliothek diskutiert. Sie besteht aus einem Pentamer aus TPP an die mehr als 40 perfluoroalkylierte Seitenketten angehängt sind, sodass eine Molekülmasse von 22152 Da erreicht wird. Um die Eignung dieser Moleküle für die existierenden Interferometer zu testen, wurde eine automatisierte Quellen-Testapparatur aufgebaut und eine Software zur Datenanalyse geschrieben. Der Kernbestandteil dieses Experiments ist ein linearer Flugzeitmassenspektrometer (ToF), welcher zur Detektion von einzelnen Molekülen verwendet wurde. Laser Desorption mit anschließender Photoionisation mit 157 nm Licht und der darauffolgenden ToF-Detektion führten zu Massenspektren welche bereits die Volatiliserbarkeit und die Photoionisierbarkeit beweisen [6]. Die Molekularbibliothek 2 mit einer Masse von bis zu 25000 Da repräsentiert zur Zeit das weltweit größte photoionisierbare Molekül.

Erhöhung der Masse im Interferometer ist aber unmittelbar mit der Reduktion der Vorwärtsgeschwindigkeit des Molekülstrahls verbunden, um die Auflösung der de Broglie Wellenlänge in bereits existierenden Materiewelleninterferometern zu gewährleisten. Deshalb wurden Geschwindigkeitsverteilungen der erwähnten Bibliotheken aufgenommen. Das Resultat für die wahrscheinlichen Geschwindigkeiten des Strahls sind 90 m/s für die Molekülbibliothek 1 und 45 m/s für die zweite, wobei signifikante Intensitäten noch bei 20 m/s detektiert wurden. All diese Werte suggerieren eine erfolgreiche Verwendung der Moleküle in existierenden Interferometern wie zum Beispiel im Interferometer mit Lichtgittern in der Zeitdomäne (OTIMA) [7] und im Kapitza-Dirac-Talbot-Lau Interferometer (KDTLI) [8]. Im Anschluss daran werden die Studien zur Effizienz der Photoionisierbarkeit für beide Molekularbibliotheken diskutiert, welche durch die Aufnahme der Signalintensität als Funktion der Laserenergie ermittelt werden kann. Von diesen Daten konnte herausgefolgert werden, dass Sättigung für beide Bibliotheken vorliegt, was ein Indiz für eine ausreichend hohe Detektionseffizienz ist. Das Vorliegen der Sättigung ist auch ein notwendiges Kriterium für die erfolgreiche Funktionsweise der Lichtgitter im OTIMA. Obwohl all die bisher aufgelisteten Eigenschaften für eine unmittelbare Eignung für die Interferometer sprechen, sind Bemühungen zur Anhebung der Signalintensitäten von außerordentlicher Bedeutung. Ein wichtiger Parameter hierfür ist die Desorptionslaserenergie. Deshalb sind Studien zur Abhängigkeit zwischen der Molekülstrahlintensität und der Desorptionsenergie unternommen wurden, wobei interessante Unterschiede in der Volatilisierbarkeit und Dissoziation zwischen den Molekülbibliotheken beobachtet wurden. Zum Abschluss werden schnelle Experimente und deren Resultate zur Untersuchung der Expansionsdynamik des Molekülstrahls präsentiert.

Contents

Chapter 1

Introduction

> *At the heart of quantum mechanics lies the superposition principle.*
>
> P. Dirac, *1902-1984*

In quantum mechanics the state of an object is described by a wave function $|\psi\rangle$ which contains all the information about the pure system. The superposition principle now claims that the complex superposition $c_1 \cdot |\psi_1\rangle + c_2 \cdot |\psi_2\rangle$ of the two Eigenstates $|\psi_1\rangle$ and $|\psi_2\rangle$ is again an Eigenstate of the same Hamiltonian. This is a fundamental axiom of quantum mechanics. Everything should obey this superposition principle. However, this seems not to be consistent with our every-day observation of the classical world. One may attribute this to decoherence theory, according to which a system apparantly loses its quantum nature if it is strongly coupled to a complex environment [9]. On the other hand, one may also speculate about a possible boundary beyond which the unitary quantum mechanical description of physical reality fails [10]. This statement is additionally motivated by the incompatibility of general relativity with quantum theory. There are many experimental approaches to establish macroscopic superposition states in order to test whether there is a limitation to quantum theory.

Superconducting quantum interference devices (SQUIDs) forming a quantum state with up to 10^{14} electrons [11], neutron interferometry providing the biggest separation of the quantum wave packet (7 cm) [12] and atom interferometry in which a coherence time of more than 2 seconds [13] and a beam separation of $102\hbar k$ [14] was realized are just some of the examples to establish macroscopic superposition states [10]. In order to compare all these experiments to each other with respect to their macroscopicity, a measure μ quantifying the degree of macroscopicity of a superposition state has even been introduced [15, 10]. For better understanding of μ, I refer the reader to the work of Nimmrichter et al. [15]. The same authors calculated the macroscopicity for different experimental approaches and concluded that matter wave interferometry with high masses has the potential to reach high values for μ. Recently, organic molecules consisting of more than 800 atoms could be successfully delocalized and the characteristic interference pattern was recorded with high visibility [4]. However, in order to increase macroscopic superposition states, heavier molecules are needed. The difficult task is to design new high mass molecules which satisfy the criteria of existing interferometers. Among them, soft volatilization of neutral molecules with sufficient low transversal and longitudinal velocities is a prerequisite for quantum interference experiments. In addition to that high photoionization efficiencies are also needed if new interferometer concepts should be used. OTIMA, the optical time domain matter wave interferometry is an example of hereof [7]. In company to that the development and characterization of new molecular sources is of essential importance.

In this work we describe the properties of two tailor-made molecular libraries of up to 25000 Da. We generate and characterize the respective molecular beams. Here the word *library* implies a mixture of molecules with the same central unit but with different number of attached perfluoroalkylated side chains. This results in a mass distribution. The library approach is scalable to higher masses in the future. Apart of that, the development of new volatilization methods also leads to the investigation of a new class of biologically relevant molecules, e.g. peptides and proteins.

Future explorations between the classical and quantum regime may require matter wave experiments with objects in the mass range of $10^7 - 10^9$ Da. For this mass range nanoparticles are very suitable. A proper launching and cooling mechanism in this mass regime has recently been developed by our group [16].

Chapter 2

Theory

> *All theory is gray, my friend. But forever green is the tree of life.*
>
> J. W. Goethe, *1749-1832*

2.1 Matter Wave Interferometry

The occurrence of interference phenomena with light can only be explained by a wave model. Many experiments, especially the double slit experiment of Thomas Young, showed that the interference phenomenon is based on the wave model [17]. Later double-slit experiments with electrons showed that the interference phenomenon is a single particle event. This observation, however, was a strong indication for the corpuscular theory of light explained by P. Lenard in 1902. A simultaneous existence of two concepts, wave and particle, was proposed to describe light [1]. A new ground-breaking hypothesis revolutionized the physical understanding of matter: Luis de Broglie′s concept of matter waves in 1923, which also became the cornerstone in Schrödinger′s wave mechanics (1926) [2].

2.1.1 Matter Waves

De Broglie started by relating the rest energy of a particle and the energy of an oscillatory phenomenon. Calculations then yields the de Broglie wavelength (see equation 2.1).

This shows that every matter particle with mass m and a center of mass velocity v is associated with a certain wavelength λ_{dB}.

$$\lambda_{dB} = \frac{h}{p} = \frac{h}{m \cdot v} \tag{2.1}$$

Here h denotes Planck′s constant. It can be seen that an increase in mass decreases the de Broglie wavelength as long as the velocity of the particle is not reduced by the same amount. Only a few years after Louis de Brolgie′s discovery, his conjecture was experimentally proven. First, the theory was applied to electron diffraction experiments of Davisson and Germer [3] but later also to neutron [18] and atom interferometers [19]. Then many other matter wave experiments have been conducted with even more complex particles, like with SF_6 in 1981 [20] or with metastable helium [21]. Interferometry with hot molecules started with the diffraction of C_{60} [22] and recently the interference of organic molecules exceeding 10000 Da was shown [8, 23–27, 4].

2.1.2 From far field diffraction to near-field interferometry: the Talbot-Lau effect

Analogous to classical optics, matter wave interferometers can be separated into two categories: those that operate in the far-field regime and those that operate in the near field. The difference between far field and near field interferometers can be well understood if one considers the Kirchhoff-Fresnel integral [28], which describes the diffraction pattern at the screen. The integral explains the pattern by regarding spherical waves created by each points in the aperture. At large distances of the screen with respect to the size of the aperture, the curvature of the spherical waves can be neglected [28]. This describes the far field. So in the far field, the detector is placed far away from the diffraction element, which is a material grating in our case. Here the resulting interference pattern can be well described by the ratio of the wavelength and the grating constant d ($sin(\theta) = \lambda_{dB}/d$). The main drawback of far-field experiments is the molecular source, as the source requirements are quite strict. For a well separated interference pattern one needs a tightly collimated molecular beam [28]. A solution to this problem is the Talbot-Lau concept. This is a near-field phenomenon, in which the curvature of the spherical waves are needed in the Kirchhoff-Fresnel integral.

It was first Henry Fox Talbot [29] who discovered that illumination of a diffraction element with periodicity d through planar waves leads to a coherent self-image of the grating at integers of the Talbot length l_T:

$$l_T = \frac{d^2}{\lambda_{dB}} \tag{2.2}$$

The intensity pattern behind a periodic mask, illuminated by a plane wave is illustrated in figure 2.1. Such Talbot carpets can be readily reproduced in the lab [30]. Here it is noteworthy that at rational multiples of the Talbot length, also the periodicity of the diffraction pattern changes accordingly. At odd integers of l_T, the pattern is shifted by half of the grating constant d. Lau′s contribution to the Talbot-Lau effect was the discovery that self-imaging

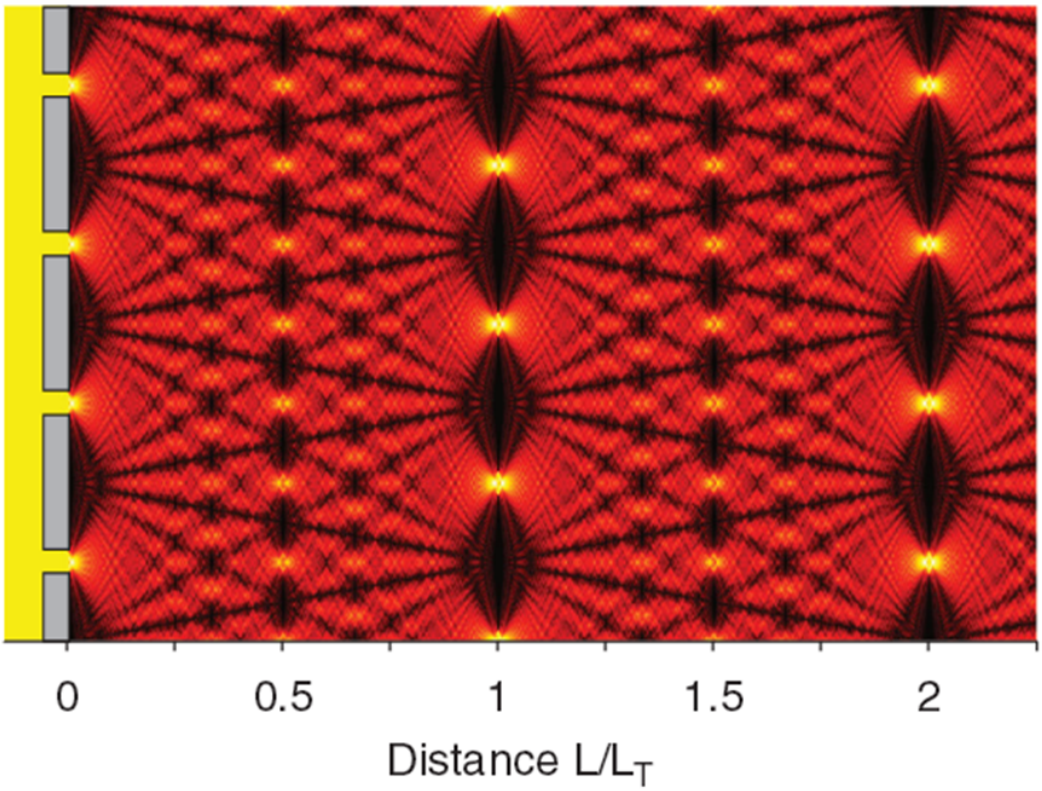

Figure 2.1: The Talbot carpet resulting from the illumination of a grating with periodicity d by planar waves. At multiples of the Talbot length (see equation 2.2), the structure of the grating is reoccuring. Fractional Talbot order leads to the formation of a diffraction pattern with distinct periodicity. [1]

of a grating can even be realized with non-planar waves. This is done through the insertion of an array of point source before the diffractive grating. As the slit openings can be thought of an ensemble of point sources, the incoming light induces multiples of cylindrical waves similar to Huygens′ principle [31].

[1] Figure was taken from ref. [28]

2.1.3 The principle of near-field interferometers

In the interferometry the first grating is used to prepare transverse coherence of the molecular beam. This can be understood with the help of Heisenberg′s uncertainty principle. As the grating acts as a spatial restriction to the wave function of each molecule, the uncertainty in its transverse momentum increases. This expansion of the wave function establishes transverse coherence at grating 2. The second grating is the diffraction grating, after which the matter-wave interference leads to the formation of a periodic particle pattern. This pattern is typically visualized by detecting particles behind a scanning third grating. All the gratings have the same periodicity d.

2.1.4 Matter-wave interferometers

In this section I want to briefly describe the near field matter-wave interferometers which are currently running in our research group to motivate the source requirements that are at the heart of my master thesis. Figure 2.2 shows the Kapitza-Dirac-Talbot-Lau Interferometer

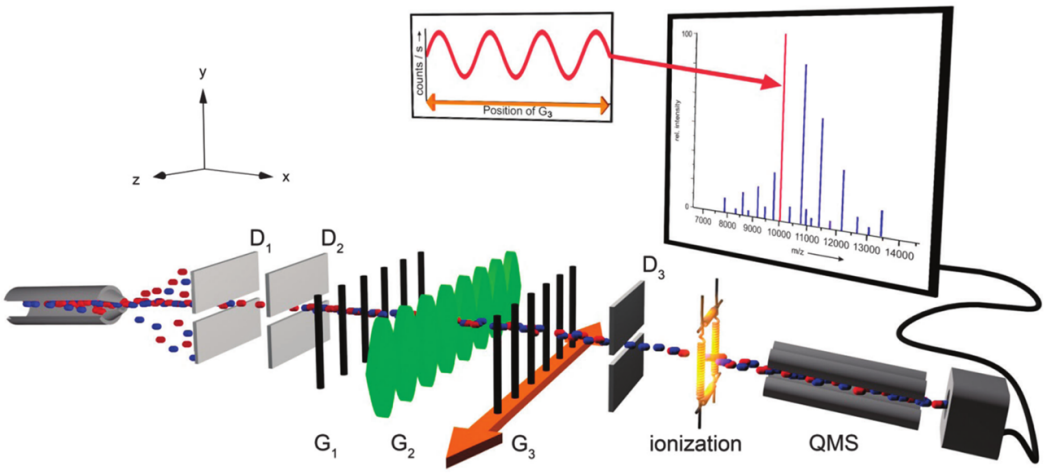

Figure 2.2: The general setup of the Kapitza-Dirac-Talbot-Lau Interferometry. The left, a molecular beam is generated in an oven and enters the interferometry. Here the molecular cloud has to pass two material gratings and one standing light wave. Through the movement of the last grating, the interference pattern is recorded whereas the particles are ionized and detected through a Quadrupole Mass Spectrometer (QMS). [2]

(KDTLI). The molecules are evaporated in an oven. This produces an intense ($2 \cdot 10^{15}$ particles per second) and slow beam ($85\ m/s$) for the interferometry [4].

[2] Figure was taken from ref. [4]

Three slits define a flight parabola for the molecular beam and represent a gravitational velocity selection. In KDTLI the second grating is a light grating. The high constrast periodic molecular intensity distribution is scanned through the movement of the third grating. The particles are ionized and analysed by a quadruple mass spectrometer (figure 2.2).

Optical time domain matter-wave interferometry (OTIMA)

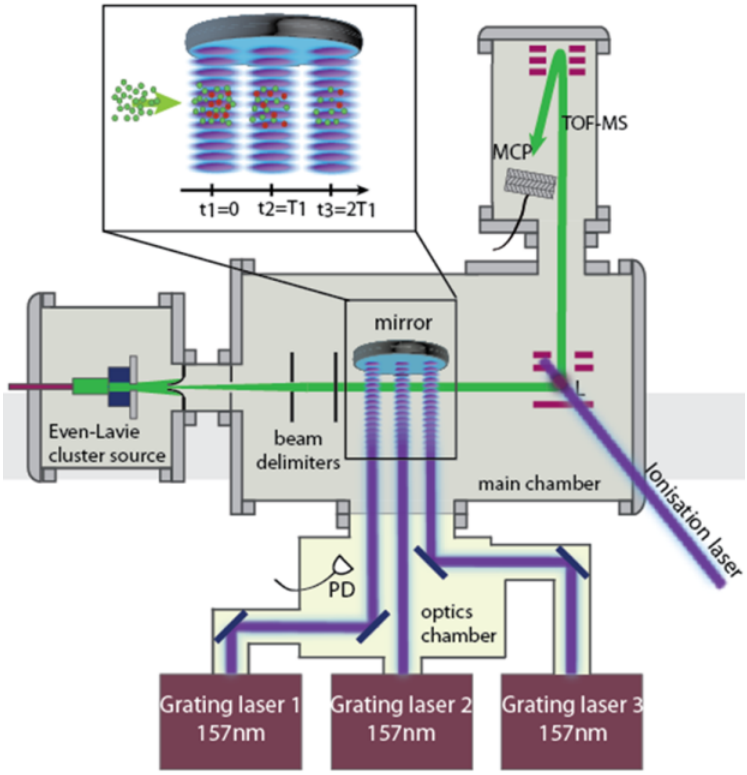

Figure 2.3: The experimental setup of the optical time domain matter-wave interferometer (OTIMA) [7]. Molecules are ejected into vacuum via supersonic expansion. The beam height and width is adjusted to the standing light waves, which are formed through back reflection of the grating laser beams. The structure of the grating is imprinted onto the molecular beam through photo-induced beam depletion (see figure 2.4). The remaining molecules are then photoionized and extracted into a time-of-flight mass spectrometer (ToF-MS).[3]

The OTIMA possesses three absorptive light gratings. Three pulsed fluorine laser beams are directed onto a mirror to create three standing light waves. OTIMA works with the Talbot time (t_T), which is obtained if one divides l_T through the particle velocity v (see equation 2.3):

$$t_T = \frac{l_T}{v} = \frac{d^2 \cdot m}{h} \tag{2.3}$$

[3]Figure was taken from ref. [7]

The Talbot time no longer contains the velocity of the molecular cloud. However, there is still a constraint for the molecular velocity in OTIMA. As the mirror and the laser beams have a finite spatial extension, it has to be guaranteed that the molecules are over the mirror while they interact with all three light gratings. The full Talbot time $(2 \cdot t_T)$ can be approximated as 30 ns/Da for the current grating lasers installed (157 nm lasers). Let us consider two molecules with masses 11676 Da and 22152 Da respectively - the masses of the molecular libraries which are characterized in the scope of this work. Then we get $v_{max} = 114\ m/s$ for the lighter molecule and $v_{max} = 60\ m/s$ for the last one. Every standing light wave imprints a grating structure onto the molecular cloud. This is done through photoionization. Molecules flying through the antinodes of the standing light wave absorb one or more photons and get ionized or destroyed (photodepletion). These cations are then extracted through residual electric fields. This is shown in figure 2.4. The neutral fraction of molecules pass to the next grating. This process is schematically shown in figure 2.3. After the last grating, the neutrals are postionized and extracted into a mass spectrometer.

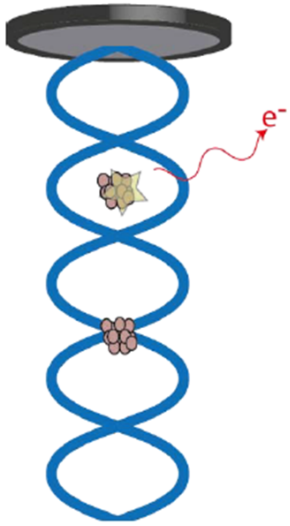

Figure 2.4: Working principle of an absorptive (photoionizing) standing light wave. [4]

[4]Figure was taken from ref. [32]

2.1.5 Source requirements

Molecular sources for matter-wave interferometry have to fulfill several requirements [33]. These are:

- *High beam intensity:* For a good signal-to-noise ratio of the interference pattern, the beam flux should be high and stable. In the case of KDTLI, $2 \cdot 10^{15}$ molecules per second would already lead to a high contrast interference pattern. In OTIMA, 10^6 particles would already be sufficient to observe an interferogram.

- *Low molecular velocity:* Since the de Broglie wavelength scales inversely proportional to the particle momentum, aiming at higher masses, means that a reduction of the forward velocity is needed for obtaining a large λ_{dB} which can be resolved in interference experiments. Current interferometer installations in Vienna (KDTLI and OTIMA) can cope with ≥ 200 fm [7]).

- *Low beam divergence:*

  - A molecular beam possesses a spatial expansion when it expands into vacuum. This is often referred to *molecular plume*. One important parameter is the plume opening angle. In the current experimental realization of both near field interferometers (KDTLI and OTIMA), the useful angle of the molecular plume is restricted to roughly 1 mrad [34].

  - If the transversal velocity of the plume is large, the molecules can travel from the nodes to the antinodes during the pulse length of the grating laser. A drastic visibility reduction would occur! For a pulse duration of $\tau = 10\ ns$ and a node-antinode separation of $39\ nm$, a maximal allowable transversal velocity of $4\ m/s$ results.

- *Small velocity spread:* Both the OTIMA and the KDTLI interferometer can cope with a velocity distribution of $\Delta v/v \approx 20\%$. A narrower selection increases signal to noise.

- *Neutral molecules:* Due to residual electric and magnetic fields, interference with heavy ion particles is a major challenge. Therefore, neutral molecules are cleary preferred.

- *Good photo depletion properties:* of the molecules guarantees a propper working of the laser gratings in the case of OTIMA. Electron impact ionization is very inefficient at low (few eV) and too harsh at high energies (e.g. 60 eV).

- *Vacuum compatibility:* High mass interference requires a good vacuum environment [35], e.g. $p \leq 10^{-8}$ mbar for 10^5 Da and $p \leq 10^{-9}$ mbar for 10^6 Da. The molecular sources should not introduce a high gas ballast.

2.2 Laser Desorption

In this work we utilize laser assisted volatilzation methods for bringing particles into the gas phase. In particular we use the matrix free laser desorption. Nowadays pulsed laser assisted desorption of molecules play an essential role in chemistry and biology. This is especially true for matrix assisted laser desorption (MALDI) [36]. MALDI is a widely used technique because it turns out that a variety of small biomolecules but also proteins can be ionized and volatilized without much fragmentation. In MALDI the analyte molecules are mixed mainly with ionizing matrix molecules. These matrix molecules posses a strong absorption band at the desorption laser wavelength, thus most of the deposited energy is used for the volatilization of the matrix molecules which then faciliates the evaporation of the analyte proteins. The process of ionizing is yet not fully understood but many models have been proposed and simulated [36]. Apart of MALDI, there is also LIAD (Laser induced acoustic desorption). Here the molecules of interest are put on a thin (typically 12 μm) metal foil (commonly titanium or tantalum) and onto the opposite side of the foil a high intense laser is focused ($300 - 600\ MW/cm^2$). The main advantage of this technique is that the molecules are not exposed directly to the laser beam which keeps the in-source-fragmentation level low. Additionally low forward velocities of the molecules are recorded [37]. In this work, however, we use the matrix free laser desorption with subsequent postionization (LD-PI) for the volatilization of high mass organic molecules. This is quite similar to MALDI. The different desorption techniques are shown in figure 2.5.

[5] Figure was taken from ref. [38]

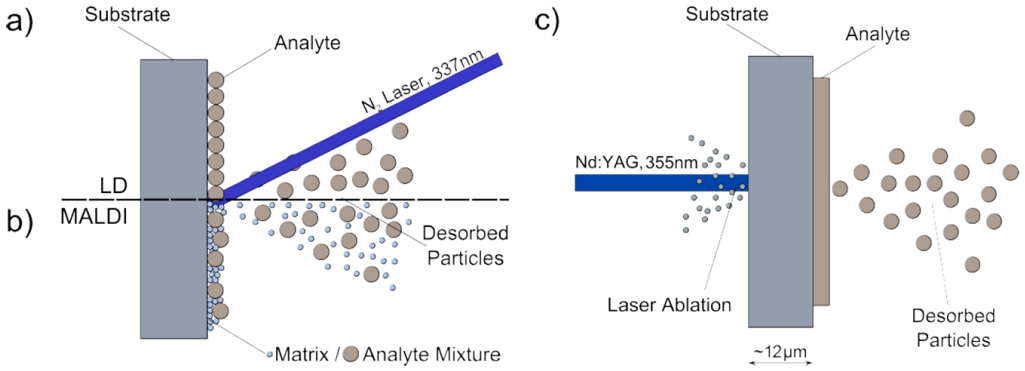

Figure 2.5: Laser driven desorption techniques. a) Laser desorption without any additional matrix molecules (LD-PI). b) Matrix assisted laser desorption (MALDI) and c) the laser induced acoustic desorption (LIAD).[5]

2.2.1 Mechanism of molecule ejection in MALDI and LD-PI

Many models have been proposed for explaining the ejection mechanism of molecules in MALDI. Thermal evaporation of individual molecules, layer-by-layer sublimation [39, 40], phase explosion [40] and volume ablation by laser-induced pressure pulses [39] are just some examples. However, a general theory describing all the observations is still lacking. Insight into the mechanism of ejection is mainly gained through experiments on the behaviour of the molecular ion yield (also included the post-ionized neutrals) upon variation of the desorption laser power [36, 41]. The rise of the signal intensity with growing laser fluence up to the value where molecular decomposition starts, has been fitted with a quasi-thermal model starting from an adapted Clausius-Clapeyron equation (equation 2.4) [41, 36].

$$N \propto \cdot f(A) \cdot exp\left(\frac{-E_a}{k_B \cdot (T_0 + \eta \cdot P\tau)}\right) \tag{2.4}$$

Whereas $f(A)$ is a function taking the desorption area into account (for Gaussian beams the spot size will vary with the laser intensity), E_a is the sublimation energy and $T = T_0 + \eta \cdot P \cdot \tau$ the temperature, whereas in the second term η stands for the conversion of the deposited energy into some degrees of freedom of the molecular lattice. Here T_0 is the initial temperature of the molecular sample and τ the pulse length of the laser and P the power density of the desorption laser. Based on molecular dynamics simulations of Zhigilei et al. equation 2.4 only holds below the laser ablation threshold [40, 42, 43]. One refers to the term *ablation* if the laser fluence exceeds a critical fluence at which also material from the target surface can be lifted up into the gas phase.

Below this threshold the term *desorption* is used. For fluences exceeding the threshold after which ablation starts, the observation could be described with a model, which describes the explosive change from solid to gas phase. This is described by equation 2.5.

$$Y \propto \cdot\delta \cdot ln^n \left(\frac{H}{\delta \cdot (E_V^* - c \cdot T_0)} \right) \tag{2.5}$$

Here Y describes the molecular ion yield and δ is the laser penetration depth, n is 1 for flat top and 2 for Gaussian laser beam profiles, H the fluence, E_V^* is a critical energy density and c is the specific heat capacity of the material. Equation 2.5 describes a model in which the laser pulse ablates material up to a certain depth, at which the deposited energy per volume is of the same order of magnitude as the cohesive energy of the solid [36].

Number of ejected molecules and monolayers

At present there is no experimental method to determine the number of desorbed molecules precisely and only estimates can be made. According to the Lambert-Beer law [17], the penetration depth of an electromagnetic wave is inversely proportional to its extinction coefficient in the material [44], $\delta = 1/\alpha$. Molar extinction coefficients can be determined through UV-Vis spectrometry in the liquid phase and it was shown that the absorption bands are only slightly shifted and broadened in the solid state [45]. For many matrix molecules in MALDI the range is from $\epsilon = 5 \cdot 10^5 - 5 \cdot 10^6\ L/(mol \cdot m)$ which corresponds to an absorption cross section of $2 \cdot 10^{-17} - 2 \cdot 10^{-16}\ cm^2$ [45]. According to ref. [46] the thickness of a dihydroxybenzoic acid (DHB) monolayer is approximately 5 $\mathring{A}$. Thus 40 - 400 monolayers can be desorbed, which is consisted with the values reported in ref. [36]. However, in our case the low post-ionization efficiency has to be taken into consideration. This is in the order of several percents. Also the volatility, crystallization rate and absorptivity of the laser light will certainly vary with molecules.

2.2.2 Laser parameters

Laser wavelength

In matrix assisted laser desoption ionization (MALDI) the choice of the laser wavelength is mainly determined through the absorption bands of the matrix molecules.

For the common MALDI matrices there is a strong absorption at the laser line 337 nm which lead to efficient and fragmentation poor volatilization of the analyte molecules [36]. There are also experiments, in which mid-infrared lasers are used [47–49]. Here the molecules of interest are dissolved in water, then dropped on a target plate and then the plate is cooled so that the droplet is transformed into ice. In some experiments also glycerol is used as solvent. The main idea behind this is the fact that intramolecular vibrations in water or glycerol can be excited upon absorption of mid-infrared photons ($\approx 3\ \mu m$). One of the main advantages of the mid-infrared technique is the natural environment (water) in which biologically relevant molecules (e.g. proteins) are embedded so that their 3D structure is preserved [47].

Laser pulse duration

In the case of MALDI or matrix free laser desorption, the analyte molecules are directly exposed to the laser beam. Taking 100 μJ (standard desorption energy in our lab), an average power of 27000 W is obtained for a pulse duration of 3 ns. At these laser energies, still intact molecules are observed. In pulsed laser desorption experiments many effects contribute to the soft volatilization. First, the laser pulse length plays an important role, as it determines the heating rate. In typical experiments the pulse duration lies between 0.5 to 10 nanoseconds [36]. Longer pulses are considered to enhance molecule dissociation [50]. One distinguishes between two different fragmentation processes, the fast dissociation channel (in source decay =ISD) and the post-source decay (PSD) [36]. The time needed from excitation to the decay in ISD is comparable to the phase-transition time ($\approx$ 300 ns) [51], whereas in PSD it can even exceed the flight time of the analyte particles to the detection stage [52]. The time constants depend on the physiochemical properties of the analyte and matrix molecules and on the pulse duration of the desorption laser. The pulse duration will also affect the internal energy of the desorbed molecules. An experimental study of Vertes et al. [53] showed significantly less fragmentation of analyte ions if a picosecond laser was used instead of nanosecond pulses. In ref. [54] they propose that molecular ionization in MALDI with picosecond laser pulses is due to a ladder climbing process, in which the high pumping rates exceed the fragmentation rates and lead to a large number of excitons. For nanosecond pulses a ladder-switching mechanism is proposed. Here the dissociation channels compete with the optical pumping and fragmentation may occur before the ionization potential is reached.

Using shorter pulse durations for soft volatilization has gained attraction in the last few years. Many experiments with fs-MALDI have been conducted [55] for that reason. For the sake of completeness, it should be noted here that the molecular plume plays also an essential role in lowering the fragmentation rate of the analyte molecules. This can be explained by the intermolecular collisions within the desorption plume. Bae et al. [56] showed that the temperature of the molecular plume is decreased by $300 - 400$ K at a time scale of several hundreds of nanoseconds. Collisions can also sharpen the molecular plume [57], i.e. reduce the translational temperature. A collision fequency of $10^4\ s^{-1}$ in the early plume is given by Puretzky et al. [58] for matrix assisted desorption of a 30 kDa protein embedded in 3-hydroxypicolinic acid.

Angle of irradiation

Some studies show a dependence of the ion intensity on the laser beam angle [59]. It was found that the ejected plume is directed into the direction of the incoming laser beam. The shape and symmetry of the laser induced craters depends on the illumination angle [60]. This has for example been shown for solgel and polymer materials in ref. [61]. An ejection of the molecular plume perpendicular to the desorption plate is a key for optimizing the signal abundances and peak resolution in matrix assisted laser desorption. Therefore some commercial MALDI-TOF instruments have axial feed-through of the desorption laser beam.

2.3 Detection

In the previous section I discussed the mechanism of molecular ejection and the influence of laser parameters of MALDI and LD-PI. However, there was no word told about the molecule detection. This is why I decided to dedicate this section to present detection mechanisms on single molecules and in particular to the working principle of a time of flight spectrometer. Detection of single molecules has always been an intriguing field of research. All began with the invention of optical microscopy, however its resolution is limited by $d = \lambda/(2 \cdot NA)$ (NA is the numerical aperture). With the invention of the electron microscopy, single particle detection became feasible at a high resolution scale. A scanning transmission microscopy (STM) was implemented in the Vienna QNP for the read-out of the interference pattern of C_{60} molecules [62], but the scanning process is extremely time consuming.

Other optical detection methods based on the fluorescence of single molecules have also been investigated in the same research group [63]. This technique is quite useful and can also be implemented in a near field interferometer [64]. Unfortunately fluorescence detection of single molecules is yet limited to molecules with a high quantum yield making this technique not universal. Experiments on the neutral detection of particles based on superconducting nanowires [65] have also been conducted. Current research on the detection of uncharged molecules gained a lot of attention over the last few years and led to many important inventions mainly based on micro resonators [66–71]. The molecule detection is done here with a time of flight mass spectrometer (ToF-MS). The working principle of a time of flight detector is as follows: A particle travelling across an electric potential U will gain a kinetic energy proportional to the depth of this potential (see equation 2.6).

$$E_{kin} = \frac{1}{2} \cdot m \cdot v^2 = e \cdot z \cdot U \tag{2.6}$$

Here m denotes the mass, v the velocity and $e \cdot z$ the charge of the particle. After transversing a field-free drift tube of length s, we can measure the flight time t for a particle of velocity v.

$$t = \frac{s}{\sqrt{2 \cdot e \cdot U}} \cdot \sqrt{\frac{m}{z}} \tag{2.7}$$

Particles with different m/z ratios will have different arrival times [72]. The basic composition of a typical linear time of flight spectrometer is shown in figure 3.3. It contains: a repeller, a focussing ion lens, two acceleration stages and a particle detector, which is a micro channel plate (MCP) in our case. For measuring the travelling time of the ions, a starting time point has to be set. This is done with a pulsed extraction of the molecular cloud. A high voltage of 2 kV is applied to parallel plates (repeller). One could use the laser pulse of the desorption to start the flight time measurement, however this has many disadvantages. The laser desorption process releases particles from different positions of the droplet and all the volatilized molecules have different kinetic energies. This leads to distinct flight times even for particles with the same m/z and this broadens the mass peak. A pulsed extraction, however overcomes this problem by focussing the molecular cloud in time [72, 73]. At the second stage an ion lens is installed. This focusses the molecular cloud onto the detector. This is in particular important for achieving high signal intensities. Many linear ToF instruments have two acceleration stages.

As we will discuss in the upcoming paragraph, the detection efficiency of a microchannel plate (MCP) increases with increasing velocity of the ions. The higher the acceleration voltage, the more efficient is the detection. However, due to technical limitations (breakdown of the electrical insulation) a maximum voltage of 20 kV is used. High ion velocities also overcome the differences in the initial kinetic energy [72, 73]. After focussing and acceleration, the molecules hit the particle detector, which is a MCP. The detection efficiency depends on the ion velocity [74]. Figure 2.6 shows the measured and calculated detection efficiency for polystyrene molecules which are variable in size and thus in mass. It can be easily seen that higher velocities increase the detection efficiency. For further reading see ref. [74].

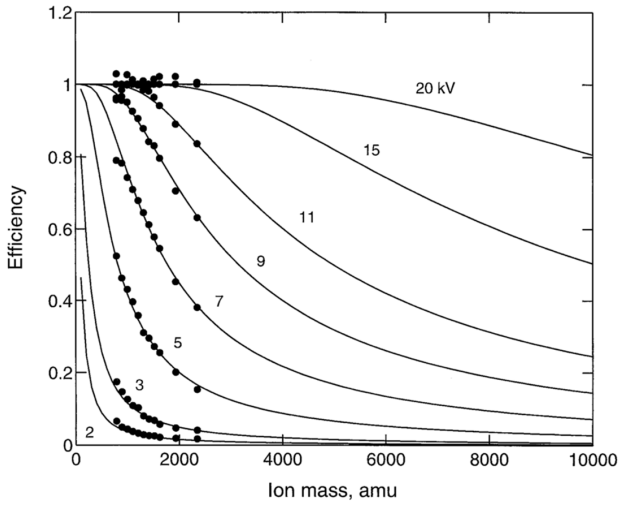

Figure 2.6: The calculated and experimentally determined secondary ion yield (detection efficiency) for different masses and different post-acceleration voltages.[6]

2.3.1 Extracting the velocity of a molecular cloud

For matter-wave interferometry, the momentum of a particle plays an essential role, as it determines the de Broglie wavelength. The velocity distribution of the molecular cloud is here recorded by varying the time delay between the desorption laser and the post-ionization laser. The real arrival time t of the particles at the detector contains the time for the desorption process t_d, the field free drift time t_0 and the time for acceleration of the ions t_a leading to $t = t_0 + t_d + t_a$ [72]. There are many theoretical models for fitting the time of flight distribution, most of them accounting for the jet-like emission of the molecular plume [36].

[6] Figure was taken from ref. [74]

Here we use the conventional Maxwell-Boltzmann distribution (equation 2.8).

$$f(v)dv = \sqrt{\left(\frac{2}{\pi} \cdot \left(\frac{m}{k_B \cdot T}\right)^3\right)} \cdot v^2 \cdot exp\left(\frac{-(m \cdot v^2)}{2k_B \cdot T}\right) dv \tag{2.8}$$

where m is the mass and v the velocity of the molecules, T the temperature of the molecular cloud and k_B the Boltzmann constant. In order to get a time distribution we have to substitute v by the distance s and the time t: $v = s/t$ and $dv = -s/t^2\ dt$. Nevertheless, then the equation is still not complete as it doesn′t take into account the type of detector we′re using. Post-ionization is done with a F_2 laser, which is sensitive to the particle density. Therefore an additional factor of $1/t$ has to enter [75]. A density sensitive detector assures that all particles inside the ionization region are detected before new molecules can enter or leave it [38]. The distribution then reads:

$$g(t)dt = \sqrt{\left(\frac{2}{\pi} \cdot \left(\frac{m}{k_B \cdot T}\right)^3\right)} \cdot \frac{s^2}{t^3} \cdot exp\left(\frac{-(m \cdot s^2)}{2k_B \cdot T \cdot t^2}\right) dt \tag{2.9}$$

Chapter 3

The Experiment

> *A theory is something nobody believes, except the person who made it. An experiment is something everybody believes, except the person who made it.*

A. Einstein, *1879-1955*

For testing various molecular sources, a new experiment was designed and built up. A major feature is the implementation of three molecular laser desorption sources, like MALDI (matrix assisted laser desorption ionization), LDI (laser desorption ionization) and LIAD (laser induced acoustic desorption) (see figure 2.5). It enables us to test particular methods suitable for some specific molecules. An example for that are peptides or proteins. As it is known that biomolecules are thermally fragile, it makes no sense to volatilize them under harsh conditions, e.g. evaporation through continuous laser heating. For such molecules it is better to use desorption techniques, in which the analyte is not directly exposed to the laser beam. This is the case in LIAD. Some desorption methods may already satisfy some of the requirements to molecular sources mentioned in section 2.1.5. Apart of that a combination of many volatilization techniques enables the comparison of results under otherwise similar experimental conditions such as detector conditions, sample preparation etc. For many desorption methods many information on the influence of laser desorption parameters on the molecular intensity is still lacking.

Especially LIAD has gained attention over the last few years and an increasing number of studies have been carried out [37, 76, 77].

3.1 An overview of the set-up

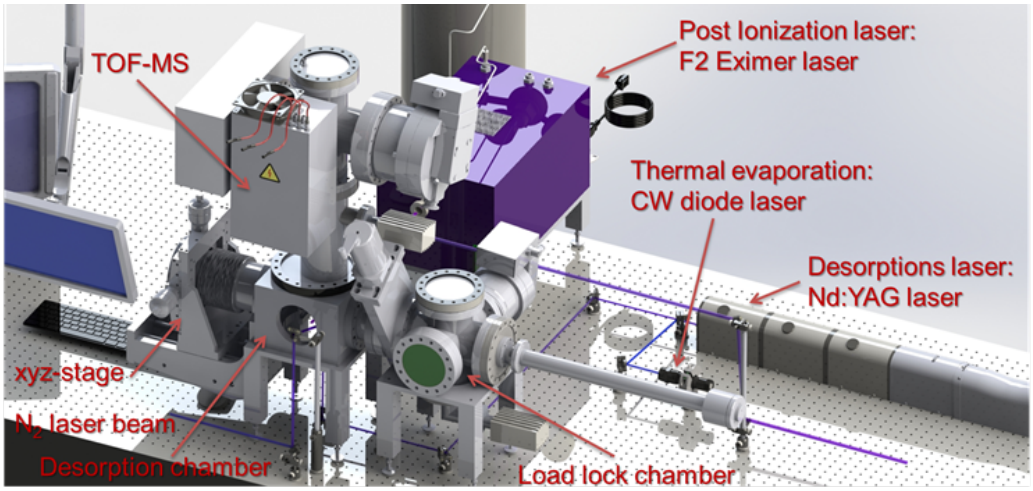

Figure 3.1: A 3D drawing of the actual experiment. Molecular laser desorption takes place in the main chamber. This is a stainless steel cube with many ports for laser access. For a close up of the desorption region see figure 3.3. Left to the cube a xyz stage is mounted for the manipulation of the sample plate. To the right a linear manipulator together with a cross vacuum chamber which serves as a load lock chamber is separated through a manual valve. A linear time of flight detector is attached directly above the cube.[7]

Figure 3.1 is a detailed drawing of the multifunctional experiment. The desorption process takes place in a cubic vacuum chamber. This has an optical access at each side and is therefore ideal for our purpose. A closer look into this cube shows that the molecular sample target is positioned on a sample holder (see figure 3.2), which can be computer-controlled with a motorized xyz stage. The sample holder is compatible with MALDI or LDI, but also LIAD foils can be clamped (see figure 3.2). It consists of a sample support frame on which a U shaped steel can be mounted. The U shaped stainless steel plate is wider than the supporting frame so that it can be lifted up by a fork like linear manipulator. Through this mechanism the sample can be exchanged very easily and very fast. The magnetically coupled manipulator with linear and rotary motion is attached to a 6-way chamber, which is separated from the main desorption chamber by a manual valve. A turbo molecular pump (modell TMU 521 from Pfeiffer Vacuum) and a vacuum gauge are installed.

[7] Some elements of this 3D drawings were taken from grabcad.com

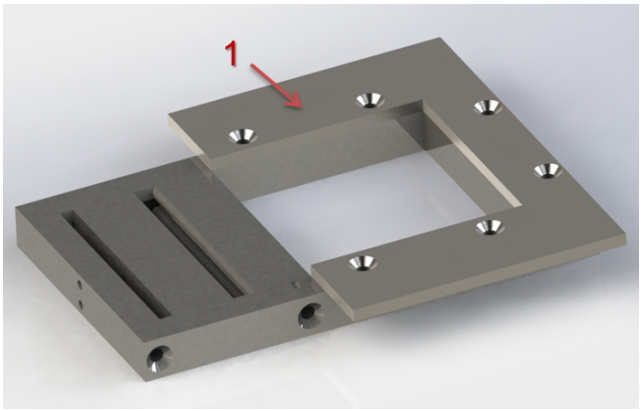

Figure 3.2: Solid Works drawing of the sample holder. The foil or sample target is put between the U shaped steel plate (1) and the frame. This holder can then be placed on a linear manipulator.

After several minutes the load lock chamber is ready for venting and the target plate can be exchanged. At 10^{-6} mbar the valve can be opened again and the freshly prepared sample plate is placed onto the holder.

3.1.1 Molecule detection on a linear time of flight mass spectrometer

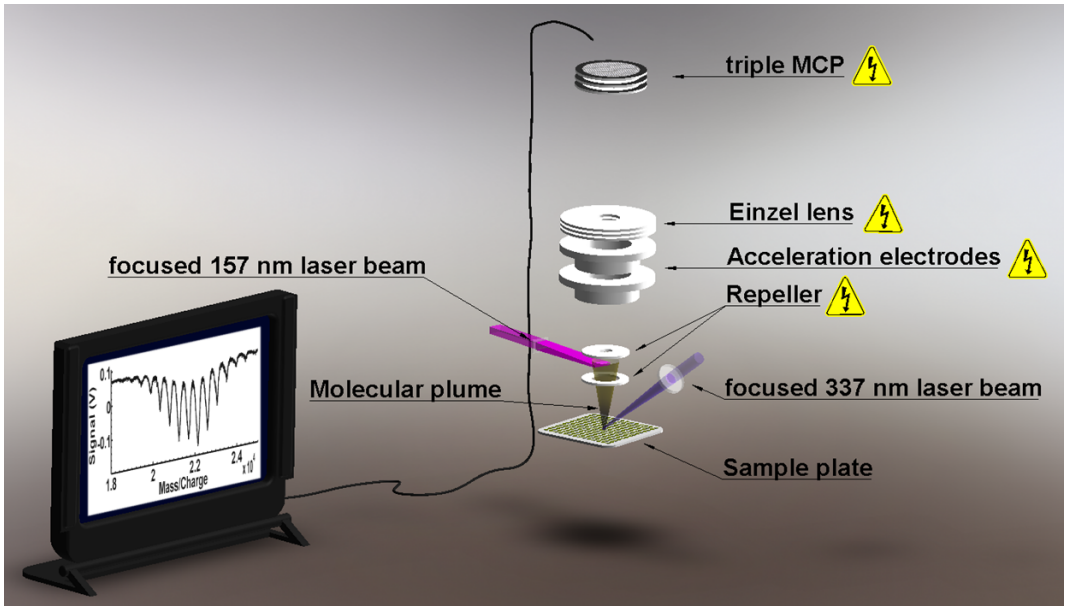

Figure 3.3: A close-up of the desorption region. The nitrogen laser beam is focused onto the target plate. This leads to the formation of a molecular plume. A fluorine post-ionization laser intersects this plume and the photoionized molecules are extracted into the time of flight detector. A stack of three micro channel plates detect the molecules.

The working principle of a time of flight detector has been described in section 2.3. The post-ionized molecules are collected and detected by a customized linear time of flight mass detector with a resolution of $m/\Delta m = 100$. This has been manufactured by Kaesdorf GmbH (Munich). It consists of three parts: the repeller (ion extraction region), ion optics and an ion counting module. In figure 3.3 all these parts are shown. A stack of three micro channel plates is used to increase the detection efficiency for heavier molecules. Liner 2 and liner 1 form the acceleration stage of the ToF. As the detection efficiency increases with growing velocity of the particles, liner 2 is supplied with the maximum voltage of 16.2 kV. In order to optimize the signal intensity via optimal focussing onto the MCP, the voltage on liner 1 and the ion lens were varied and an optimal value was found. Finally, the distance between the two repeller plates (see figure 3.4) was reduced so that the electric field strength increased. This is in particular important to exert a bigger force on the charged molecules to be sucked into the ToF and the short distance also guarantees a more homogenous electric field. The new repeller design is shown in figure 3.4 with a new separation distance of 6.5 mm.

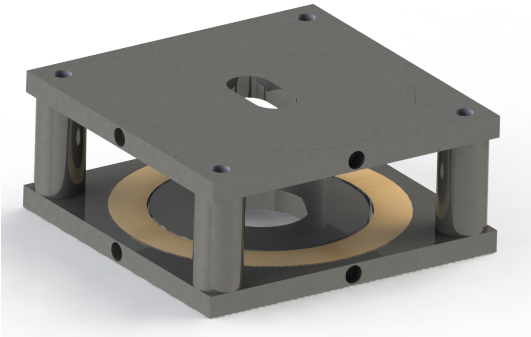

Figure 3.4: The new design of the repeller. The distance between the two plates is roughly 7mm. Voltage is put on the inner circle, which is isolated from the supporting frame through PEEK (beige material).

Mass calibration of the linear ToF

A correct calibration is important for the exact mass determination. For that reason one uses molecules of well known masses. Here all calibration measurements were done simultaneously with: ZnTPP and $\mathrm{TPPF}_{20\mathrm{x}+17\mathrm{x}}$ (ref. [78]) and the square root of the nominal mass/charge is plotted against the arrival times of the particles (see section 2.3).

This is then linearly fitted and the slope and the intersection of the linear function with the y-axis serve as the conversion factor from the flight time to mass. Figure 3.5 shows an example of such a calibration curve.

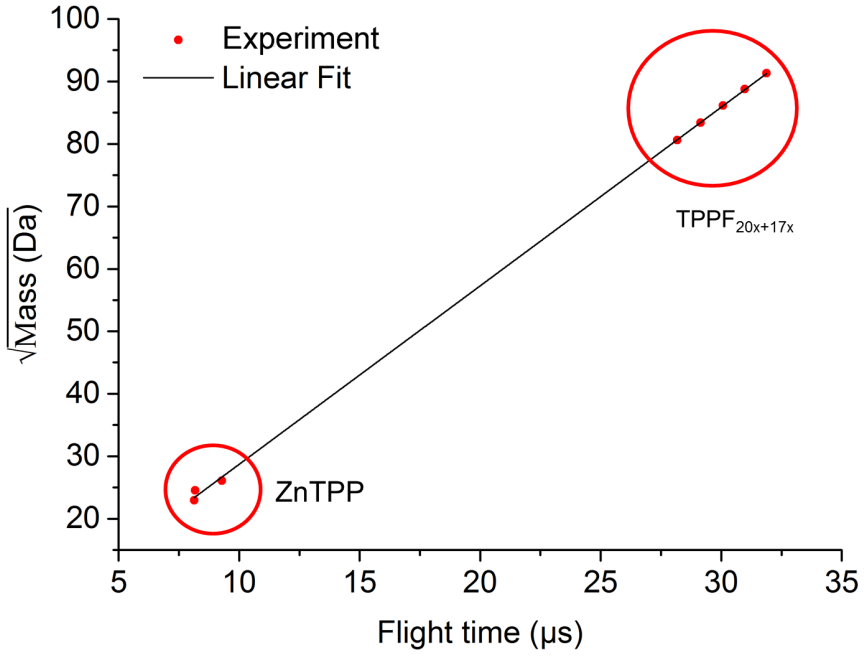

Figure 3.5: Calibration of the time of flight mass spectrometer. There is a linear dependence between the square root of the nominal mass in Da and the flight time. Larger arrival times correspond to higher m/z values.

3.2 The laser system

Important parts of desorption experiments are the various lasers. It is known from the literature that the wavelength, pulse length, beam profile as well as spot size have significant effects on the desorption and ionization efficiency [41, 79, 80]. A short description of the laser systems used for laser desorption and post-ionization shall be given in the following section.

3.2.1 The nitrogen laser

In my desorption experiment the laser beam of a N_2 laser is focused onto the sample plate. The beam shape at the output of the laser is rectangular and has a size of roughly 7 x 5 mm. After focussing by a plano convex lens with a focal length of f = +50 mm it then has a dimension of 1.5 x 0.5 mm. This is shown in figure 3.1 and figure 3.3 . The incident angle of the beam is chosen to be approximately $30°$, as an increase was not possible due to technical limitations (e.g. window size). Nitrogen lasers are commonly used for MALDI as the wavelength of 337 nm is absorbed by many matrix molecules. As we don′t use any matrix molecules, any wavelength for intact desorption of the molecules would come into consideration. However, as an ion trap is established in our lab, we utilize MALDI for the loading of the quadrupole trap. Here a N_2 laser with an output wavelength of 337 nm is therefore advantageous. The nitrogen laser beam is guided through several one inch 337 nm high reflectivity coated fused silica mirrors to an aperture. The output of the N_2 laser is rectangular, but after the aperture the beam is transformed to a circularly shaped profile.

How does a N_2 work?

There are many types of lasers classified according to the optically active medium used for lasing. Solid-state laser, dye lasers, semiconductor lasers and gas lasers are just some of them. However, here we want to emphasize the discussion of the nitrogen laser, which belongs to the molecular gas lasers. The N_2 laser is a typical three level vibronic laser. Here an electrical discharge of the gas in the laser tube initiates a flux of high energetic electrons. They collide with nitrogen molecules and excite them without significant dissociation [81]. Once excited, the molecule then falls to the $B^3\ \Pi_g$ state under emission of a photon with $\lambda = 337.1\ nm$ and a typical life time of $\tau \approx 40\ ns$. However the pulse duration can be controlled upon variation of the nitrogen pressure inside the nitrogen gas tube [81]. The transition between the highest level to $B^3\ \Pi_g$ represents the lasing transition, which only takes place between the various rotational levels of the lowest vibrational energy level $(\nu''(0) \rightarrow \nu'(0))$. There exist other possible emission paths, however with lower Franck-Condon factors. From the 61 possible laser lines of the lowest vibrational level, also transitions like $\nu''(1) \rightarrow \nu'(0)$ ($\lambda = 357.7\ nm$) or $\nu''(0) \rightarrow \nu'(1)$ ($\lambda = 315.9\ nm$) can occur. After lasing, the N_2 molecule falls into a metastable energy level and then back to the ground state [82, 81].

The whole laser process is schematically shown in figure 3.6.

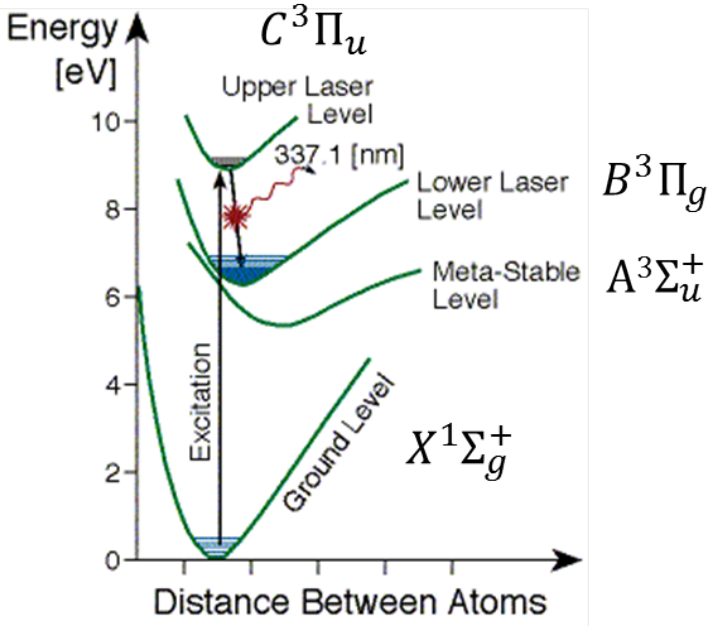

Figure 3.6: Energy level scheme for a nitrogen molecule. Energetic electrons excite the molecule, which then falls to the lower laser level through emission of a $337.1\ nm$ photon. Through collisions with the back ground gas the molecules are then transferred to the ground state.[8]

The model we used in our experiment is called VSL-337ND-S from Thermo Science. It is specified with a pulse length of $\tau \approx 3\ ns$, a pulse energy of maximally $120\ \mu J$, a maximum repitition rate of $60\ Hz$ and a full angle beam divergence of $0.3\ mrad$.

3.2.2 The fluorine laser

Excimer lasers emit in deep UV. As the name suggests, an excimer laser uses the transition of an excited dimer to its dissociating ground state. The dimer only exists in the excited state. However, here a slightly different system should be discussed briefly. The fluorine laser, emitting at 157 nm is used in micromachining for processing sub 100 nm structures [83]. In lithography, 157 nm light sources revolutionized the tool and wafer production and are still an active area of research [84]. F_2 lasers are also essential in OTIMA interferometry [7].

[8]Source: Wright, Leslie: Nitrogen Laser. URL: `http://www.fineartradiography.com/hobbies/lasers/nitrogen/` (18.05.2014)

Here they form standing light gratings and imprint this structure onto the molecular beam through photodepletion. A fluorine laser GAM Inc. (Orlando) is also used for post-ionization of neutral molecules in our set up, as shown in figure 3.3. Fluorine lasers are commonly operated with a mixture of fluorine and helium gases. The ratio of these two determines the laser parameters such as the output energy, pulse length and laser wavelength. As in N_2 lasers, fluorine lasers begin with a high voltage gas discharge. In contrast to excimer lasers, the F_2 lasers posses a ground state. Three processes can lift the fluorine molecule into the excited state $F_2(D')$ [85–87]:

1. Collisions with electrons or with noble gas atoms can lead to $F_2(D')$ according to:

$$F_2 + e^- \rightarrow F_2^* + e^-$$

$$F_2 + He^* \rightarrow F_2^* + He$$

$$F_2 + He_2^* \rightarrow F_2^* + He_2$$

2. Neutral collisions can result in $F_2(D')$:

$$F_2 + F^* \rightarrow F_2^* + F$$

3. Excitation by a three body collision:

$$F^+ + F^- + He \rightarrow F_2^* + He$$

From the $F_2(D')$ to the electronic state $F_2(A')$ the lasing at 157.6 nm occurs. The lifetime of the excited state is of the order of several nanoseconds. The excitation process is in competition with relaxation phenomena like collisions or spontaneous emissions. This is the reason why excimer coherent light sources are pulsed lasers. A detailed summary of all collisions and emission path ways is given in figure 3.7. However, a fluorine laser also emits red light. This is useful for laser alignment, since VUV photons are absorbed by oxygen in the ambient air [9][87]. Emission in the red is due to the fact that fluorine molecules can populate different excited states of F^*, which however will decay to the lowest level of F^*. These transitions are accompanied with a 600-800 nm radiation [87].

[9]VUV rays are absorbed through oxygen with an absorption cross section of 200 $1/(cm \cdot atm)$

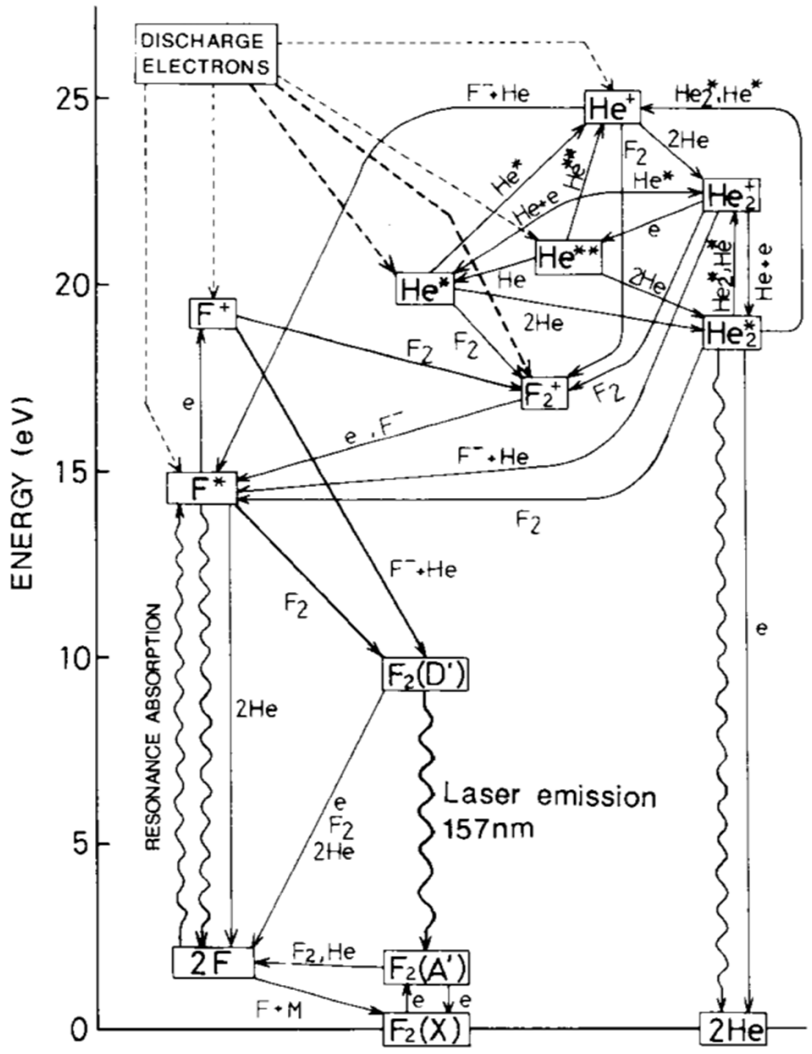

Figure 3.7: : Excitation paths in a fluorine/helium laser. The ground state F_2 molecules can be excited to $F_2(D')$ through various ways. Three of these possibilities are listed in the text. Relaxation from the $F_2(D')$ to $F_2(A')$ leads to the known laser transmission of 157.6 nm [85–87].[10]

Our fluorine laser has a 10 ns pulse duration and a maximal output energy of 1.4 mJ at a gas pressure of 3.4 bar. It has a maximum repitition rate of 250 Hz. The laser beam must be enclosed in a tube, which is continuously purged with dry nitrogen in order to keep the O_2/N_2 ratio at 10^{-6}. We use a cylindrical lens with $f = +200$ mm to focus the light into the repeller volume. The focused beam shape has the dimension of 1 x 8 mm (figure 3.3). For measurements of the molecular ionization cross section, the power of the laser has to be varied. This can be done by changing the discharge voltage of the laser. As it is shown in figure 3.8, the energy per pulse scales linearly with the discharge voltage.

[10]Graph was taken from ref. [86]

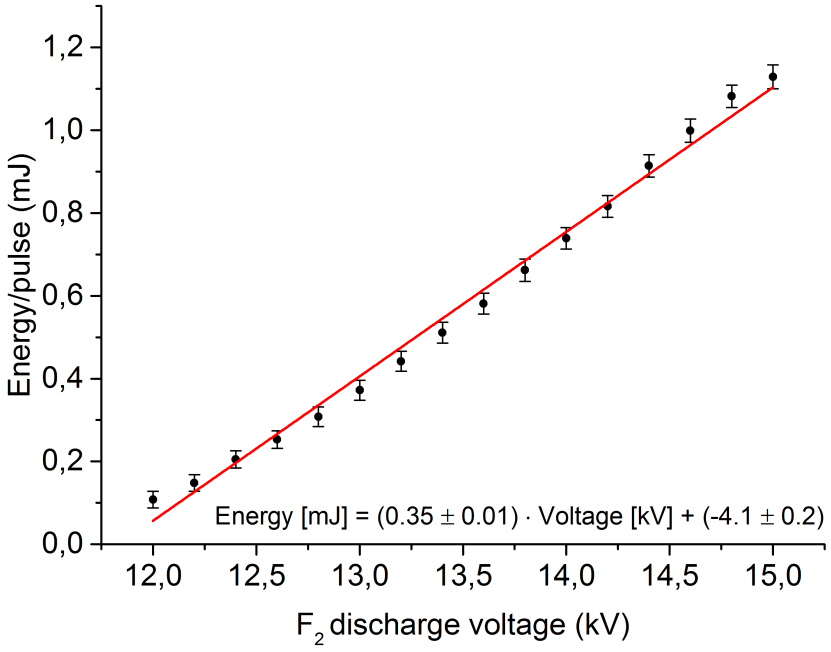

Figure 3.8: Laser pulse energy as a function of the gas discharge voltage in the fluorine laser.

3.2.3 The Neodymium:Yttrium Aluminium Garnet laser

A Nd:YAG laser was used to test the thermal volatilization of perfluoroalkyl-functionalized molecules. This was done by guiding the third harmonics of the Nd:YAG laser (355 nm) beam through triple coated mirrors to a plano convex lens with $f = +50$ mm. After focussing onto the sample plate, the beam shape has a size of 1.2 x 0.3 mm. A Nd:YAG laser contains a crystal of $Y_3Al_5O_{12}$ (yttrium aluminium garnet) where some of the Y^{3+} ions are substituted by Nd^{3+} atoms [82]. As shown in the energy level scheme in figure 3.9, a Nd:YAG laser is a four level laser. The most essential laser transition happens between the level $4F_{3/2}$ and $4I_{11/2}$ with a radiation of 1064 nm. Apart of 1064 nm, other wavelengths such as 532 nm (2^{nd}), 355 nm (3^{th}), 266 nm (4^{th}) and 213 nm (5^{th}) (obtained through mixing of the fundamental and 4^{th} harmonics) can be generated. In our set up we use the Nd:YAG laser of Quantel (model: Brilliant 360 mJ). At 355 nm it has a maximum laser output energy of 60 mJ and a pulse length of $\tau \approx 4$ ns.

[11] Graph was taken from ref. [88]

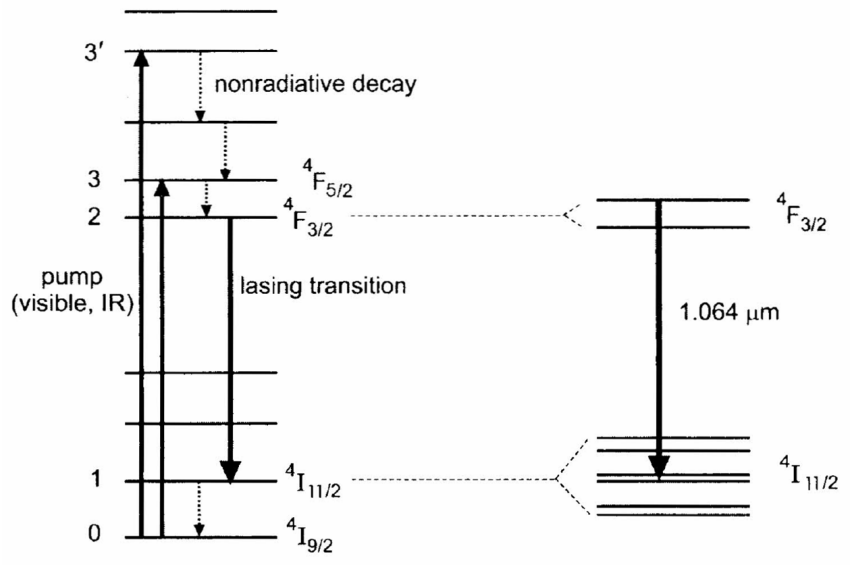

Figure 3.9: Schematic energy diagram of the lamp excited neodymium:yttrium aluminium garnet laser. The most important laser transition occurs from $4F_{3/2}$ to $4I_{11/2}$ with 1064 nm photon emission.[11]

3.3 Automation of the set up and the self written data analysis software

Data statistics is an important issue and fluctuations of the desorption yield are still a challenge. An automated molecular source helps to collect large data sets in short time and it would also simplify the data acquisition and allows to acquire conclusive data with good statistics. For that purpose an experiment with variable repetition rate was automated as follows: The LabView code initializes an oscilloscope (LeCroy Wavesurfer 454), the xyz stage and a pulse/delay generator (model 575 Berkley Nucleonics Corporation) and triggers the lasers with specific delays. A simplified model of the sequence is shown in figure 3.10. A data analysis program written in Matlab, is based on the mass spectrometry library of the bioinformatics tool of Matlab but it was modified according to our specific needs.

[12]This scheme was made out of several pictures which are listed below:

1. LabView logo URL: `http://de.wikipedia.org/wiki/Datei:Labview-logo.jpg` (21.05.2014)
2. Pulse generator URL: `http://www.pdsinstruments.co.uk/berkeley_nucleonics_main.htm` (21.05.2014)
3. N2 laser URL: `http://www.337nm.com/VSL-337ND_LaserInnovations.htm` (21.05.2014)
4. F2 laser URL: `http://www.photonicsolutions.co.uk/company.asp?CoID=GAML` (21.05.2014)

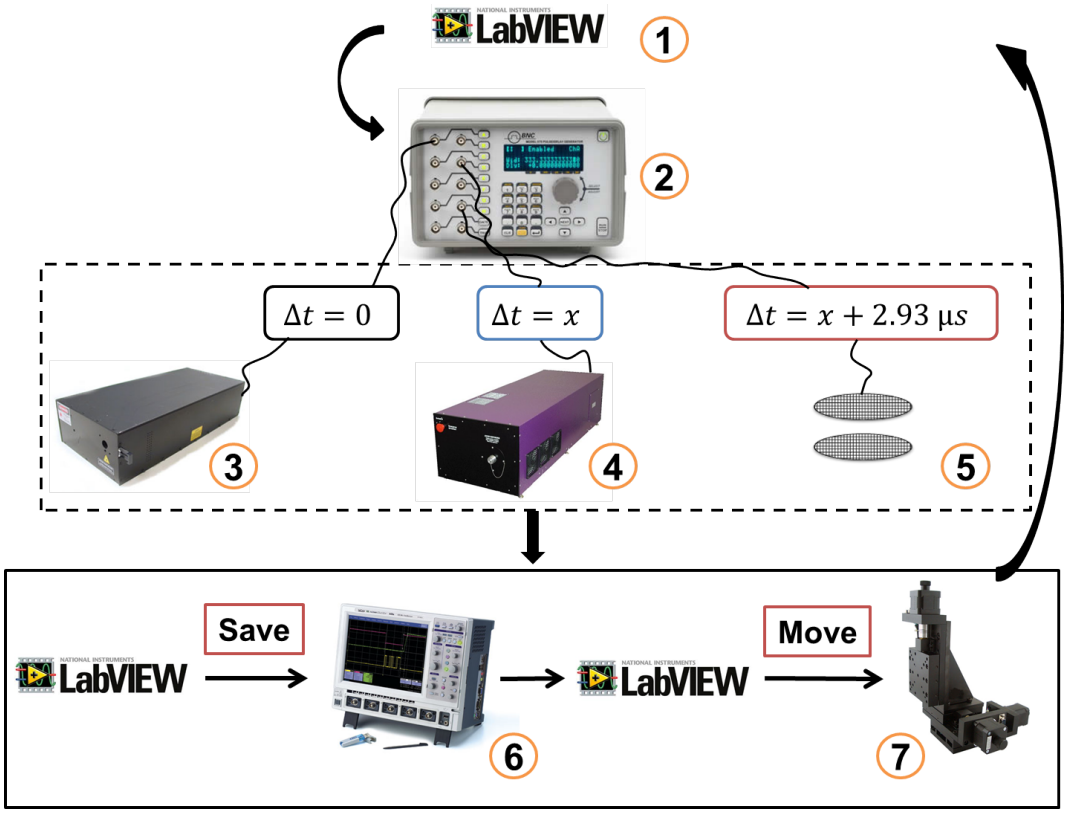

Figure 3.10: This simplified graphics shows the automation cycle for the whole set up. At first the LabView program (1) initializes the pulse/delay generator (2) and sets the values for trigger parameters (width of pulse, delay, etc). After that, the BNC generator triggers the instruments. The N_2 laser shoots without any delay after the delay generator has been started, whereas the F_2 laser (4) is triggered usually at a delay time x which the experimentator can determine. After $x + 2.93\ \mu s$ seconds the ToF electronics gets a TTL pulse for turning on the high voltage on the repeller (5). As soon as the signal is recorded and saved by the oscilloscope (6), the LabView program initiates the movement of the xyz-stage where the sample target is placed. After each shot the sample is moved to hit fresh molecules.[12]

3.4 Sample preparation methods

Great effort has been made for preparing homogenous samples in matrix assisted laser desorption ionization [45]. This problem is not trivial, as many uncontrollable or even uncharacterized effects are involved in the crystallization of the sample spot.

5. Self made
6. LeCroy oscilloscope URL: `http://www.testequipmentconnection.com/36808/Teledyne_LeCroy_WaveSurfer_454.php` (21.05.2014)
7. Motorized xyz-stage URL: `http://www.optics-focus.com/motorized-xyz-stage-p-862.html` (21.05.2014)

Not only surface properties like roughness or wettability play an important role, but also the interaction of the analyte and matrix molecules and even the way of coating the target plate with molecules (see figure 2.5) is essential. Since such effects depend on the analyte/matrix solution and target material, the sample preparation must be optimized individually. For that reason many mass spectrometry groups tried to develop new deposition methods [89–93].

Also here, the sample preparation is a crucial issue. However, here we are less interested in the improvement of the resolution of mass spectra but rather in the ability of launching and detecting molecules. A good shot-to-shot reproducibility allows statements about the molecular beam or the molecules themselves. Stable signals are also of great importance for matter-wave interferometry. They help avoiding unnecessary signal averaging. Our first observation was that deposited droplets immediately begin to spread on the metal target plate. After evaporation of the solvent, the material is mainly found at the rim of the droplet (see figure 3.11). The layers inside of the droplet seem to be homogenous, but additional fluorescence microscopy data show that more material is situated at the rim. In order to get rid of this effect, plasma treating of the metal target plate was done.

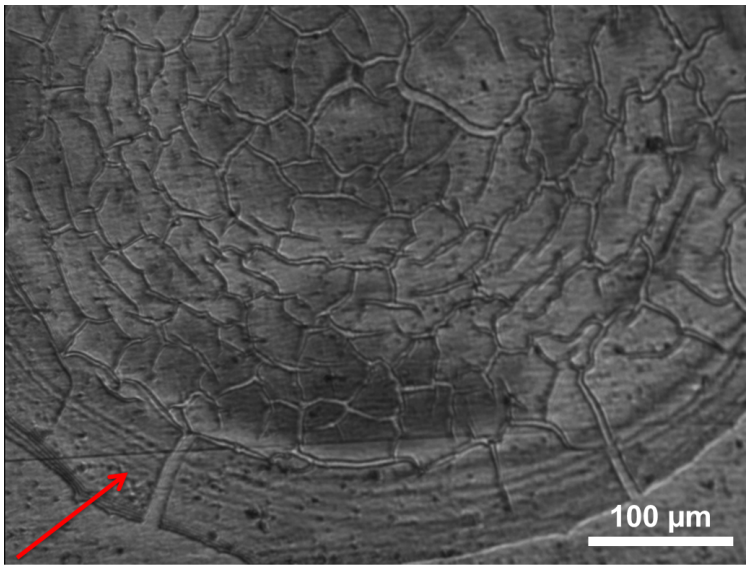

Figure 3.11: Drop on a stainless steel target. Most of the molecular material is situated at the rim (red arrow) of the drop. [13]

[13] Picture was taken on a Zeiss microscope with an Andor iXon camera at a magnification of 2.5x.

The idea was to increase the surface roughness, which should affect the adhesive forces between molecules and the surface [94]. Indeed it was shown that the plasma treatment can polish the surface to a roughness down to several nanometres, change the surface energy and help to get more homogenous coatings [14] (see figure 3.12a). Further decrease of the surface roughness was achieved with diamond nanoparticle polishing pastes (figure 3.12b).

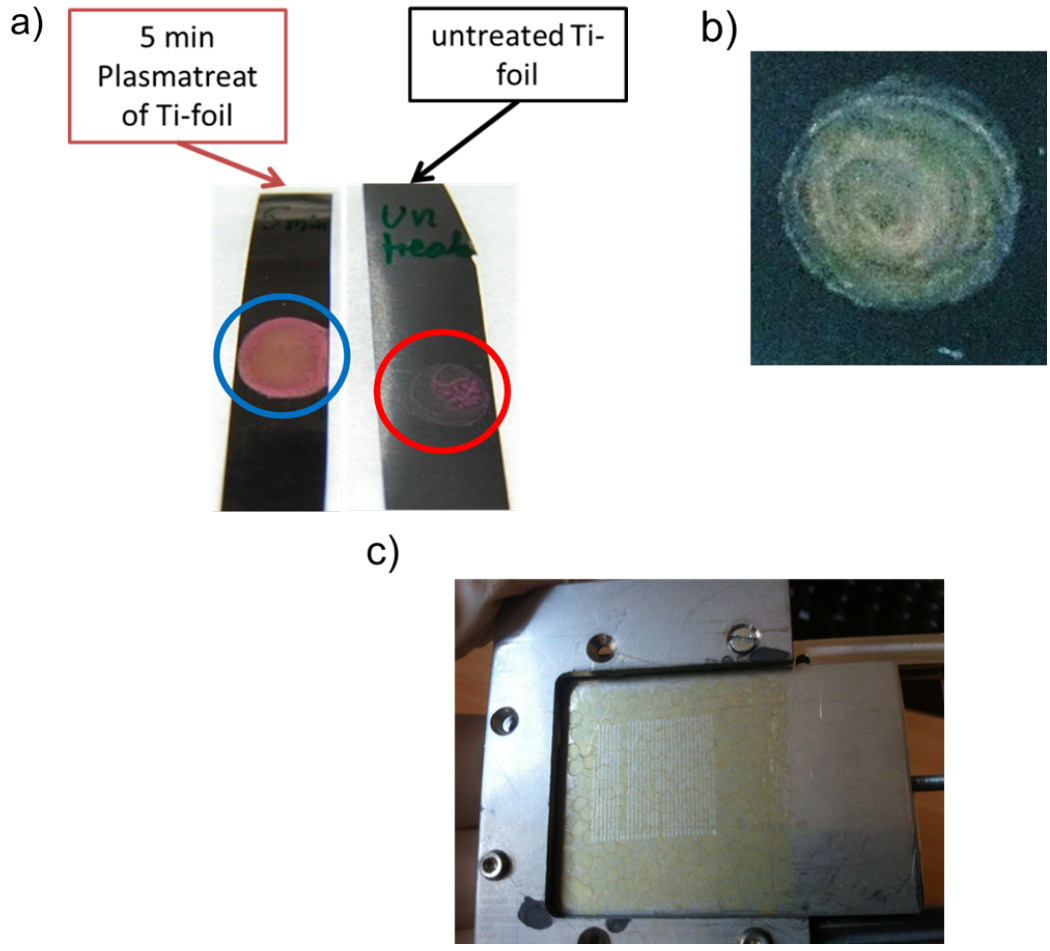

Figure 3.12: Various sample surface modification methods were tried. Plasma treating of a 10 μm titanium foil with ambient air leads to a better homogeneity of the molecular droplet (a). The same is achieved through treatment with diamond polishing (b). However, depositing small droplets (3-5 μm) and covering the whole plate gives similar results (c). As this technique is less time consuming, it was used for sample preparation. White stripes on green molecular coating arise from the successful laser desorption.

[14] See video at URL: `http://www.plasmatreat.com/plasma-treatment/plasma-pretreatment/plasma-activation_surface-activation.html`

Unfortunately such sample surface modifications are extremely time consuming and the improvement is rather small. The same shot to shot variations can be obtained by depositing 3-6 μL drops onto the stainless steel plate (see figure 3.12c). This technique was routinely used for sample preparation. As described in the upcoming section, we investigate two newly designed organic molecular libraries, designated here as library 1 and 2. The first we dissolved in diethylether. For library two, we took tert-butylmethylether (tBME). Before deposition, the stainless steel target was placed in an acetone bath and ultrasonicated for 10 minutes. Afterwards a 1-10μL pipette was used to deposit the droplets.

Chapter 4

Results and Discussions

> *Insanity is doing the same thing over and over again and expecting different results.*
>
> A. Einstein, *1879-1955*

Designing molecular sources for interferometry is not a trivial task (section 2.1.5). It has been shown [63] that new volatilization methods can indeed form molecular beams, which meet all requirements. This is true for far-field [63] and near-field matter-wave interferometers. Further development of molecular sources is still needed. Many research groups have specialized on techniques to produce intense beams of slow and cold molecules with a narrow velocity distribution. These approaches base on techniques like Stark decelarators, Alternating Gradient or Zeemann decelerators [95, 96] for rather small (up to several hundred Daltons) and charged molecules or with a sufficiently big electrical dipole moment. Optical slowing schemes [97, 98] have also gained attention. Recent ideas make use of the centrifugal slowing of polar molecules [99]. Also ion traps come more and more into consideration for the manipulation of the internal and external properties of molecules down to few Kelvins [100, 101]. This is essential for quantum interference experiments. However, ion traps can only deal with charged particles, hence for matter wave interferometers additional neutralization techniques are needed.

In order to do research on such fragile systems in the gas phase, special care has to be taken to avoid fragmentation during the volatilization process. One popular method is to cool the molecules by means of a buffer gas. Here the molecules are desorbed into the buffer gas and through the collisions their internal temperature is lowered. Under these conditions the molecules of interest are not only less prone to fragmentation but they also acquire low translational temperatures, which can reach down to 4.2 K [102]. However, for interference of large masses to occur, the background pressure has to be kept sufficiently low [35]. For objects ≤ 10000 Da a vacuum of $\leq 10^{-8}$ mbar is a prerequisite for matter-wave interference. Although this excludes the direct implementation of a buffer gas cell, pumping stages can circumvent this problem. One of the main disadvantages of using a pumping stage is the fact that the molecular beam path gets enlarged which then forces the molecular source to volatilize even more molecules. Optical cooling of nanoparticles has gained increasing attention during the last 20 years and many research groups (Markus Aspelmeyer, Lukas Novotny, Markus Arndt etc.) work on that [103, 104, 16]. Our group has shown recently that transverse cooling of nanoparticles with several hundreds of nanometres in diameter is possible [16]. The authors report that a reduction of the transverse kinetic energy by a factor of 30 has been realized. However, this technique is currently limited to nanoparticles in the range of $100 - 300\ nm$ ($\leq 10^{10} Da$). Preparing them for interferometry is still a challenge, as for example the temperature of the nanoparticle is very high ($\geq 10000K$). However for molecules up to the mass range of 10^5 Da known laser assisted volatilization methods can still be useful. Indeed, as I will show during the upcoming sections, laser desorption with appropriately chosen molecules already meets most of the requirements listed in section 2.1.5. Apart from the difficulty of volatilization of heavy molecules, many publications asked whether photoionization is mass limited [105, 106]. It was believed that this limit is about few thousand Daltons. However, in the past this limit could be pushed further [65, 107], recently even beyond 10000 Da [78]. With the molecules presented in the next section, we were able to identify a new class of particles. Flourination of porphyrin polymers to ≥ 25000 Da is the key to volatilization and photoionization in this mass range.

4.1 A new generation of the perfluoroalkylated molecular libraries

The molecules investigated here were synthesized by Lukas Felix in the group of Prof. Marcel Mayor at the chemistry department of the University of Basel. The synthesis is described in ref. [5]. Up to a certain mass (roughly 5-10 kDa) the strategy of monodisperse molecules works, however a further increase of the size is problematic since the purification is time consuming. For that reason we have focused on creating a molecular library. The strategy is based on a narrow mass distribution of perfluoroalkylated molecules. The central unit of the library is always the same (a porphyrin polymer), but the different number of attached fluorinated side chains determines the mass distribution [108, 109]. Since these molecules can be detected in VUV ionization, time of flight detection of the mass spread of the library is compatible with both the KDTLI [8] and the OTIMA[7]. We use fluorinated molecules for several reasons:

1. We are mainly interested in increasing the mass of the interference object. Incorporation of fluorinated alkyl chains into molecules is a promising way to do that. Addition of single fluorinated octyl chain increases the mass by 479 Da [108, 109].

2. Another important factor is thermal stability. The C-F bonds in a perfluorooctyl chain possess a higher dissociation energy (485 kJ/mol) compared to a hydrogen-carbon bond with ca. 425 kJ/mol [108, 109].

3. Fluorous compounds have a high volatility making them popular in environmental sciences [110, 111]. This is due to their low polarizability which results in small van der Waals interaction between different perfluoroalkyl chains. Thus less energy is required to lift them into the gas phase [108, 109, 98].

Our collaborators have designed two types of molecules.

4.1.1 $(\mathrm{ZnTPPF})_4\mathrm{F}_{60+16\mathrm{x}}$

$(\mathrm{ZnTPPF})_4\mathrm{F}_{60+16\mathrm{x}}$ contains four Zn-Tetraphenylporphyrins (ZnTPP) which are connected through a tetraphenylmethane unit.

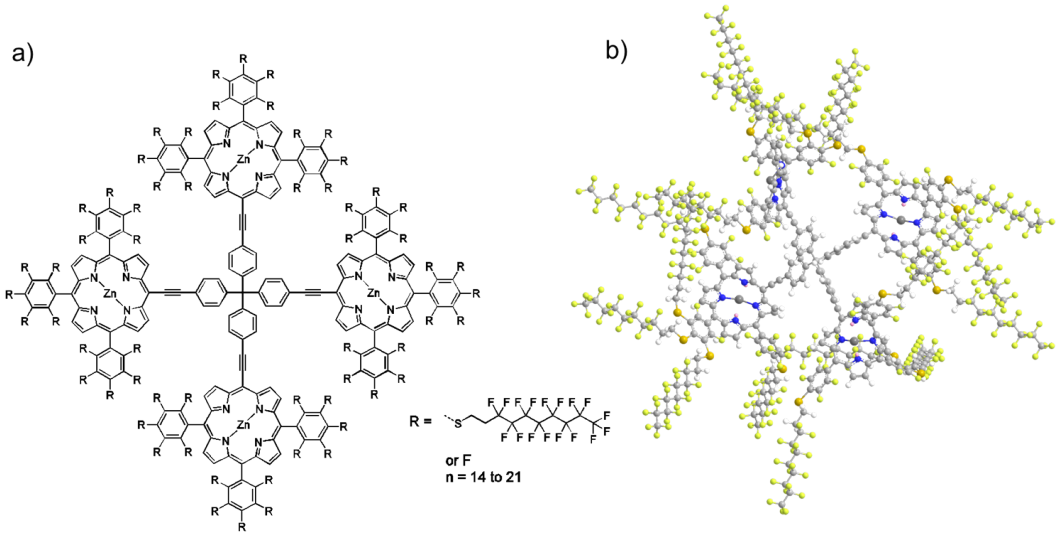

Figure 4.1: Molecular structure of $(\mathrm{ZnTPPF})_4\mathrm{F}_{60+16\mathrm{x}}$. Panel a) shows a schematic drawing of the molecule. It consist of a central tetraphenylmethane to which four Zinc tetraphenylporphyrins are attached. Each phenyl can be functionalized with up to five perfluoroalkylated chains. Due to steric shielding and electrostatic repulsion a full substitution is not possible. Panel b) shows a possible 3D structure but at an equilibrium temperature of 700 K [112], computed with the MM2 package of ChemBio3D Ultra. At this temperature the molecule undergoes conformational changes on the time scale of picoseconds.

Perfluorooctyl chains are attached to the phenyl groups of the ZnTPP. Furthermore, also matter-wave interferometers can contribute to a better characterization of porphyrins. This has been shown for their static and optical polarizabilities but also thermal features in the gas phase [63, 113–115].

The molecules have to be detectable, hence we require them to be photoionisable. It was shown in earlier works that porphyrins can be detected with either 193 nm or 266 nm [116–118]. The first ionization potential (IP) lies roughly at 6.5 eV [119, 120]. The low IP is in particular an important feature for the proper working of the current matter-wave interferometer in the time domain, as the efficiency of the laser gratings depends on a high photodepletion cross-section. The photoionization efficiencies of $(\mathrm{ZnTPPF})_4\mathrm{F}_{60+16\mathrm{x}}$ (see figure 4.1) and $\mathrm{TPP}(\mathrm{TPP})_4\mathrm{F}_{60+16\mathrm{x}}$ (figure 4.2) will be discussed in section 4.2. Tagging of chromophores to a specific molecule facilitates the (single) photoionization - a strategy which has been pursued by many other research groups [121, 122]. Third, it is also known from literature [123] that tetraphenylporphyrins are thermostable.

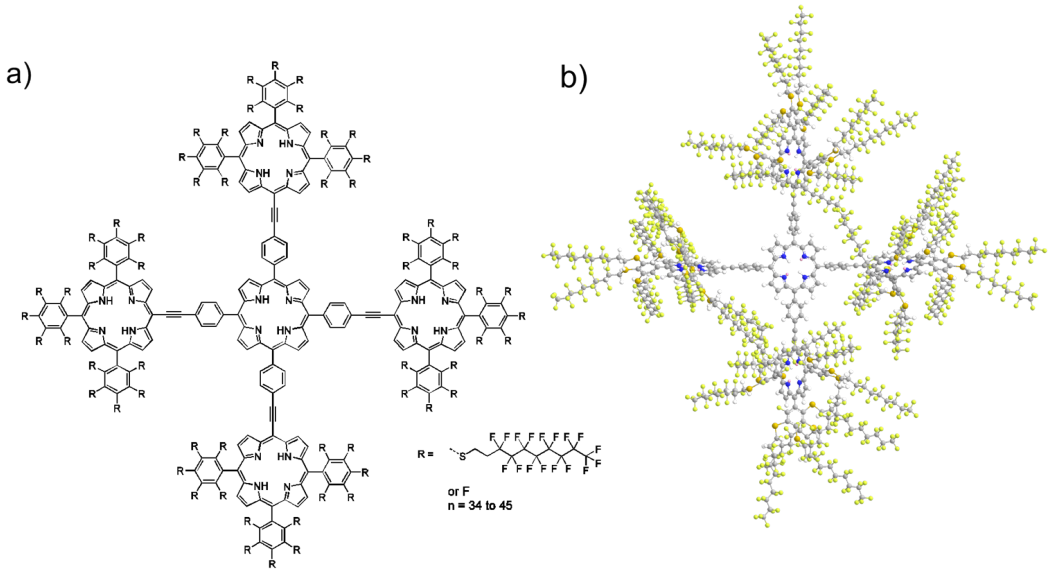

Figure 4.2: Shown is the molecular structure of $\mathrm{TPP(TPP)_4F_{60+16x}}$. Panel a) is a schematic drawing of the tetraporphyrin system reaching a mass of up to 25 kDa. Maximally 45 attached perfluorooctyl chains are detected in the mass spectrum. To the right a three dimensional drawing of the same molecule at an equilibrium temperature of 700K is shown. This structure is again calculated with the MM2 package of ChemBio3D Ultra.

4.1.2 $\mathrm{TPP(TPP)_4F_{60+16x}}$

A comparison of the two molecular libraries $\mathrm{(ZnTPPF)_4F_{60+16x}}$ 4.1 and $\mathrm{TPP(TPP)_4F_{60+16x}}$ 4.2 reveals some differences. Both of them contain a "ring" of four tetraphenylporphyrins, but the central unit is different. $\mathrm{TPP(TPP)_4F_{60+16x}}$ possesses another TPP in the centre, turning the whole molecule into a fully conjugated system, whereas in the case of $\mathrm{(ZnTPPF)_4F_{60+16x}}$ the conjugation is broken through the tetraphenylmethane subunit. Additionally it turned out that attaching a high number of perfluorooctyl chains (up to 45) to the polyporphyrin is easier without a metal atom. Each of the two cores described here can contain up to 60 side chains. Theoretically, all fluorine atoms at all phenyl rings can be substituted. In reality this is not the case, because of steric hindrance. This can be understood by considering typical bond lengths: In contrast to sp3 carbon-hydrogen bonds with a typical length of 109 pm, carbon fluorine bonds are considerably larger (135 pm). Therefore they are sterically more space demanding [109, 124]. Additionally a perfluorooctyl chain can be regarded as a positively charged carbon backbone with a negative fluorine cloud, since the C-F bond is strongly polarized. This leads to electrostatic repulsion [109, 124].

4.2 Mass spectra

4.2.1 Mass distribution of the $(\mathrm{ZnTPPF})_4\mathrm{F}_{60+16\mathrm{x}}$ library

Matrix free laser desorption of $(\mathrm{ZnTPPF})_4\mathrm{F}_{60+16\mathrm{x}}$ led to a molecular plume which was intersected by the VUV post-ionization laser (see figure 3.3). At a fixed delay between the nitrogen laser and the 157 nm laser, a mass spectrum was recorded. This delay (ca. 400 μs) was chosen so that the signal intensity is at its maximum. Furthermore, the intensity of the post-ionization laser was also optimized according to the molecular intensity (approximately 200 μJ). Under these conditions the mass spectrum was averaged over 30 laser shots. An example of the mass spectrum of $(\mathrm{ZnTPPF})_4\mathrm{F}_{60+16\mathrm{x}}$ is shown in figure 4.3. The collected data shows significant components between 1 to 5000 Da and between 10 kDa and 14 kDa.

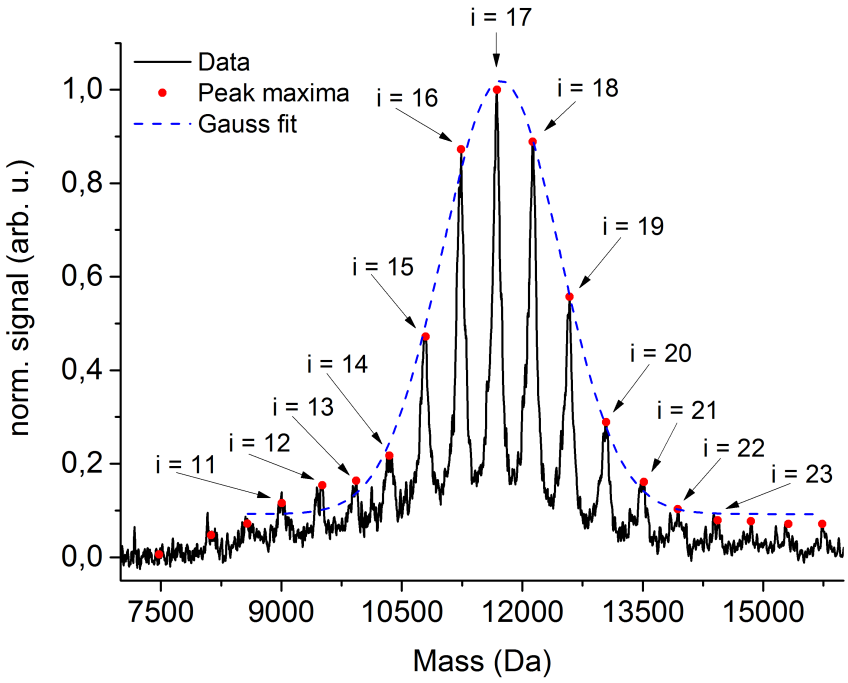

Figure 4.3: The high mass component of the mass spectrum of the molecular library $(\mathrm{ZnTPPF})_4\mathrm{F}_{60+16\mathrm{x}}$. The maxima of the mass peaks are emphasized by red dots, which are fitted by a Gaussian (dashed blue line) in order to see how well the molecular distribution in the library can be described through this model. Peaks from 8000 to 16000 Da are still resolvable. For further explanation, see text.

Number of perflouroalkylated chains	Mass (Da) $\pm$ mass error ($\Delta m/m \approx 1/100$)
14	10342 ± 104
15	10782 ± 108
16	11232 ± 113
17	11676 ± 117
18	12134 ± 122
19	12575 ± 126
20	13041 ± 131
21	13492 ± 135

Table 4.1: Mass peaks of $\mathrm{TPP(TPP)_4F_{60+16x}}$

Figure 4.3 shows a typical mass/charge spectrum of the $\mathrm{(ZnTPPF)_4F_{60+16x}}$ library. All spectra shown in these sections are formed by molecules which are photoionized. Only single charged ions are most probable to occur reducing m/z to m. Higher charges would reduce the separation between peaks by the factor m/z. Peaks highlighted by the red dots represent different numbers of perfluorooctyl chains attached to the central core of the molecule (see figure 4.1). The respective masses are listed in table 4.1. As shown in figure 4.3 the central unit with 11 to 23 perfluorinated side chains can be detected. This corresponds to a mean number of 1.5 side chains per phenyl moiety. For measurements of velocity or ionization efficiencies, only $i = 14$ to $i = 21$ were taken into consideration, since they had the best signal to noise ratio for a reliable analysis. One eye-catching property of this mass spectrum is the Gaussian envelope of the peak maxima (dashed blue line in figure 4.3). This is a result of the synthesis, since the side chain attachment is a probabilistic event [108]. One would expect a Poisson distribution because the side chain attachement is likely to be a single event and not a collective process. However Poisson statistics only holds if the events are independent of each other, which is not the case here, since electrostatic repulsion and steric hindrance can significantly contribute to the decision of the attachment position. Because of electrostatic repulsion and steric hindrance, molecules with 12 side chains should build up the strongest signal, because it is more likely that all para positions of the phenyl rings are occupied at first (see figure 4.4). According to ref.[109] this is due to the fact that nucleophilic aromatic substitution is preferentially done in the para-position at first. Then the meta positions of the phenyl groups are filled (see section 4.1). However, the most abundant peak in our case is formed by molecules with 17 side chains. So the expectation described previously doesn't occur.

[15]Figure was taken from URL: `http://en.wikipedia.org/wiki/Arene_substitution_pattern#mediaviewer/File:Ortho-meta-para.svg` (30.06.2014)

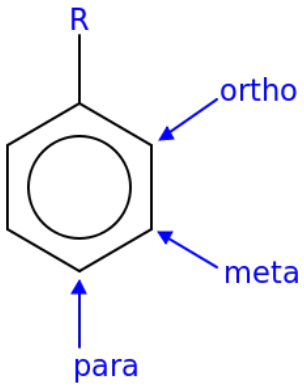

Figure 4.4: The explanation of the para, meta and ortho position of functional groups on a phenyl ring. [15]

Apart from that, another remarkable feature of the mass spectrum in figure 4.3 is the separation of the peaks. The peaks are separated by 450 ± 10 Da. This value is the avarage over all distances between neighboring peaks and the error represents the standard deviation. Perfluorooctyl $SC_2H_4(C_8F_{17})$ has a nominal mass of 479 Da. A fluorine chain can only be attached if a fluorine atom (19 Da) is removed from the phenyl rings. This yields a mass increase of only 460 Da. Thus the measured peak distance is compatible with our expectations.

Some fundamental questions on the desorption process arise in the low mass regime of the mass spectrum as shown in figure 4.5.

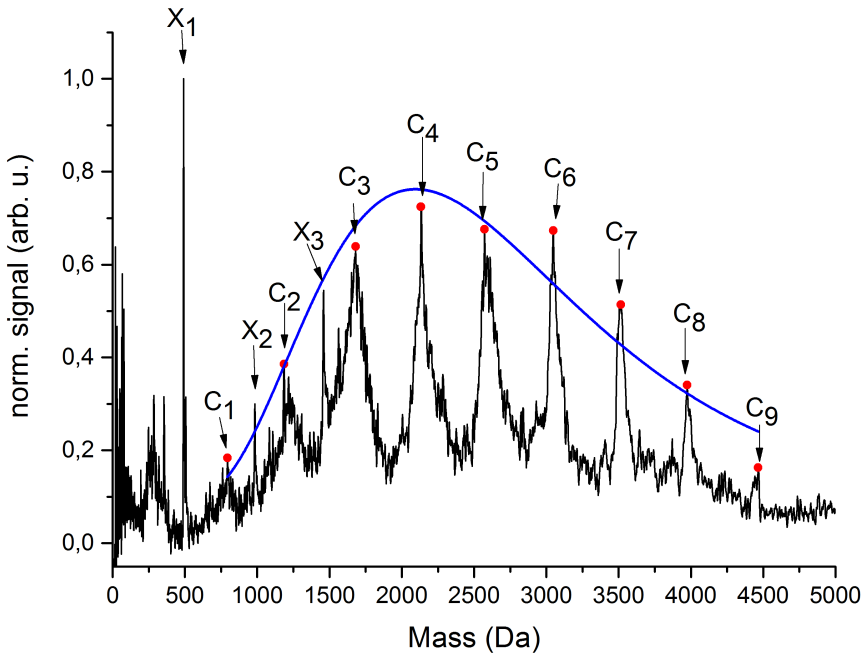

Figure 4.5: Low mass regime of the mass spectrum of $(\mathrm{ZnTPPF})_4\mathrm{F}_{60+16\mathrm{x}}$. X_1 denotes the mass speak of a single perfluoroalkyl chain. C_1 to C_9 are separated each by a mass of a side chain. This is a strong indication for clusters of chains formed during the expansion of the molecular plume. For further information, see text.

Peak label	Mass (Da) $\pm$ mass error ($\Delta m/m \approx 1/100$)
X_1	490 ± 5
C_1	796 ± 8
X_2	983 ± 10
C_2	1217 ± 13
X_3	1459 ± 15
C_3	1678 ± 17
C_4	2136 ± 22
C_5	2580 ± 26
C_6	3045 ± 31
C_7	3506 ± 36
C_8	3976 ± 40
C_9	4451 ± 45

Table 4.2: Mass peaks of $\mathrm{TPP(TPP)}_4\mathrm{F}_{60+16\mathrm{x}}$

This regime looks similar to the spectrum of the intact molecular library. However, here we used a LogNormal function to describe the shape of the distribution. This fit approximates the curve much better than a simple Gaussian. In literature it is argumented that LogNormal distributions often occur in clustering processes [125].

We think that this process may also explain our observation in the low mass regime (figure 4.2). The respective masses are listed in table 4.2. Here X_1 is the mass peak of a single perfluorooctyl side chain. It is surprising that the side chain can be observed, since its photoionization is unlikely due to the lack of an ionization centre. It was shown previously [126] that perfluoroalkyl chains can undergo a resonance enhanced two photon ionization if a chromophore is attached. From that we assume that the ionization of the fluorinated chains is indirect via fragmentation-induced charge transfer. Another astonishing fact is the appearance of the peaks C_1 to C_9. They are separated from each other by a molecular mass of (457 ± 18) Da. This fits reasonably well with the nominal mass of a single perfluoroalkyl chain. However, the question is how these masses are formed. One may think that these peaks represent a TPP unit or a fragment thereof with attached fluorinated chains. The number of chains would then vary from one to at least nine. Indeed, previous work shows that photo dissociation of TPPs is possible [117], preferentially leading to the cleavage of a phenyl unit. This assumption leads, however to some inconsistencies. The mass of peak C_1 would correspond to one TPP with one perfluoroalkyl chain and only hydrogen atoms in the rest of the possible positions instead of fluorine atoms (see structure in figure 4.1). This is very unlikely to happen, both during synthesis and in the desorption process. If it were a result of the chemical production, these peaks would also be observable with MALDI, but they aren′t. Furthermore, also a TPP without a side chain would have to appear in the mass spectrum, but no peak is observed at the relevant mass. X_2 is the only peak which can be caused by fluorinated TPP (see table 4.2), but then the addition of a single side chain does not lead to the observed peaks between C_1 up to C_9. Another strong inconsistency is the fact that the position of the peaks C_1 to C_9, the shape and centre of the envelope of hereof are the same for different molecules ($(\mathrm{ZnTPPF})_4\mathrm{F}_{60+16\mathrm{x}}$, $\mathrm{TPP}(\mathrm{TPP})_4\mathrm{F}_{60+16\mathrm{x}}$ and the previous library generation $\mathrm{TPPF}_{20-\mathrm{x}+17\mathrm{x}}$ [78]). If the peaks resulted from photofragmentation, the centre of the distribution would have to change, as there is an obvious difference in the number of attached chains between the different kinds of libraries.

Our hypothesis is therefore that these peaks are a result of side chain clustering, which may occur in the hot and dense desorption plume. Indeed, the occurrence of van der Waals clusters in MALDI plumes have been reported in various earlier experiments [36, 127].

4.2.2 Mass spectra of $\mathrm{TPP(TPP)_4F_{60+16x}}$

As our primary goal is to increase the mass limit in interferometers, our collaborators in Basel designed a perfluoroalkylated pentaporphyrin system $\mathrm{TPP(TPP)_4F_{60+16x}}$. With the sample preparation method described in the section 3.4, a mass spectrum of this molecular library was recorded. Here the ionization laser energy was 1.4 mJ. With these settings the spectrum was averaged over 30 shots. The result is shown in figure 4.6.

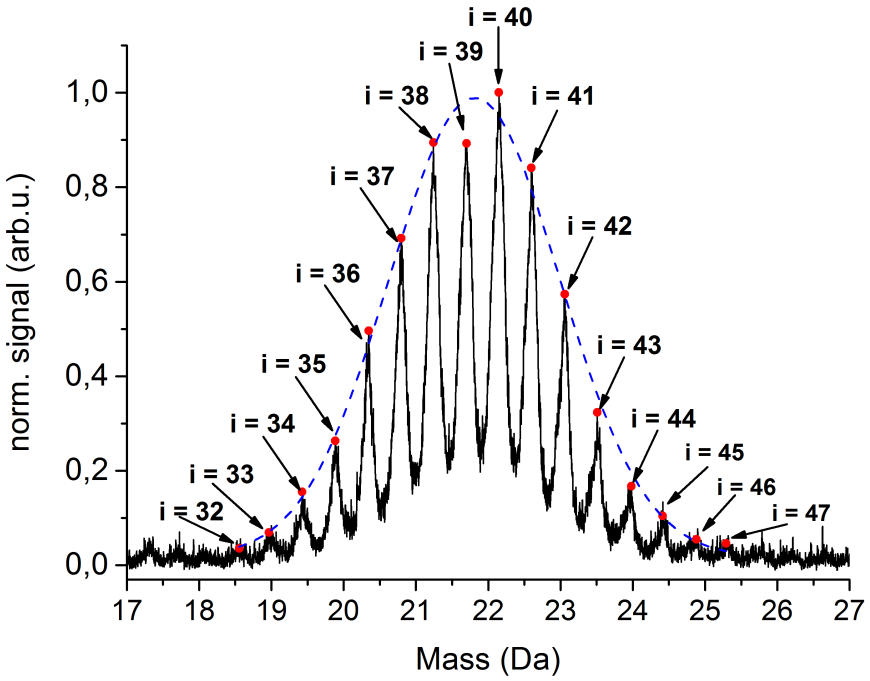

Figure 4.6: Mass spectrum of $\mathrm{TPP(TPP)_4F_{60+16x}}$.The different peaks represent molecules with different number of side chains of the same library. Molecules of up to 25000 Da can be detected. The maxima of the peaks are marked by red dots. These points are then fitted by a Gaussian distribution (dashed blue line).

Number of attached perflouroalkylated chains	Mass (Da) $\pm$ mass error ($\Delta m/m \approx 1/100$)
34	19431 ± 195
35	19894 ± 200
36	20345 ± 204
37	20801 ± 209
38	21245 ± 213
39	21700 ± 220
40	22152 ± 222
41	22609 ± 227
42	23062 ± 231
43	23522 ± 236
44	23977 ± 240
45	24418 ± 245

Table 4.3: Mass peaks of $\mathrm{TPP(TPP)_4F_{60+16x}}$

The most abundant peak is situated at 22152 Da, however here this peak is not simultaneously the central peak, as it is the case in figure 4.6. This slight asymmetry arises again from the synthesis as explained in the previous section. All of the peaks have a mass separation of 453 ± 7 Da corresponding to the nominal mass of the side chain (479 Da) minus a fluorine atom, which is replaced. A comparison with $\mathrm{(ZnTPPF)_4F_{60+16x}}$ shows that this value is more precise. This may be ascribed either to the better instrumental conditions (e.g. better focussing) or to molecular properties (lower probability for fragmentation) during the recording of the mass spectrum.

4.3 Velocity distribution

The de Broglie wavelength scales inversely proportional to the momentum of the particle. In order to be able to resolve the interference pattern, it is therefore necessary to achieve a low forward velocity to allow high masses to interfere in the current interferometer setups. Not every desorption technique is applicable to matter-wave interferometry. Molecular beams of $\mathrm{(ZnTPPF)_4F_{60+16x}}$ and $\mathrm{TPP(TPP)_4F_{60+16x}}$ were formed via matrix-free laser desorption of the molecular powder on a steel plate and the velocity distributions were recorded. This was done by varying the time delay between the desorption laser (nitrogen laser) and the post-ionization laser (fluorine laser). Although we are mostly interested in neutral particles there are still ions in the molecular plume. This is consistent with some observations in the literature [128, 129]. We used a delayed extraction technique [36, 73] to ascertain their velocities as described in section 3.3.

Both in KDTLI and OTIMA, there are restrictions to the velocity of the molecular beam described in the section 2.1.4.

4.3.1 Time of flight distribution of $\mathrm{TPP(TPP)_4F_{60+16x}}$

The delay between the desorption laser pulse and the photoionization laser was scanned from 0 to 2 ms. Within this window we were able to observe two components of the velocity distribution (a bimodal distribution), a faster and a slower part separated for better clarity. In figure 4.7 and 4.8 the time of flight distribution of $\mathrm{(ZnTPPF)_4F_{60+16x}}$ is shown. The distribution reveals that there are two components leading to a bimodal velocity distribution. This is in particular true for $\mathrm{(ZnTPPF)_4F_{60+16x}}$ as well as for $\mathrm{TPP(TPP)_4F_{60+16x}}$.

The fast component

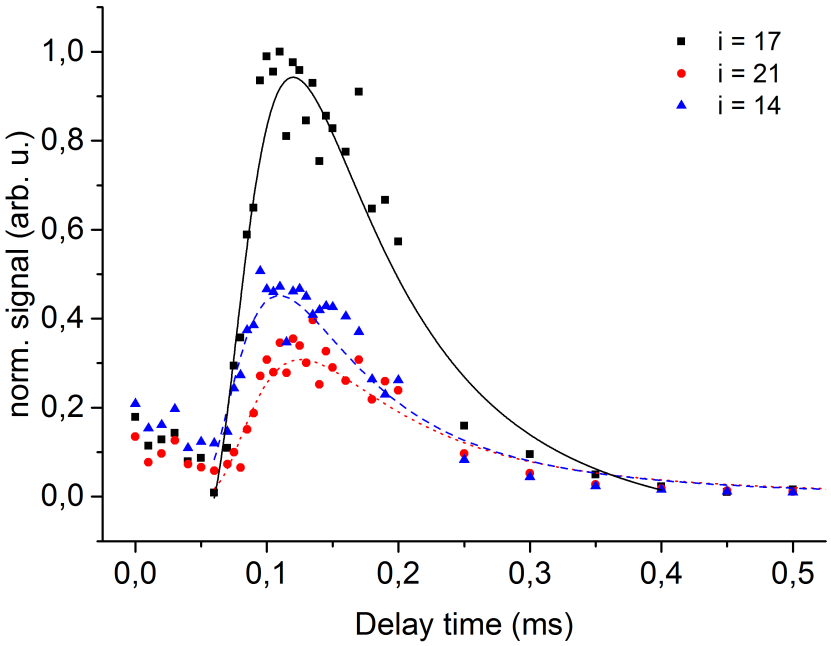

Figure 4.7: Time of flight distribution of in-source created $\mathrm{(ZnTPPF)_4F_{60+16x}}$ ions. As the post-ionization laser was not used, the delay between ion ejection and desorption was realized by the delayed extraction technique. Hereby the opening time of the repeller was controlled. Different symbols represent different numbers of attached perfluorooctyl side chains, whereas the solid, dashed and dotted lines are the respective Maxwell-Boltzmann fits. For the resulting values of the velocities, see text.

In figure 4.7 the direct ions were detected (i.e. with F_2 laser off) and the time of flight distribution could be recorded via the delayed extraction technique. For the different number of side chains ($i = 14$, $i = 17$ and $i = 21$) the most probable velocity was extracted through a Maxwell-Boltzmann fit (see equation equation 2.8). The reason why we use a Maxwell-Boltzmann distribution will be discussed in the upcoming section. The results are summarized in table 4.4. Although there seems to be an increase in velocity with decreasing

Number of chains (i)	Most probable velocity (m/s)	Translational temperature (K)
14	291 ± 6	52800 ± 2100
15	264 ± 4	48700 ± 1400
16	253 ± 6	51900 ± 2200

Table 4.4: Results of the Maxwell-Boltzmann fit for $(\mathrm{ZnTPPF})_4\mathrm{F}_{60+16\mathrm{x}}$ generated by matrix-free laser desorption ionization. The error bars directly result from the fit.

mass (see table 4.4) in the case of $(\mathrm{ZnTPPF})_4\mathrm{F}_{60+16\mathrm{x}}$, we believe that this observation is only true for this specific kind of molecule as for $\mathrm{TPP(TPP)}_4\mathrm{F}_{60+16\mathrm{x}}$ this statement doesn$'$t hold. Other experiments and molecular dynamics simulations also showed the independence of velocity on mass [36, 42, 130, 131]. The individual temperatures listed in table 4.4 are extracted from the Maxwell-Boltzmann fit. Also in the literature values in excess of 1000 K have been reported for small molecules (up to several hundreds of Dalton) [36, 132, 133].

The neutral and slower component

There is a slower component that we only observe after post-ionization of the neutral molecules. This is shown in figure 4.8. The velocities for each molecule with a certain number of attached perfluoroalkyl can be extracted from the data of figure 4.8. This is done by fitting the traveling time of the particles from the sample surface to the ionization volume (roughly 3.9 cm) with a Gauss function as it suits better than the Maxwell-Boltzmann fit. The peak of this fit results in a velocity. Figure 4.9 displays the velocities for different number of side chains. Actually one would expect a slight decrease for higher masses, as more desorption energy is needed to volatilize heavier particles due to the increased intermolecular van der Waals interactions. This results in a smaller fraction of the laser energy converted into kinetic energy of the molecules. In figure 4.9 we fitted the data points with a linear function. As one can see there is a slight decrease with a slope of $(-0.4 \pm 0.6)\ m/s$, however the error is too large to make a conclusive statement.

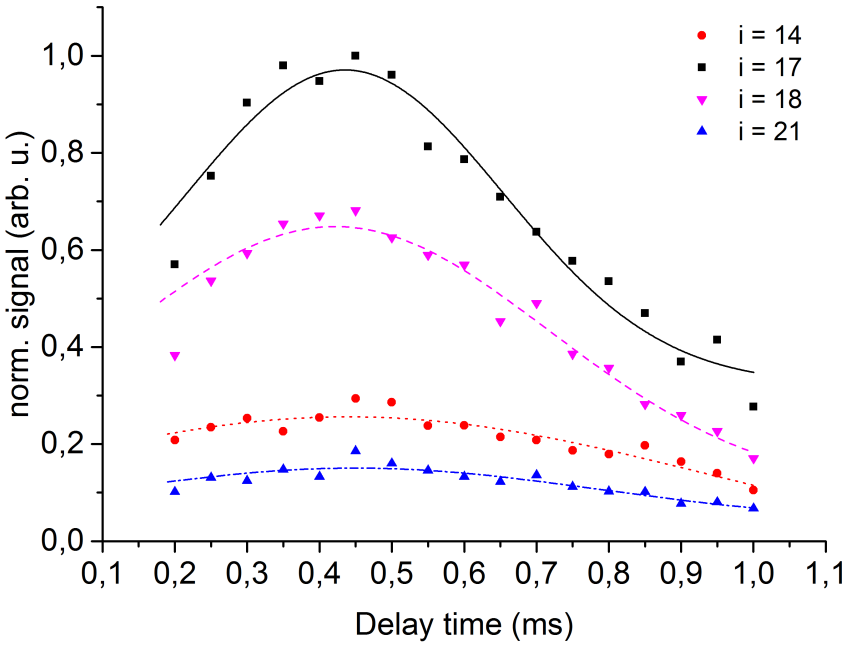

Figure 4.8: The slow component of the time of flight distribution of $(\mathrm{ZnTPPF})_4\mathrm{F}_{60+16x}$. The different symbols represent different number of attached side chains and they are fitted by a Gauss function. Here, all the data points are **post-ionized neutral** molecules. Solid lines represent Gauss fits.

Experiments in literature in which the velocities of MALDI-ions have been determined, state that there is no dependence between the velocities and the masses [36, 134, 130]. Comparing the data shown in figure 4.8 with figure 4.11 raises new questions:

1. Why are the neutral post-ionized molecules slower than those which are directly ionized during the desorption process?

2. Why is there a bimodal velocity distribution?

3. Why is the velocity distribution for the neutrals (figure 4.8) broader than for the ions?

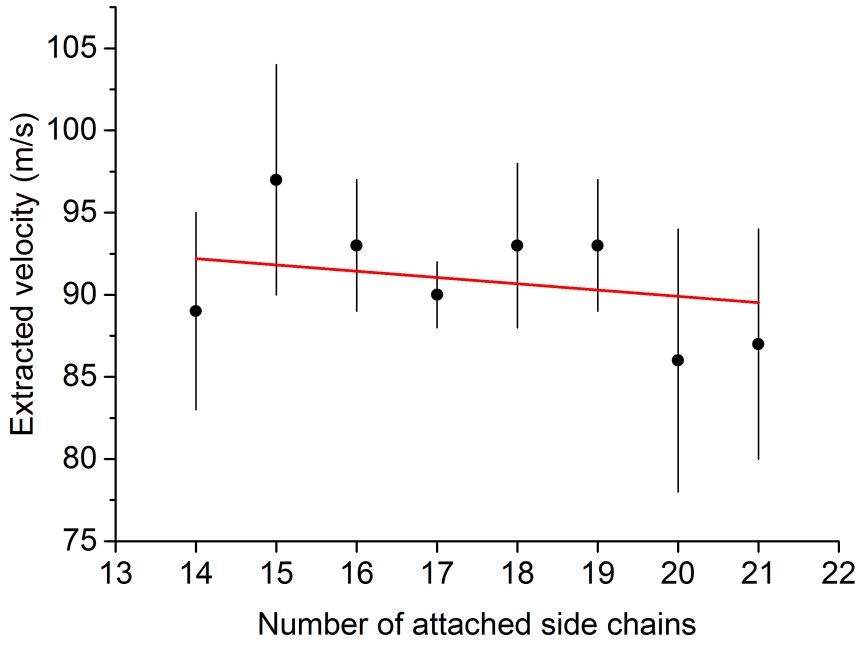

Figure 4.9: Molecular velocity in dependence of the number of side chains. As shown, the extracted velocity values are quite similar within the error bars.

4. How can we justify the fitting with a Maxwell-Boltzmann distribution or a Gauss function?

Before I attempt to answer these questions, it should be noted that these problems listed above are still a subject of research [36]. Therefore, only a qualitative discussion of the desorption process can be given as these are highly complex phenomena, which depend on the physicochemical properties of the compounds. Nevertheless, several valid theories for answering the questions shall be discussed.

According to Dreisewerd et al. [36], velocities of neutral post-ionized molecules are remarkably lower than for ions created during the laser desorption. It is not reasonable to give a number, since the velocities will strongly depend on the type of molecules. The same phenomenon was also observed in ref. [36, 57, 58] where the authors performed absorption spectroscopy on the molecular plume and concluded that the front part of the ejected plume mainly consists of hotter analyte ions. In laser desorption it has been argued that the molecules which are directly exposed to the laser will have a free-jet expansion character. With this argument the higher velocities of the ions can be understood.

However, one has to add that the velocities in MALDI or LDI for the ions are generally lower compared to supersonic expansion sources. This can be explained through the fact that in the early stage of the plume many collisions between the molecules can occur which could lead to collisional cooling. This phenomenon will be adressed later. Apart from that, molecular dynamics simulations showed that the axial velocities strongly depend on the initial position of the analyte molecules inside the molecular powder on the target plate [131]. Molecules at the surface have larger velocities than those which are deeply embedded in the molecular crystal [42]. This observation alone shows already that the explanation of the bimodal character of the velocity distribution is a nontrivial task. Another eye catching effect is the broad velocity distribution in figure 4.8. In the case of a Maxwell-Boltzmann distribution the width is determined by the temperature of the molecular cloud, but here Gauss functions were used for fitting. One possible explanation of the broad distribution could be related to the fact that even large ensembles of molecules can be lifted into the gas phase during laser desorption. As it was shown in ref. [42], desorption of clusters of analyte molecules is possible if the laser fluence is chosen appropriately. For lower laser intensities only single isolated molecules are ejected, whereas for higher laser fluences also clusters of up to ten molecules can be volatilized [40]. As the cluster size is not uniform but will rather have a distribution, also their velocities will have a broad distribution and in general they will be lower than the velocity of the ions. This could explain the rather broad distribution. In that context, however, the question arises whether it is possible to see the different clusters in the mass spectra, as they must have different masses. In our experiments we couldn′t do any related observations. To address the last question, it should be mentioned that for the fast part a modified Maxwell-Boltzmann distribution is also applicable. The modification includes the so called stream velocity [36], which takes into account that the molecular plume is generally forward directed. However, we use the common Maxwell distribution (equation 2.8). The stream velocity is introduced for the description of the faster part of the molecular plume. For the slow part of the time of flight distribution we use a Gauss function (figure 4.8). Since we are mainly interested in the measurement of the most probable and the lowest velocity of the molecular cloud any time of flight distribution gives a reasonable value.

4.3.2 Time of flight distribution of $\mathrm{TPP(TPP)_4F_{60+16x}}$

Velocity of the ionic component

Also the mass spectra of $\mathrm{TPP(TPP)_4F_{60+16x}}$ exhibit molecular ions already created in the desorption process. The most probable velocity of these ions (in figure 4.10) is $270 \pm 4\ m/s$.

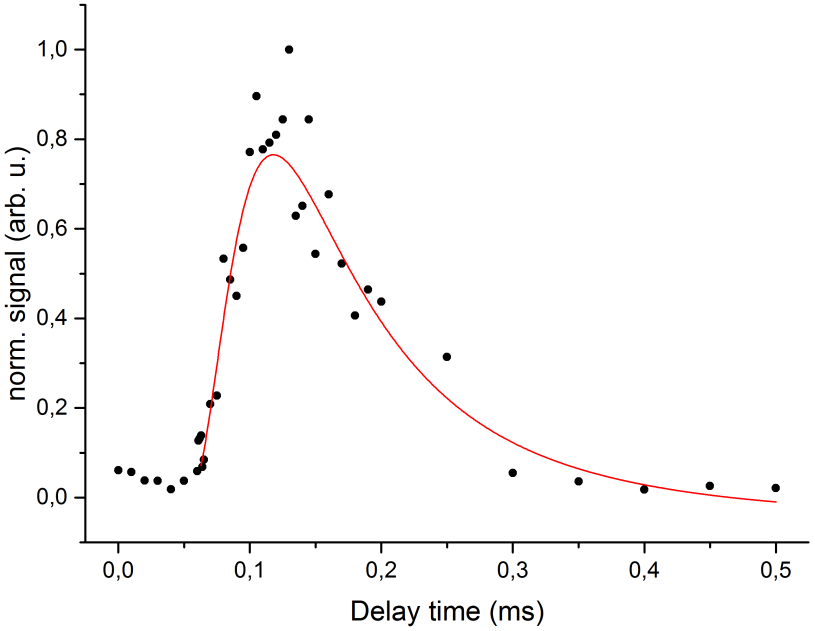

Figure 4.10: Ionic component of the velocity distribution of $\mathrm{TPP(TPP)_4F_{60+16x}}$ (i=40). At a distance of 3.9 cm from sample to the ion extraction region, the most probable time of flight is roughly 800 μs. Fitting the data with a Maxwell-Boltzman distribution yields a most probable velocity of 270 ± 4 m/s.

The graph represents $\mathrm{TPP(TPP)_4F_{60+16x}}$ with 40 side chains, however for the elements of the same molecular library the velocity remains more or less the same.

Down to 20 m/s and below...

As before the heavier molecules show a bimodal velocity distribution. The slow component is shown in figure 4.11.

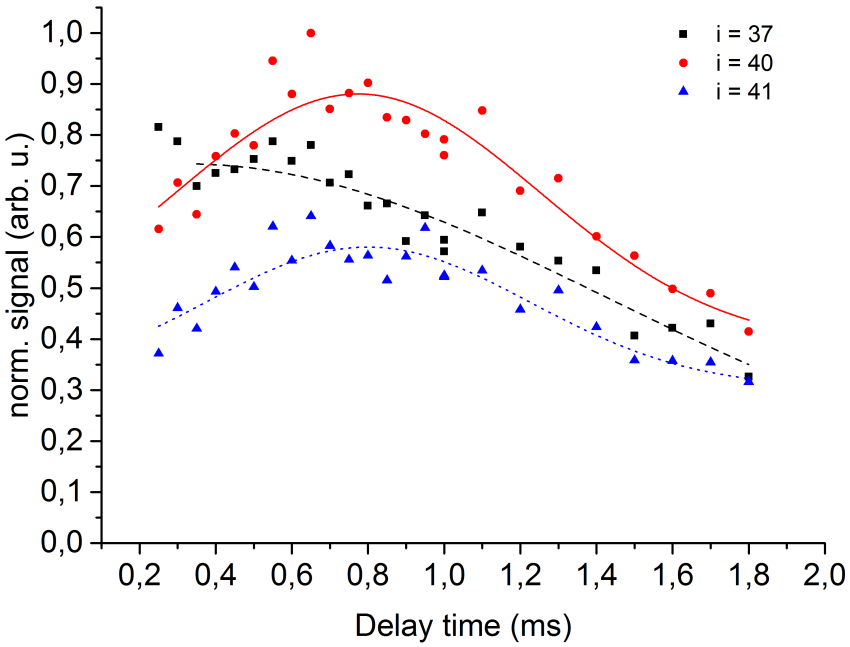

Figure 4.11: Slow part of the velocity distribution of $\mathrm{TPP(TPP)_4F_{60+16x}}$. Distinct symbols represent different number of perfluoroalkyl chains attached to the pentaporphyrin core. The lines represent Gauss fits to the data, as Max Boltzmann fits didn't represent the data well. Attention should be given to the fact that even at ≈ 2 ms, still a signal can be detected. This corresponds to a velocity value of roughly 20 m/s.

A comparison of figure 4.11 with figure 4.8 shows that the shape of the slow component is quite similar for certain numbers of perfluorooctyl chains. The fast component is separated from the slow part by a dip in the signal. However, in the case of $\mathrm{TPP(TPP)_4F_{60+16x}}$ this is not always true. For $i = 37$ for example it seems that the ionic component is merged together with the slow part, which makes the dip invisible. These data points can not be well fitted with a Gaussian (see black dashed line in figure 4.11), as it will result in large error bars. Nevertheless, regarding the time of flight distributions for all elements, one can see that the peak of the Gaussian, which corresponds to the mean velocity, is quite similar, consistent with figure 4.9. Another common observation is the existence of the broad slow part of the velocity distribution, similar to section 4.3.1. A closer look at figure 4.11 reveals that at delay times as large as 2 ms we can still measure neutral molecules. This delay corresponds to $v = 20\ m/s$.

4.4 A plume experiment

In this part I will focus on the transversal velocity and the plume shape of laser desorption. There have been experimental attempts in the previous decades to image the molecular plume [57, 58]. This can be done through many techniques, however among them laser induced fluorescence is the most common one. In ref. [57, 58] fluorescent molecules of various masses are desorbed and the plume is probed by an excitation laser with the appropriate wavelength. The emitted photons are then collected by a sensitive camera. From these experiments one can deduce the plume dynamics, e.g. the opening angle. Knowledge about the dynamics and shape of the molecular plume can be of essential interest, when it comes to the optimization of the desorption process. As an example, sharpening of the plume (= reduction of the plume opening angle) will not only increase the overall signal intensity, but it can also lead to an improvement of the resolution of mass spectra. Here we restricted ourselves to a simple but informative experiment to gain information about the desorption plume: For that a microscope slide was sonicated in acetone and plasma cleaned for ten minutes, in order to remove dust particles. Then it was placed between the repeller plates of the ToF-MS, as depicted in figure 3.3a. This guarantees a distance Δl of 3.6 cm to the sample surface. After evacuating the chamber, 20000 shots with the nitrogen laser were executed and the ejected particles were collected on the glass plate. The molecular plume shown in figure 4.12 possesses a slightly elliptical shape. Since the laser hits the sample surface under an angle of roughly 30 degrees, the beam shape on the sample target is slightly oval. This leads to the elliptical cross section of the molecular beam. An image analysis, where only the diagonal of the plume is examined, leads to a nearly Gaussian intensity distribution. This is shown in Figure 4.12b. For that the camera image was imported into Mathematica. Then the pixel position of the maximum intensity value was extracted. The intensity of the pixels which define the cross-section of the ellipse (red line in figure 4.12a) was plotted. This led to the cross section of the plume. To these data points a Gaussian function was fitted (red line in figure 4.12b):

$$f(x) = \frac{A}{\sigma\sqrt{2\cdot\pi}} \cdot exp\left(-\frac{(x-\mu)^2}{2\cdot\sigma^2}\right) \tag{4.1}$$

where A is a proportionality constant, σ the standard deviation and μ the expected value. As a scale bar is present in panel a), the conversion from the number of pixels into a real physical linear measure can be made.

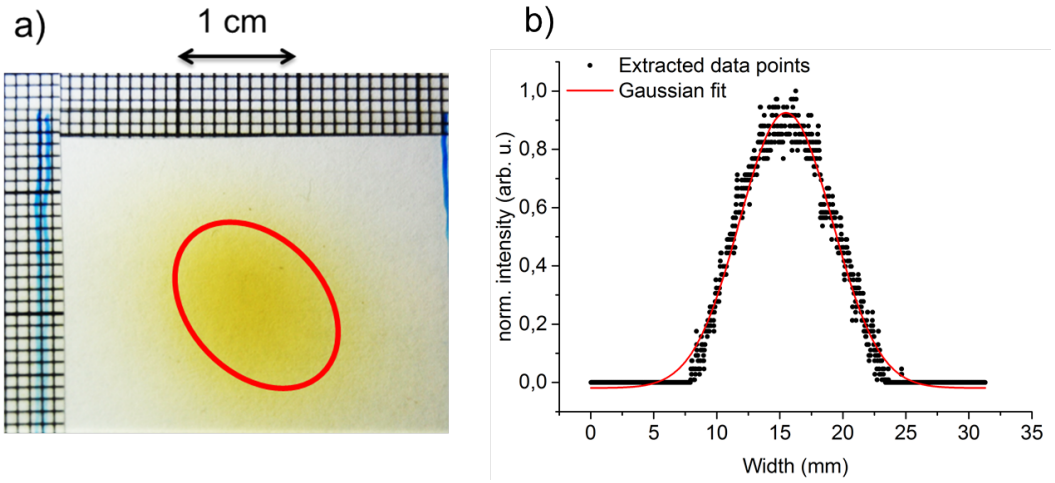

Figure 4.12: This figure shows a plume analysis of the laser desorbed $\mathrm{TPP(TPP)_4F_{60+16x}}$ molecules. Panel a) shows the appearance of the collected particles. No microscope was used and the photo was taken by a reflex camera. Millimetre papers were used as scale bars. Panel b): diagonal cross section of the plume is presented (black dots). The data points were fitted with a Gaussian (see equation 4.1) to determine the full width at half maximum (FWHM). From that the maximum divergence angle of the plume can be deduced. We calculated $13.8° \pm 0.2°$.

Together with the Gaussian fit, this results in a full width at half maximum (FWHM) of (8.7 ± 0.1) mm. With this, we can calculate the full divergence angle of the plume. This is given by the following formula:

$$tan\left(\frac{\theta}{2}\right) = \frac{FWHM}{2 \cdot \Delta l} \rightarrow \theta_{full} = 13.8° \pm 0.2° \tag{4.2}$$

Plume angles of laser desorbed molecule clouds have also been carried out by other groups. In ref. [49] for example, the authors found that Cytochrome C proteins desorbed from an ice matrix have a full open angle of roughly $40°$. Others [58] found that heavy molecules tend to undergo plume sharpening, several microseconds after desorption. One argument against the simple plume imaging technique applied here is the fact that molecules, which are collected on the microscope slide can also be fragments. This could lead to a wrong FWHM of the plume and to a wrong angular distribution. However, considering the whole mass spectrum of the particles (figure 4.5 and figure 4.3), this assumption seems no to be true, as only clusters of the perfluorooctyl chains could be observed in the mass spectrum which don't have any color. For matter-wave interferometers the divergence of the molecular should be smaller than 1 mrad (see section 2.1.1). This is one of the reasons why many delimiters are needed and used in our experiments.

We are currently working on techniques which could sharpen the molecular plume. We expect also an increase of the signal [52]. Many ideas have been developed for lowering the transversal translation temperature [16] and the collimation angle of the molecular beam. One idea which will be soon tested is the so called micro-well assisted laser desorption. Here, the idea is to use a sample plate, on which well-defined micro channels are etched. The molecular solution is then dropped into these channels, so that the molecular plume is constrained and forced to evolve under a narrower opening angle. This is shown in figure 4.13. The expected plume sharpening effect has been modelled and verified in ref.

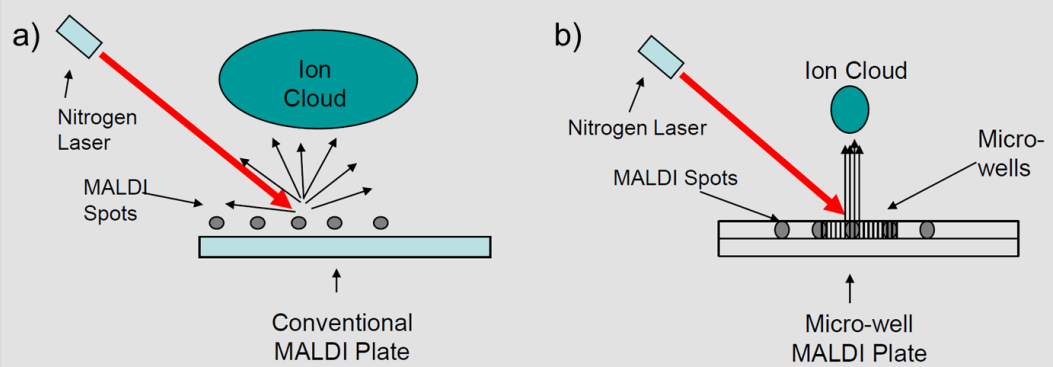

Figure 4.13: With a conventional sample target (a) the ejected molecular plume has a larger spatial elongation, whereas the molecular cloud desorbed from micro-well plates is much more directed towards the detection region. [16]

[135]. The authors simulated substrates with micro channels of high aspect ratio resembling capillary nozzles. It was shown that the plume gets more directed towards the detection region, but it was also observed that the molecular velocity increases with growing aspect ratio of the channels. Especially with regard to $\mathrm{TPP(TPP)_4F_{60+16x}}$ this method could help to increase the signal intensity, which would pave the way for a successful interferometry experiment. As the velocity of these molecules is lower than 40 m/s, one can easily cope with a faster molecular plume as a result of the sharpening effect from micro-well plates. Also the optimization can be done easily, as these plates are commercially [17] available in different sizes.

[16] Figure was taken from Photonis, Inc. URL: `http://www.photonis.com/en/`
[17] Photonis, Inc. URL: `http://www.photonis.com/en/ism/41-micro-pore-optics.html`

4.5 Optimization of the desorption laser power

The enhancement of the signal intensity can be done through various ways. In this section, we describe how the signal was optimized by varying the laser pulse energy. Since the nitrogen laser has a limited range (0...90 μJ), the third harmonics of a Nd:YAG laser was aligned and used for desorption. The pulse energy was adjusted by a polarization filter in the beam path. A reproducible power value could be set in steps of ten micro joules. In the following, desorption studies on $(\mathrm{ZnTPPF})_4\mathrm{F}_{60+16\mathrm{x}}$ as well as on $\mathrm{TPP}(\mathrm{TPP})_4\mathrm{F}_{60+16\mathrm{x}}$ will be presented and discussed.

4.5.1 The optimal desorption power for $(\mathrm{ZnTPPF})_4\mathrm{F}_{60+16\mathrm{x}}$

The following study aims not only at the enhancement of the signal intensity but it can also deliver valuable information about the thermal stability of the respective particle. The sample target plate was prepared in exactly the same way, as it is described in section 3.4. Here the desorption laser energy was varied, but the post-ionization energy was kept constant. In the case of $(\mathrm{ZnTPPF})_4\mathrm{F}_{60+16\mathrm{x}}$, the ionizing laser is set to ≈ 400 μJ. This is important, as the signal intensity variations can only be caused by the variation of the desorption energy. The signal with respect to the desorption laser power density for $(\mathrm{ZnTPPF})_4\mathrm{F}_{60+16\mathrm{x}}$ is shown in figure 4.14. The signal values for different side chain numbers at the same desorption laser intensity come from the same mass spectrum. Thus for them the experimental conditions were the same. For clarity the error bars of the desorption laser intensity are not included, however for the third harmonics of a Nd:YAG laser we measure 10% deviations of the laser pulse energy. The laser spot on the sample target has a dimension of 1.2 x 0.3 mm. One can divide figure 4.14 into two major components. First the signal increases with increasing desorption laser power and then, after reaching a saturation point, it falls off due to fragmentation of the molecules. Such types of studies were also made with matrix assisted laser desorption [36, 41].

4.5.2 The optimal desorption power for $\mathrm{TPP}(\mathrm{TPP})_4\mathrm{F}_{60+16\mathrm{x}}$

Variation of the desorption laser power was also done for $\mathrm{TPP}(\mathrm{TPP})_4\mathrm{F}_{60+16\mathrm{x}}$. The sample preparation is the same, as described in section 3.4.

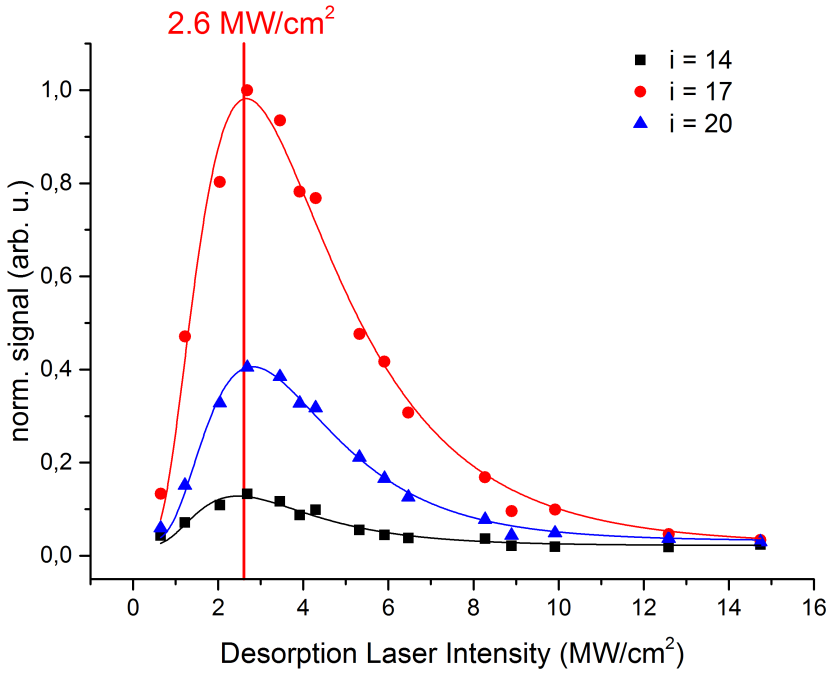

Figure 4.14: The signal of $(\mathrm{ZnTPPF})_4\mathrm{F}_{60+16\mathrm{x}}$ vs. the desorption laser power density. Different symbols represent molecules with differing number of attached perfluorooctyl side chains. As shown, the intensity increases with different slopes up to a saturation point. Further increase, however, results in fragementation. Solid lines are to guide the eye.

Here the laser energy for photoionization is set to 1.2 mJ and each mass spectrum is a sum over 90 shots. The result is depicted in figure 4.15. Comparing the desorption yield of $\mathrm{TPP(TPP)}_4\mathrm{F}_{60+16\mathrm{x}}$ (figure 4.15) with that of $(\mathrm{ZnTPPF})_4\mathrm{F}_{60+16\mathrm{x}}$ shows that the saturation point in the first case lies at a desorption laser power density of $4.6\ MW/cm^2$, which is twice as much as for $(\mathrm{ZnTPPF})_4\mathrm{F}_{60+16\mathrm{x}}$. This faster rise suggests that the lighter molecules possess a lower evaporation enthalpy than the heavier molecules [36, 41, 108]. This is consistent by regarding the van der Waals intermolecular-interaction. A comparison of library 1 and library 2 shows that $\mathrm{TPP(TPP)}_4\mathrm{F}_{60+16\mathrm{x}}$ has more than twice as many (factor = 2.3) perfluorooctyl side chains compared to $(\mathrm{ZnTPPF})_4\mathrm{F}_{60+16\mathrm{x}}$, whereas the mass only differs by a factor of 1.9. Thus with respect to the molecular mass, in library 2 the side chains contribute more to the static polarizability than it is the case in library 1. Apart from that, the central unit of each of the libraries can contribute to the overall static polarizability $\alpha_{stat.}$. As the porphyrin in the centre of library 2 doesn′t break the conjugation of the whole core in contrast to library 1, we believe that this may increase the polarizability of $\mathrm{TPP(TPP)}_4\mathrm{F}_{60+16\mathrm{x}}$.

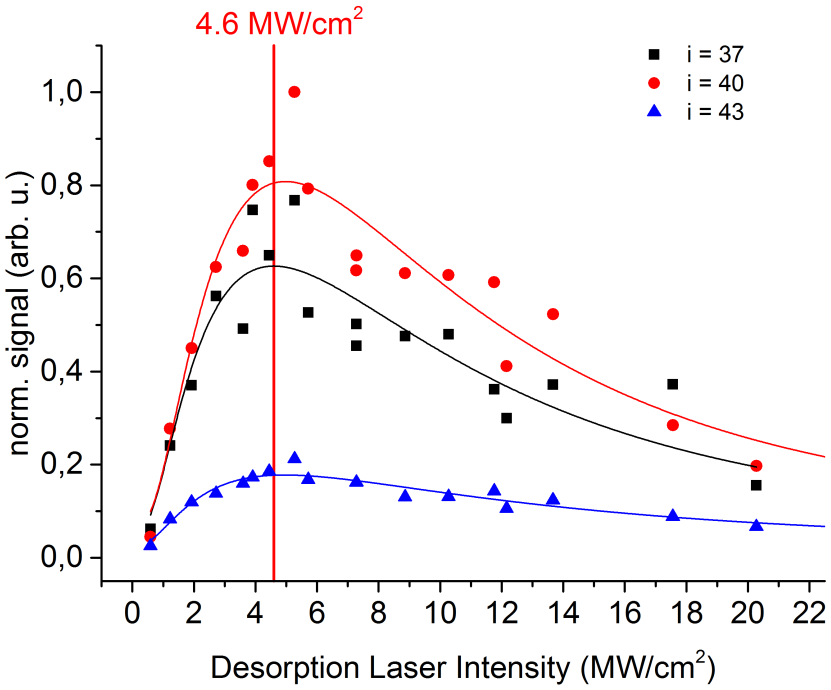

Figure 4.15: $\mathrm{TPP(TPP)_4F_{60+16x}}$ was desorbed through a 355 nm Nd:YAG, whereas its pulse energy is varied. The signal shows an increase up to saturation and then begins to fall, indicating the fragmentation. Solid lines are guides for the eye. For further explanation, see the text.

For the sake of completeness is should be mentioned that the central tetraphenylmethane core of library 1 has a much lower polarizablity than the TPP in library 2. In ref. [115] $\alpha_{stat.}$ of tetraphenylmethane is given as $4\pi\epsilon_0 \cdot 33\ \mathring{A}$, whereas the polarizability of tetraphenylporphyrin is $4\pi\epsilon_0 \cdot 105\ \mathring{A}$ [113], thus more than three times larger. The fragmentation behaviour is different between these two molecular libraries as well. The decay constant for $\mathrm{(ZnTPPF)_4F_{60+16x}}$ is higher than for $\mathrm{TPP(TPP)_4F_{60+16x}}$ by almost a factor of ten. This is consitent with the larger number of vibrational modes in library 2 in comparison to library 1. The same internal energy would correspond to a lower temperature of the moelecule. Recently it has been shown that the relaxation rates of a molecule in the gas phase are strongly coupled to the molecular size [136]. The structural variation between these two libraries can also influence the difference in stability.

4.6 Photoionization efficiencies

As mentioned in section 2.1.5 the molecular sources have to meet some requirements for matter-wave interferometry. In OTIMA, efficient photodepletion (ionization or/and fragmentation) is an essential prerequisite for the proper working of the gratings. Here the interference contrast is influenced by the molecular transmission through a light grating. This is mainly influenced by the ionization cross section of the particle. For a sufficient visibility, a minimal ionization cross section in the order of $10^{-17}\ cm^2$ [7, 78] has been calculated. This is a result for a laser energy of 4 mJ with a beam shape of 10 x 1 mm^2. In the following the photoionization efficiency shall be discussed for both libraries $(\mathrm{ZnTPPF})_4\mathrm{F}_{60+16\mathrm{x}}$ and $\mathrm{TPP}(\mathrm{TPP})_4\mathrm{F}_{60+16\mathrm{x}}$.

4.6.1 VUV photoionization of $(\mathrm{ZnTPPF})_4\mathrm{F}_{60+16\mathrm{x}}$

The photoionization efficiency was measured by variation of the pulse energy of the post ionization laser (157 nm). As described in section 3.2.2, this is controlled through the gas discharge voltage. Focussing the 157 nm through a cylindrical lens (f=+200 mm) the minimum energy which can be reached is about 200 μJ. This is limited by the minimum gas discharge voltage one can set in a fluorine laser. In order to go further down with the laser power, we removed the focussing lens and delimited the laser beam through a slit to guarantee the same laser beam shape as compared to the case with the lens. With this method we can reach energy values down to 10 μJ. It should be noted that the pulse energy measurement was done with a pyro electric energy sensor of Ophir Photonics [18] with a calibration error of 3%. This energy sensor was placed in the beam path and then purged with nitrogen. As the flowing nitrogen gas cools the surface of the power meter, the energy could have a larger error. Losses occurring through the imperfection of window transmittance were already taken into account in the energy measurements. In figure 4.16 we show the efficiency curve for the photoionization of library 1. At lower laser energy the signal rapidly increases until a saturation point is reached. Further increase leads to a drop of the signal. This figure not only demonstrates the successful photoionization of large molecules at 157 nm, but it also shows that $(\mathrm{ZnTPPF})_4\mathrm{F}_{60+16\mathrm{x}}$ is suitable for future matter-wave experiments.

[18] See PE-25C. URL: `http://www.ophiropt.com/laser-measurement-instruments/laser-power-energy-meters/products/energy-sensors/pyroelectric-energy-sensors`

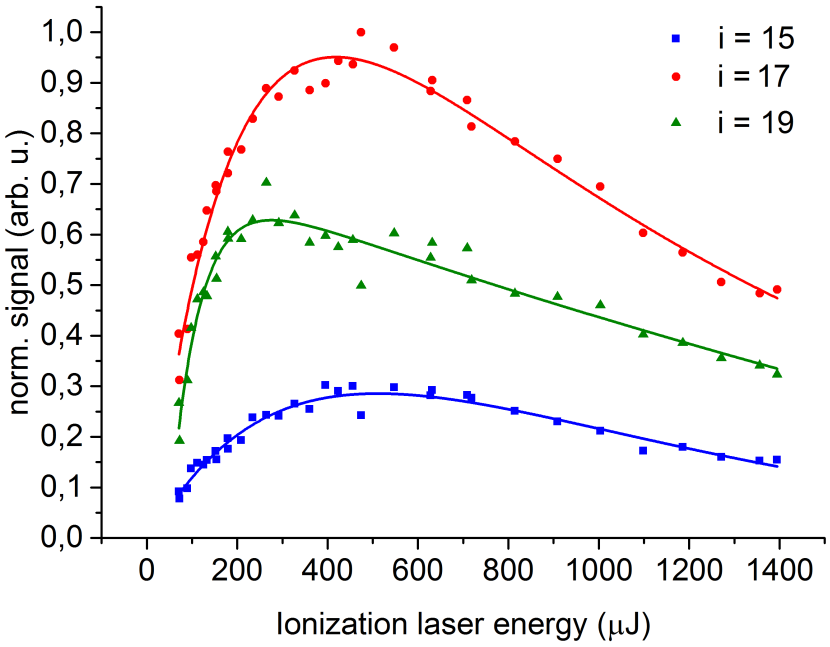

Figure 4.16: Photoionization efficiency of $(\mathrm{ZnTPPF})_4\mathrm{F}_{60+16\mathrm{x}}$. Different symbols represent different number of attached perfluorooctyl side chains ($i = 15, 17$ and 19) and the lines are only present to guide the eye. First the signal intensity increases with growing post-ionization energy, but after reaching saturation, photodissociation of the molecules start.

The fact that saturation is achieved ($\approx 600\ mV$), means that all of the molecules inside the ionization volume get charged. Together with the fact that saturation occurs already at low laser energies suggests that the ionization cross section is sufficiently large for the proposed matter-wave interferometry [32]. But also in the case of KDTLI, the appearance of saturation has a major impact, as the detection of the molecules becomes efficient. In principle, one could extract the photoionization and fragmentation cross sections from figure 4.16. There have been many attempts to find an appropriate fit for the determination of the cross section [65, 137, 138]. To our knowledge this has been achieved only for molecular monomers in literature [137]. However our sample contains a distribution of molecules with different side chains, so new mathematical expressions are needed. This new theory has to take into account that a loss of x chains (due to fragmentation) of a molecule initially containing y chains would fill up the population of molecules with y-x chains. We have set up rate equations describing the number density of organic molecules. Three cases are considered [137]:

1. Ionization of neutral molecules with rate R_I

2. Fragmentation of neutral molecules with rate R_{F_n} and

3. Dissociation of an already ionized molecule with rate R_{F_I}

with N the maximum number of perfluorooctly side chains which can be attached to molecules. In our case $N = 60$. For single photon processes the rate constant would look like $R = \sigma \cdot P/h\nu$, whereas σ is the cross section, P the laser power and $h\nu$ the photon energy. The number density of the neutral molecules with x perfluorooctyl side chains is denoted by $\rho_n^x(t)$. For the ionized species, we use $\rho_I^x(t)$, whereas x denotes the number of attached side chains. The rate equations form a system of coupled inhomogeneous first order differential equations:

$$\dot{\rho}_n^x(t) = -R_I^x \cdot \rho_n^x(t) - R_{F_n}^x \cdot \rho_n^x(t) + \sum_{\xi=x+1}^{N} R_{F_n}^{\xi} \cdot \rho_n^{\xi}(t) \tag{4.3}$$

$$\dot{\rho}_I^x(t) = +R_I^x \cdot \rho_n^x(t) - R_{F_I}^x \cdot \rho_I^x(t) + \sum_{\eta=x+1}^{N} R_{F_I}^{\eta} \cdot \rho_I^{\eta}(t) + \sum_{\gamma=x+1}^{N} R_I^{\gamma} \cdot (R_{F_n}^{\gamma} \cdot \rho_n^{\gamma}(t)) \tag{4.4}$$

The first term in equation 4.3 describes the increase of the neutrals through photoionization. The second term contains the fragmentation losses but the last expression results in an increase of the neutrals through the fragmentation of molecules with higher numbers of fluorinated side chains. Equation 4.4 represents the number density of molecular ions, which are increased by the photoionization of the neutral molecules (first term), the fragmentation of charged heavier molecules (third term) and finally through the photoionization of the neutral molecules with larger chain numbers (last expression). A loss factor (second term) including the fragmentation of the ionized molecules is also taken into account. Every differential equation needs initial conditions. In our case all of the $\rho_I^x(0) = 0$, but the $\rho_n^x(0)$ will have different values as the molecular libraries does have a mass distribution. It is clear that most abundant molecules in the synthesis will also lead to the highest signal intensities. Therefore, the initial condition for each of the population must obey this mass distribution. In our algorithm (written in Mathematica), we ensured this by taking the mass spectrum of $(\mathrm{ZnTPPF})_4\mathrm{F}_{60+16\mathrm{x}}$ at a given ionization energy and extracting the peak values. This step is shown in figure 4.17a.

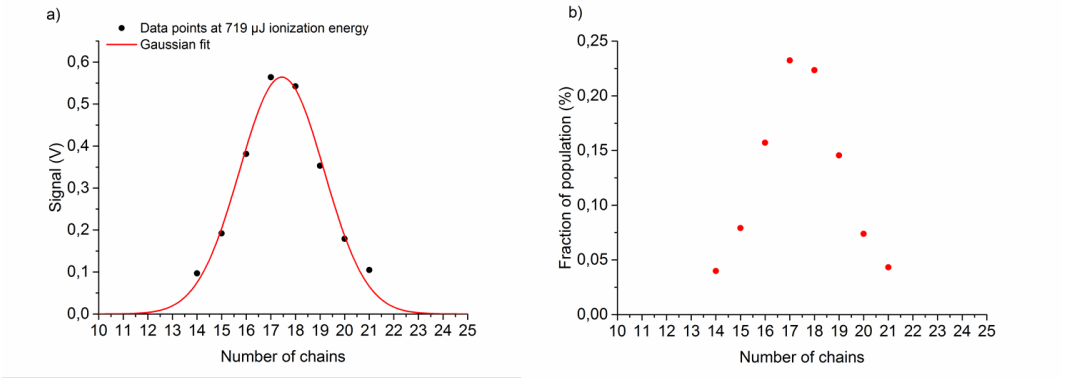

Figure 4.17: Panel a) shows the signal intensity in Volts. They are extracted from the mass spectrum at a post-ionization energy of 710 μJ. To these peak values, a Gaussian function (see 4.1) was fitted. From this normalized fit, the fraction of population was then extracted. This is the content of panel b).

From the normalized Gaussian fit, the fraction of population (figure 4.17b) can be calculated. These values were then used for the initial conditions of $\rho_n^x(0)$. With increasing number of side chains, also the number of free parameters (rate constants) grows. To minimize this number we established two models for the ionization and fragmentation cross sections. These are:

- If we assume a linear dependence of the ionization cross section on the number of chains, only two parameters must be defined. These are the intercept and the slope of equation 4.5.

$$R_I^x = R_I^0 + x \cdot \Delta R_I \tag{4.5}$$

  This assumption is based on the believe that the addition of a single perfluorooctyl chain will not only increase the geometrical size of the molecule, but it acts also as an extra electron-pool for photoionization. As already discussed in 4.1, the side chains can be imagined as a positive carbon backbone with a surrounding negative shell of fluorine atoms, where the electrons can be detached by a photon.

- Our second model deals with the fragmentation behaviour of the molecule. As it was shown previously, the molecular relaxation rates are strongly influenced by the size of the molecules [136]. We believe that the addition of a side chain will open more relaxation paths. Although little is known how the number of relaxation channels increases with increasing size of the molecule, here we assumed an exponential dependence according to the Boltzmann distribution.

Another assumption we have made is, that fragmentation is independent of the number of charges in the molecule, thus $R^x_{F_I} = R^x_{F_n}$ [137]. Together with the last assumption, the parameter amount of fragmentation rate constants can be drastically reduced to three parameters (A, B, α) as we used equation 4.6.

$$R^x_{I,F} = A \cdot exp(-\alpha \cdot x) + B \tag{4.6}$$

For a test run, we implemented a simplified set of differential equations together with these assumptions in Mathematica. The simplification comprises the fact that we considered the fragmentation of only one single side chain. The preliminary results are promising, however the full model should be calculated for precise statements.

A proof of fragmentation of $(\mathrm{ZnTPPF})_4\mathrm{F}_{60+16\mathrm{x}}$

In figure 4.3 the signal intensity of the peak corresponding to the mass of a single chain (X_1 peak in figure 4.5) is plotted against the post-ionization energy measured by the energy sensor (Ophir). Figure 4.18 shows a linear increase of the signal, whereas the slope smoothly increases. Our attempt was to divide figure 4.18 into two parts which we fitted with a linear function to compare the slopes. Up to ionization energies of $\approx 550\ \mu J$ the intensity is well represented by a linear function, with a slope of (600 ± 90) arb.u. The blue dashed line represent the second part of the data and possesses a much higher rise (slope is (920 ± 90) arb.u.). This change in the slope could be argued with a possible photofragmentation of the libraries at higher ionization laser energies (see figure 4.16).

4.6.2 VUV photoionization of $\mathrm{TPP(TPP)}_4\mathrm{F}_{60+16\mathrm{x}}$

The ionization efficiency curve of library 2 is shown in figure 4.19. As observed for $(\mathrm{ZnTPPF})_4\mathrm{F}_{60+16\mathrm{x}}$, library 2 also increases up to a certain value of the post-ionization energy. However, a detailed comparison shows that the rise for $\mathrm{TPP(TPP)}_4\mathrm{F}_{60+16\mathrm{x}}$ is faster than for library 1, as saturation is reached earlier. The saturation signal is roughly $100\ mV$, so six times less than for $(\mathrm{ZnTPPF})_4\mathrm{F}_{60+16\mathrm{x}}$. This suggests a bigger ionization cross section. Two factors may contribute to that:

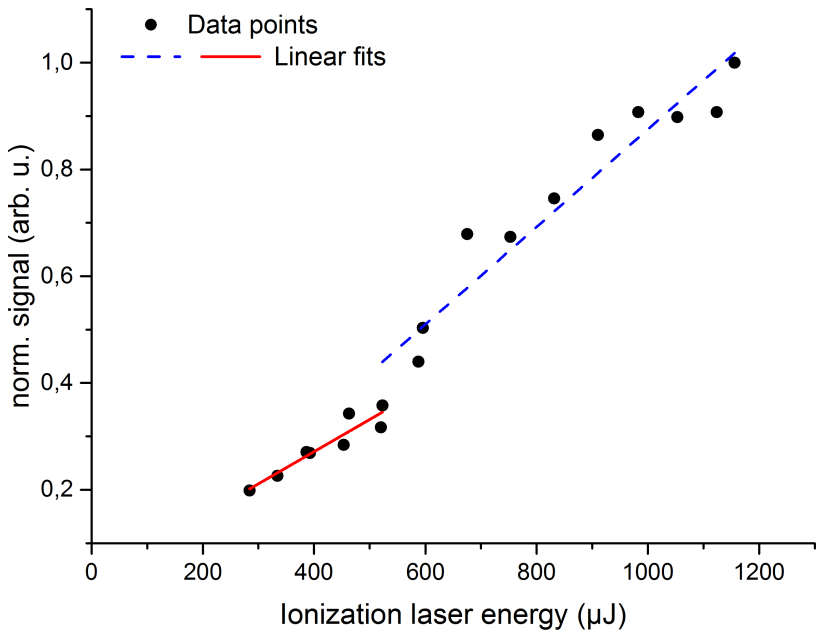

Figure 4.18: Post-ionization energy was varied and simultaneously the signal intensity of a single perfluoroalkyl chain was recorded. Interestingly one can observe two separated parts in the data set. At low F_2 energies the signal is well described through the red solid line, but suddenly the rise becomes stronger (dashed blue line). This is an indication for the fragmentation at higher laser energies.

- First, library 2 has more than twice as much as perfluorooctyl side chains compared to library 1. As mentioned earlier, the side chains not only increase the geometrical size and therefore the geometrical absorption cross section of the molecule but they also increase the electron cloud surrounding the particle.

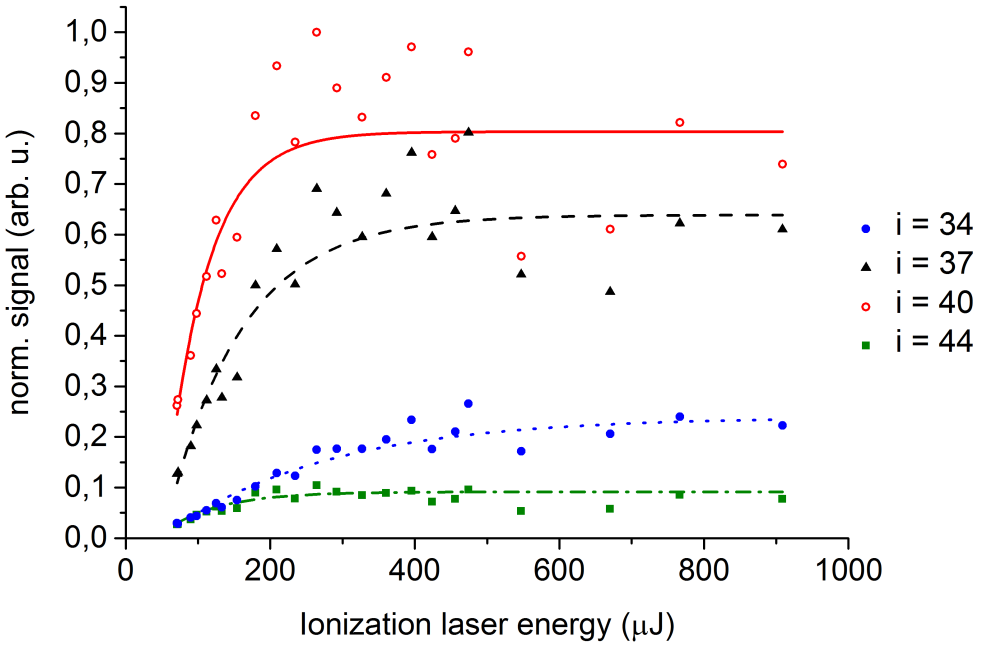

Figure 4.19: Distinct symbols represent different numbers of perfluorooctyl side chains attached to $\mathrm{TPP(TPP)_4F_{60+16x}}$. In contrast to $\mathrm{(ZnTPPF)_4F_{60+16x}}$ (figure 4.17), saturation is reached at earlier ionization energies and no fragmentation is observed.

- Comparing the structures of the molecules (see figure 4.1 and figure 4.2) the central unit earns attention. For the heavier library 2 a TPP molecule builds the central unit, whereas for library 1 it is tetraphenylmethane (TPM). As it is known that TPP photoionizes efficiently, we believe that it contributes much more to the ionization cross section than TPM.

Apart of that also the fragmentation behaviour is different. While photodissociation is present for $\mathrm{(ZnTPPF)_4F_{60+16x}}$, library 2 remains constant up to the maximum fluorine laser energy. The question is why the members of library 1 fragment while $\mathrm{TPP(TPP)_4F_{60+16x}}$ doesn′t? A clear answer to this question can′t be given as no experimental investigation has been done on that problem. We suspect that library 2 has a larger number of relaxation channels than library 1, as there are more side chains attached [136]. The deposited energy through the photons can then be distributed much easier over many vibrational and rotational levels [139]. This is simplified through the central TPP molecule, as it forms a fully conjugated molecular system, whereas the conjugation is broken for $\mathrm{(ZnTPPF)_4F_{60+16x}}$ through the TPM unit.

It has been shown in a variety of publications that electronic energy can flow over $\pi-$conjugated systems [140, 141]. This feature is essential in molecular electronics [142–145].

4.6.3 Experimental improvements

Although figure 4.16 and figure 4.19 show a clear behaviour of the ionization efficiency, there is still room for improvement. Especially the determination of the cross sections and whether the ionization is a single or multiple photon process needs an advanced experiment. For future measurements on the photoionization efficiency, we will implement the following experimental improvements:

1. As the energy of the fluorine laser is influenced by the purged nitrogen gas, we will design and build a beam guiding system. This will contain a gas regulation valve and it will be attached to a pre vacuum pump. With these elements we hope not only to control the fluctuations of the nitrogen concentration but we will be able to reduce the post-ionization energy down to zero in a controlled way. This may answer the question whether the photoionization is a single or multiple photon process.

2. We want to install a small photodiode inside the desorption chamber. This will measure the fluorine laser energy continuously. On the one hand we can record the energy simultaneous to the desorption and on the other hand the measurement gets more precise.

Chapter 5

Conclusion

> *A conclusion is the place where you got tired of thinking.*
>
> A. Bloch, *1882-1942*

A short summary of the results should be given at this place.

- We have realized an advanced set up for testing molecular sources. Through the fast exchange of the samples and the advanced analysis program, a variety of molecules can be tested and optimized in a short time.
- First of all, chemists around Prof. Marcel Mayor have shown that the synthesis of perfluoroalkylated libraries up to 25000 Da is feasible in large quantities.
- We have shown that these molecules can be volatilized as intact particles through nanosecond, matrix-free laser desorption. We were able to demonstrate their high thermal stability by investigating the behaviour of the molecular signal upon variation of the desorption laser power (see figure 4.14 and figure 4.15).
- I could prove that these libraries of molecules can be ionized at 157nm, which is a prerequisite for the successful implementation into matter-wave interferometry. Currently $TPP(TPP)_4F_{60+16x}$ is the most complex and most massive organic molecule that we have seen to photoionize.

We also observe that the signal for both molecular libraries can be saturated. This is a strong indication for an ionization cross section, which is high enough for high contrast matter wave interference [7, 78, 146]. The library $(\mathrm{ZnTPPF})_4\mathrm{F}_{60+16\mathrm{x}}$ starts to fragment at higher pulse energies of the ionization laser. This could also be used for photodepletion gratings which have recently been demonstrated [147].

- By varying the time delay between the desorption laser and the post-ionization laser, we were able to record the velocity distribution of the molecular cloud. It turned out that the neutrals of $(\mathrm{ZnTPPF})_4\mathrm{F}_{60+16\mathrm{x}}$ have a most probable velocity of 90 m/s and $\mathrm{TPP}(\mathrm{TPP})_4\mathrm{F}_{60+16\mathrm{x}}$ reach velocities as low as 40 m/s. Even at 25.000 Da this is still compatible with existing interferometers in Vienna.
  The chemical approach is expected to be scalable by at least another factor of two in mass. And since we find also substantial signal at 20 m/s for 25 kDa it is likely that the techniques established here will be upgradable to matter wave interferometry at 50.000 amu with molecules composed of several thousand atoms in the near future.

Although most of the molecular beam properties seem to meet the requirements for matter wave experiments already now, the signal intensities still need to be enhanced. First the molecular source has to be placed several tens of centimetres away from the detector in the current implementation of the interferometer. The beam density decreases proportional to $1/r^2$ (r is the distance from the source to the detector). Second, a collimation of 1 mrad of the beam has to be realized, so that the molecules fly in the vicinity of the interferometer mirror.

Chapter 6

Outlook

> *Erfolg hat drei Buchstaben: TUN!*
>
> J. W. Goethe, *1749 - 1832*

The main aim is to push the mass limit in current interferometers. In the scope of this thesis two molecular libraries have been presented to do this. However, we believe that the nonlinearity of quantum mechanics will occur at higher masses - higher than the masses presented in this work. Our colleagues in Basel are already working on polyporphyrin macromolecules with branched perfluoroalkyl side chains to reach 50000 Da. These molecular libraries will be tested in our setup. However, synthesis of polyporphyrins to reach 10^5 Da may be difficult, as several hundreds of mg is needed to perform a matter-wave interference experiment. For that reason we pursuit another strategy. Chemists around Prof. Mayor will synthesize nanoparticles which can be easily tuned in size and mass. These nanoparticles will carry fluorinated side chains, too. Figure 6.1 shows an example of such a nanoparticle. The attached fluorine chains should simplify the evaporation/desorption and increase the thermal stability, whereas the central core should be photoionisable. This is for example true for many metal and semiconductor nanoparticles [148]. In figure 6.1 we use silicon, as it is known from the literature that clusters of thereof have an ionization potential below 6 eV [149]. Indeed, this is not necessary at all. One could also use fluorinated chromophores which can be attached to the nanoparticles.

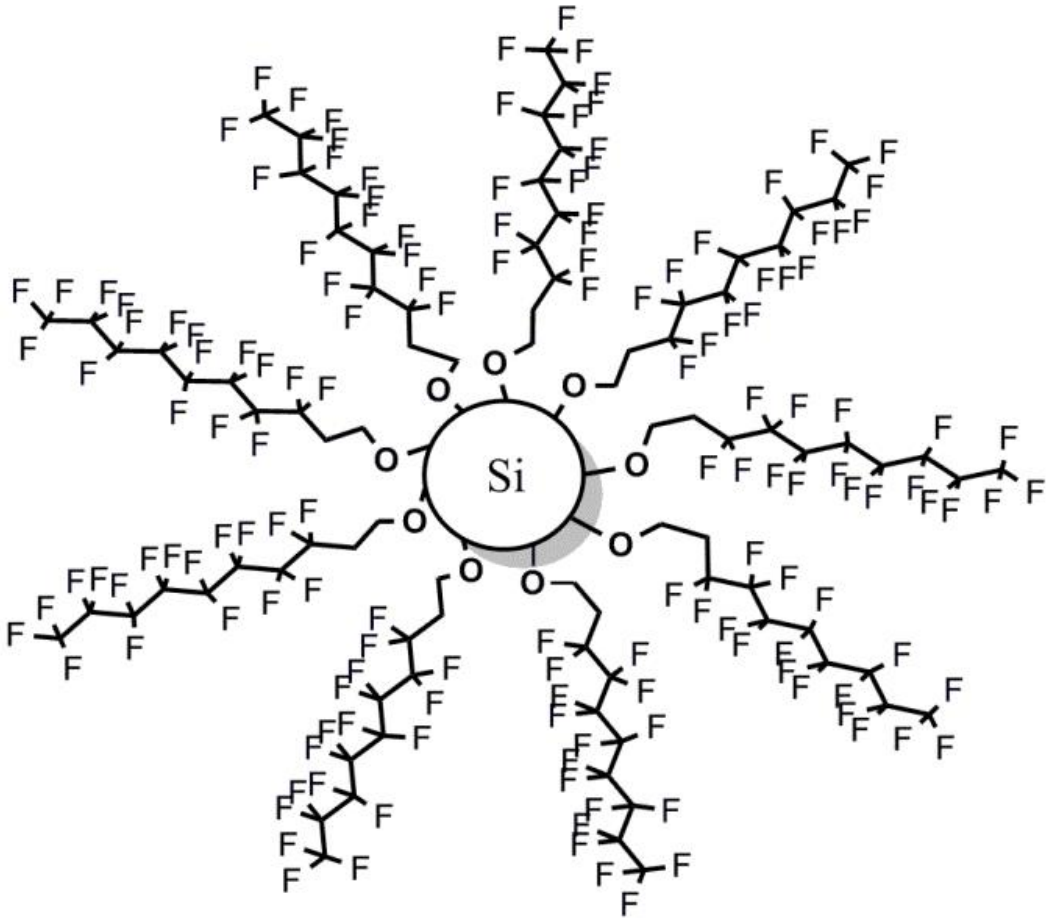

Figure 6.1: The new class of particles for matter wave interferometry. Here a silicon nanoparticle serves as the chromophore for photo ionization while the perfluoroalkyl chains increase the volatility.

Apart of that our aim is also to develop nanoparticles with high fluorescence quantum yields to explore optical detection schemes for high masses in matter-wave interferometers [64]. However, here the difficulty is to detect the signal from only those nanoparticles which have not been destroyed after desorption or during the flight. This is a difficult task which requires substantial effort.

The big aim should still be the interference of masses reaching 10^5 Da. The molecular libraries presented in the scope of this work are an essential step towards this goal. For matter-wave interference experiments with the aforementioned nanoparticles many characterization studies have to be done in order to judge whether the nanospheres are suitable for the interferometers.

List of Figures

List of Tables

Bibliography

[1] A. Einstein. Über einen die Erzeugung und Verwandlung des Lichtes betreffenden heuristischen Gesichtspunkt. *Annalen der Physik*, 322(6):132–148, 1905.

[2] L. De Broglie. Waves and quanta. *Nature*, 112(2815):540–540, 1923.

[3] C. Davisson and L. H. Germer. The scattering of electrons by a single crystal of nickel. *Nature*, 119(2998):558–560, 1927.

[4] S. Eibenberger, S. Gerlich, M. Arndt, M. Mayor, and J. Tüxen. Matter wave interference of particles selected from a molecular library with masses exceeding 10000 amu. *Physical Chemistry Chemical Physics*, 15(35):14696–14700, 2013.

[5] L. Felix, U. Sezer, M. Arndt, and M. Mayor. Synthesis of highly fluoroalkyl-functionalized oligo-porphyrin systems. 2014.

[6] U. Sezer, P. Schmid, L. Felix, M. Mayor, and M. Arndt. Slow beams and VUV postionization of macromolecular libraries. 2014.

[7] P. Haslinger, N. Dörre, P. Geyer, J. Rodewald, S. Nimmrichter, and M. Arndt. A universal matter-wave interferometer with optical ionization gratings in the time domain. *Nature Physics*, 9(3):144–148, 2013.

[8] S. Gerlich, S. Eibenberger, M. Tomandl, S. Nimmrichter, K. Hornberger, P. J. Fagan, J. Tüxen, M. Mayor, and M. Arndt. Quantum interference of large organic molecules. *Nature Communications*, 2:263, 2011.

[9] K. Hornberger, J. E. Sipe, and M. Arndt. Theory of decoherence in a matter wave talbot-lau interferometer. *Physical Review A*, 70(5):053608, 2004.

[10] M. Arndt and K. Hornberger. Testing the limits of quantum mechanical superpositions. *Nature Physics*, 10(4):271–277, 2014.

[11] J. R. Friedman, V. Patel, W. Chen, S. K. Tolpygo, and J. E. Lukens. Quantum superposition of distinct macroscopic states. *Nature*, 406(6791):43–46, 2000. 10.1038/35017505.

[12] M. Zawisky, M. Baron, R. Loidl, and H. Rauch. Testing the world's largest monolithic perfect crystal neutron interferometer. *Nuclear Instruments and Methods in Physics Research Section A: Accelerators, Spectrometers, Detectors and Associated Equipment*, 481(13):406 – 413, 2002.

[13] S. M. Dickerson, J. M. Hogan, A. Sugarbaker, D. M. S. Johnson, and M. A. Kasevich. Multiaxis inertial sensing with long-time point source atom interferometry. *Physical Review Letters*, 111:083001, 2013.

[14] S. W. Chiow, T. Kovachy, H.-C. Chien, and M. A.Kasevich. Large area atom interferometers. *Physical Review Letters*, 107:130403, 2011.

[15] S. Nimmrichter and K. Hornberger. Macroscopicity of mechanical quantum superposition states. *Physical Review Letters*, 110(16):160403, 2013.

[16] P. Asenbaum, S. Kuhn, S. Nimmrichter, U. Sezer, and M. Arndt. Cavity cooling of free silicon nanoparticles in high vacuum. *Nature Communications*, 4, 2013.

[17] W. Demtröder. *Experimentalphysik*, volume 3. Springer-Verlag Berlin Heidelberg New York, Germany, 2005.

[18] H. Rauch, W. Treimer, and U. Bonse. Test of a single crystal neutron interferometer. *Physics Letters A*, 47(5):369 – 371, 1974.

[19] A. D. Cronin, J. Schmiedmayer, and D. E. Pritchard. Optics and interferometry with atoms and molecules. *Reviews of Modern Physics*, 81:1051–1129, 2009.

[20] Ch. J. Bordé, S. Avrillier, A. Van Lerberghe, Ch. Salomon, D. Bassi, and G. Scoles. Observation of optical ramsey fringes in the 10 μm spectral region using a supersonic beam of SF6. *Le Journal de Physique Colloques*, 42(C8):C8–15, 1981.

[21] O. Carnal and J. Mlynek. Young's double-slit experiment with atoms: A simple atom interferometer. *Physical Review Letters*, 66:2689–2692, 1991.

[22] M. Arndt, O. Nairz, J. V.-Andreae, C. Keller, G. Van der Zouw, and A. Zeilinger. Waveparticle duality of C60 molecules. *Nature*, 401(6754):680–682, 1999.

[23] J. F. Clauser and S. Li. Talbot-Lau atom interferometry with cold slow potassium. *Physical Review A*, 49(4):R2213, 1994.

[24] A. Steane, P. Szriftgiser, P. Desbiolles, and J. Dalibard. Phase modulation of atomic de broglie waves. *Physical Review Letters*, 74(25):4972, 1995.

[25] B. Brezger, L. Hackermller, S. Uttenthaler, J. Petschinka, M. Arndt, and A. Zeilinger. Matter-wave interferometer for large molecules. *Physical Review Letters*, 88(10):100404, 2002.

[26] L. Hackermüller, S. Uttenthaler, K. Hornberger, E. Reiger, B. Brezger, A. Zeilinger, and M. Arndt. Wave nature of biomolecules and fluorofullerenes. *Physical Review Letters*, 91(9):090408, 2003.

[27] S. Gerlich, L. Hackermüller, K. Hornberger, A. Stibor, H. Ulbricht, M. Gring, F. Goldfarb, T. Savas, M. Müri, and M. Mayor. A KapitzaDiracTalbotLau interferometer for highly polarizable molecules. *Nature Physics*, 3(10):711–715, 2007.

[28] K. Hornberger, S. Gerlich, P. Haslinger, S. Nimmrichter, and M. Arndt. Colloquium: Quantum interference of clusters and molecules. *Reviews of Modern Physics*, 84(1):157, 2012.

[29] H. F. Talbot. I. Facts relating to optical science.No. III. *The London and Edinburgh Philosophical Magazine and Journal of Science*, 9(51):1–4, 1836.

[30] W. B. Case, M. Tomandl, S. Deachapunya, and M. Arndt. Realization of optical carpets in the Talbot and Talbot-Lau configurations. *Optical Express*, 17(23):20966–20974, 2009.

[31] Ernst Lau. Beugungserscheinungen an Doppelrastern. *Annalen der Physik*, 437(78):417–423, 1948.

[32] P. Haslinger. *A universal matter-wave interferometer with optical gratings*. Thesis, 2013.

[33] M. Arndt, L. Hackermüller, and E. Reiger. Interferometry with large molecules: exploration of coherence, decoherence and novel beam methods. *Brazilian Journal of Physics*, 35(2A):216–223, 2005.

[34] S. Eibenberger, X. Cheng, J. P. Cotter, and M. Arndt. Absolute absorption cross sections from photon recoil in a matter-wave interferometer. *Physical Review Letters*, 112:250402, 2014.

[35] S. Nimmrichter, K. Hornberger, P. Haslinger, and M. Arndt. Testing spontaneous localization theories with matter-wave interferometry. *Physical Review A*, 83(4):043621, 2011.

[36] K. Dreisewerd. The desorption process in MALDI. *Chemical Reviews*, 103(2):395–426, 2003.

[37] A. V. Zinovev, I. V. Veryovkin, J. F. Moore, and M. J. Pellin. Laser-driven acoustic desorption of organic molecules from back-irradiated solid foils. *Analytical Chemistry*, 79(21):8232–8241, 2007.

[38] J. Rudolf Horak. *Design and characterisation of a LIAD source in view of the matter wave interferometry*. Thesis, 2013.

[39] R. E. Johnson. Models for matrix-assisted desorption by a laser-pulse. *International Journal of Mass Spectrometry and Ion Processes*, 139:25–38, 1994.

[40] L. V. Zhigilei and B. J. Garrison. Microscopic mechanisms of laser ablation of organic solids in the thermal and stress confinement irradiation regimes. *Journal of Applied Physics*, 88(3):1281–1298, 2000.

[41] K. Dreisewerd, M. Schürenberg, M.l Karas, and F. Hillenkamp. Influence of the laser intensity and spot size on the desorption of molecules and ions in matrix-assisted laser desorption/ionization with a uniform beam profile. *International Journal of Mass Spectrometry and Ion Processes*, 141(2):127–148, 1995.

[42] L. V. Zhigilei, P. B. S. Kodali, and B. J. Garrison. Molecular dynamics model for laser ablation and desorption of organic solids. *The Journal of Physical Chemistry B*, 101(11):2028–2037, 1997.

[43] L. V. Zhigilei, P. B. S. Kodali, and B. J. Garrison. On the threshold behavior in laser ablation of organic solids. *Chemical Physics Letters*, 276(34):269–273, 1997.

[44] N. Gotsche, H. Ulbricht, and M. Arndt. UV-VIS absorption spectroscopy of large molecules for applications in matter wave interferometry. *Laser Physics*, 17(4):583–589, 2007.

[45] F. Hillenkamp and J. P.-Katalinic. *MALDI MS*. Wiley-VCH Verlag, Weinheim, 2007.

[46] M. Haisa, S. Kashino, S.-I. Hanada, K. Tanaka, S. Okazaki, and M. Shibagaki. The structures of 2-hydroxy-5-methylbenzoic acid and dimorphs of 2, 5-dihydroxybenzoic acid. *Acta Crystallographica Section B: Structural Crystallography and Crystal Chemistry*, 38(5):1480–1485, 1982.

[47] W. Zhang, S. Niu, and B. T. Chait. Exploring infrared wavelength matrix-assisted laser desorption/ionization of proteins with delayed-extraction time-of-flight mass spectrometry. *Journal of the American Society for Mass Spectrometry*, 9(9):879–884, 1998.

[48] S. Berkenkamp, F. Kirpekar, and F. Hillenkamp. Infrared maldi mass spectrometry of large nucleic acids. *Science*, 281(5374):260–262, 1998.

[49] A. Leisner, A. Rohlfing, S. Berkenkamp, F. Hillenkamp, and K. Dreisewerd. Infrared laser post-ionization of large biomolecules from an IR-MALD(I) plume. *Journal of the American Society for Mass Spectrometry*, 15(6):934–941, 2004.

[50] A. Vertes, R. Gijbels, and R. D. Levine. Homogeneous bottleneck model of matrix-assisted ultraviolet laser desorption of large molecules. *Rapid Communications in Mass Spectrometry*, 4(6):228–233, 1990.

[51] R. S. Brown and J. J. Lennon. Sequence-specific fragmentation of matrix-assisted laser-desorbed protein/peptide ions. *Analytical Chemistry*, 67(21):3990–3999, 1995.

[52] B. Spengler. Post-source decay analysis in matrix-assisted laser desorption/ionization mass spectrometry of biomolecules. *Journal of Mass Spectrometry*, 32(10):1019–1036, 1997.

[53] A. Vertes, G. Luo, L. Ye, Y. Chen, and I. Marginean. Laser pulse length dependence of internal energy transfer in UV-MALDI-MS. *Applied Physics A*, 79(4-6):823–825, 2004.

[54] Y. Chen and A. Vertes. Pumping rate and surface morphology dependence of ionization processes in matrix-assisted laser desorption ionization. *The Journal of Physical Chemistry A*, 107(46):9754–9761, 2003.

[55] J. Wichmann. *Matrix-gestützte Laser-Desorption und Ionization (MALDI) mit ultrkurzen Laserpulsen*. Phd thesis, 2010.

[56] Y.J. Bae, J. H. Moon, and M. S. Kim. Expansion cooling in the matrix plume is under-recognized in MALDI mass spectrometry. *Journal of the American Society for Mass Spectrometry*, 22(6):1070–1078, 2011.

[57] A. A. Puretzky and D. B. Geohegan. Gas-phase diagnostics and LIF-imaging of 3-hydroxypicolinic acid MALDI-matrix plumes. *Chemical Physics Letters*, 286(5):425–432, 1998.

[58] A. A. Puretzky, D. B. Geohegan, G. B. Hurst, M. V. Buchanan, and B. S. Luk'yanchuk. Imaging of vapor plumes produced by matrix assisted laser desorption: A plume sharpening effect. *Physical Review Letters*, 83(2):444–447, 1999.

[59] R. E. Johnson and Y. LeBeyec. Angular distribution of the ejecta in matrix-assisted laser desorption/ionization: Model dependence. *International Journal of Mass Spectrometry*, 177(2):111–118, 1998.

[60] F. Aksouh, P. Chaurand, C. Deprun, S. Della-Negra, Y. Le Beyec, J. Hoyes, and R. R. Pinho. Influence of the laser beam direction on the molecular ion ejection angle in matrix-assisted laser desorption/ionization. *Rapid Communications in Mass Spectrometry*, 9(6):515–518, 1995.

[61] D. S. George, A. Onischenko, and A. S. Holmes. On the angular dependence of focused laser ablation by nanosecond pulses in solgel and polymer materials. *Applied Physics Letters*, 84(10):1680–1682, 2004.

[62] T. Juffmann, S. Truppe, P. Geyer, A. G. Major, S. Deachapunya, H. Ulbricht, and M. Arndt. Wave and particle in molecular interference lithography. *Physical Review Letters*, 103(26):263601, 2009.

[63] T. Juffmann, A. Milic, M.l Mllneritsch, P. Asenbaum, A. Tsukernik, J. Txen, M.l Mayor, O. Cheshnovsky, and M. Arndt. Real-time single-molecule imaging of quantum interference. *Nature Nanotechnology*, 7(5):297–300, 2012.

[64] A. Stibor, A. Stefanov, F. Goldfarb, E. Reiger, and M. Arndt. A scalable optical detection scheme for matter wave interferometry. *New Journal of Physics*, 7(1):224, 2005.

[65] M. Marksteiner, A. Divochiy, M. Sclafani, P. Haslinger, H. Ulbricht, A. Korneev, A. Semenov, G. Goltsman, and M. Arndt. A superconducting nbn detector for neutral nanoparticles. *Nanotechnology*, 20(45):455501, 2009.

[66] P. Tinnefeld. Single-molecule detection: Breaking the concentration barrier. *Nature Nanotechnology*, 8(7):480–482, 2013.

[67] J. Park, D. Bang, K. Jang, E. Kim, S. Haam, and S. Na. Multimodal label-free detection and discrimination for small molecules using a nanoporous resonator. *Nature Communications*, 5, 2014.

[68] A. M. Armani, R. P. Kulkarni, S. E. Fraser, R. C. Flagan, and K. J. Vahala. Label-free, single-molecule detection with optical microcavities. *Science*, 317(5839):783–787, 2007.

[69] J. Zhu, S. K. Ozdemir, Y.-F. Xiao, L. Li, L. He, D.-R. Chen, and L. Yang. On-chip single nanoparticle detection and sizing by mode splitting in an ultrahigh-Q microresonator. *Nature Photonics*, 4(1):46–49, 2010.

[70] A. K. Naik, M. S. Hanay, W. K. Hiebert, X. L. Feng, and M. L. Roukes. Towards single-molecule nanomechanical mass spectrometry. *Nature Nanotechnology*, 4(7):445–450, 2009.

[71] L. He, S. K. Ozdemir, J. Zhu, W. Kim, and L. Yang. Detecting single viruses and nanoparticles using whispering gallery microlasers. *Nature Nanotechnology*, 6(7):428–432, 2011.

[72] J. H. Gross. *Massenspektrometrie*. Ein Lehrbuch. Springer Berlin Heidelberg, 2013.

[73] J.T. Watson and O.D. Sparkman. *Introduction to Mass Spectrometry*. John Wiley and Sons, 4th edition, 2007.

[74] I. S. Gilmore and M. P. Seah. Ion detection efficiency in SIMs: Dependencies on energy, mass and composition for microchannel plates used in mass spectrometry. *International Journal of Mass Spectrometry*, 202(1):217–229, 2000.

[75] G. Scoles, D. Bassi, U. Buck, and D. Laine. *Atomic and Molecular Beam Methods*. Oxford University Press, 1988.

[76] A. R Dow, A. M. Wittrig, and H. I. Kenttmaa. Laser-induced acoustic desorption (LIAD) mass spectrometry. *European Journal of Mass Spectrometry*, 18(2):77–92, 2012.

[77] V. V. Golovlev, S. L. Allman, W. R. Garrett, N. I. Taranenko, and C. H. Chen. Laser-induced acoustic desorption. *International Journal of Mass Spectrometry and Ion Processes*, 169:69–78, 1997.

[78] P. Schmid, F. Sthr, M. Arndt, J. Txen, and M. Mayor. Single-photon ionization of organic molecules beyond 10 kDa. *Journal of the American Society for Mass Spectrometry*, 24(4):602–608, 2013.

[79] A. Ingendoh, M. Karas, F. Hillenkamp, and U. Giessmann. Factors affecting the resolution in matrix-assisted laser desorptionionization mass spectrometry. *International Journal of Mass Spectrometry and Ion Processes*, 131:345–354, 1994.

[80] K. Dreisewerd, M. Schürenberg, M. Karas, and F. Hillenkamp. Matrix-assisted laser desorption/ionization with nitrogen lasers of different pulse widths. *International Journal of Mass Spectrometry and Ion Processes*, 154(3):171–178, 1996.

[81] M. Csele. *Fundamentals of light sources and lasers*. John Wiley and Sons, New York, 2004.

[82] O. Svelto and D. C. Hanna. *Principles of lasers*. Springer, New York, 2 edition, 1982.

[83] D. Basting and G. Marowsky. *Excimer laser technology*. Springer, 2005.

[84] A. K. Bates, M. Rothschild, T. M. Bloomstein, T. H. Fedynyshyn, R. R. Kunz, V. Liberman, and M. Switkes. Review of technology for 157-nm lithography. *IBM Journal of Research and Development*, 45(5):605–614, 2001.

[85] J. Rodewald. *Setup of an optical time-domain matter wave interferometer for heavy particles*. Thesis, 2011.

[86] M. Kakehata, T. Uematsu, F. Kannari, and M. Obara. Efficiency characterization of vacuum ultraviolet molecular fluorine (F2) laser (157 nm) excited by an intense electric discharge. *IEEE Journal of Quantum Electronics*, 27(11):2456–2464, 1991.

[87] S. M. Hooker and C. E. Webb. Progress in vacuum ultraviolet lasers. *Progress in Quantum Electronics*, 18(3):227–274, 1994.

[88] R. S. Quimby. *Photonics and Lasers: An Introduction*. Wiley, Newark, NJ, 2006.

[89] S. D. Hanton, P. A. C. Clark, and K. G Owens. Investigations of matrix-assisted laser desorption/ionization sample preparation by time-of-flight secondary ion mass spectrometry. *Journal of the American Society for Mass Spectrometry*, 10(2):104–111, 1999.

[90] H.-R. Aerni, D. S. Cornett, and R. M. Caprioli. Automated acoustic matrix deposition for MALDI sample preparation. *Analytical Chemistry*, 78(3):827–834, 2005.

[91] Y. Dai, R. M. Whittal, and L. Li. Two-layer sample preparation:A method for MALDI-MS analysis of complex peptide and protein mixtures. *Analytical Chemistry*, 71(5):1087–1091, 1999.

[92] P. Önnerfjord, J. Nilsson, L. Wallman, T. Laurell, and G. Marko-Varga. Picoliter sample preparation in MALDI-TOF MS using a micromachined silicon flow-through dispenser. *Analytical Chemistry*, 70(22):4755–4760, 1998.

[93] J. Axelsson, A.-M. Hoberg, C. Waterson, P. Myatt, G. L. Shield, J. Varney, D. M. Haddleton, and P. J. Derrick. Improved reproducibility and increased signal intensity in matrix-assisted laser desorption/ionization as a result of electrospray sample preparation. *Rapid Communications in Mass Spectrometry*, 11(2):209–213, 1997.

[94] B. Bhushan. *Springer Handbook of Nanotechnology*. Springer Science+Business Media, 2nd edition, 2007.

[95] S. Y. T. van de Meerakker, H. L. Bethlem, N. Vanhaecke, and G. Meijer. Manipulation and control of molecular beams. *Chemical Reviews*, 112(9):4828–4878, 2012.

[96] S. Y. T. van de Meerakker, H. L. Bethlem, and G. Meijer. Taming molecular beams. *Nature Physics*, 4(8):595–602, 2008.

[97] R. Fulton, A. I. Bishop, and P. F. Barker. Optical stark decelerator for molecules. *Physical Review Letters*, 93(24):243004, 2004.

[98] S. Deachapunya, P. J. Fagan, A. G. Major, E. Reiger, H. Ritsch, A. Stefanov, H. Ulbricht, and M. Arndt. Slow beams of massive molecules. *The European Physical Journal D*, 46(2):307–313, 2008.

[99] S. Chervenkov, X. Wu, J. Bayerl, A. Rohlfes, T. Gantner, M. Zeppenfeld, and G. Rempe. Continuous centrifuge decelerator for polar molecules. *Physical Review Letters*, 112(1):013001, 2014.

[100] A. K. Hansen, O. O. Versolato, L. Klosowski, S. B. Kristensen, A. Gingell, M. Schwarz, A. Windberger, J. Ullrich, J. R. Crespo Lopez-Urrutia, and M. Drewsen. Efficient rotational cooling of coulomb-crystallized molecular ions by a helium buffer gas. *Nature*, 508(7494):76–79, 2014.

[101] S. Willitsch. Molecular physics: Very cool molecular ions. *Nature Physics*, 6(4):240–241, 2010.

[102] D. Egorov, T. Lahaye, W. Schöllkopf, B. Friedrich, and J. M. Doyle. Buffer-gas cooling of atomic and molecular beams. *Physical Review A*, 66:043401, 2002.

[103] N. Kiesel, F. Blaser, D. Deli, U.and Grass, R. Kaltenbaek, and M. Aspelmeyer. Cavity cooling of an optically levitated submicron particle. *Proceedings of the National Academy of Sciences*, 2013.

[104] J. Gieseler, B. Deutsch, R. Quidant, and L. Novotny. Subkelvin parametric feedback cooling of a laser-trapped nanoparticle. *Physical Review Letters*, 109:103603, 2012.

[105] E. W. Schlag, J. Grotemeyer, and R. D. Levine. Do large molecules ionize? *Chemical Physics Letters*, 190(6):521 527, 1992.

[106] C. H. Beckercor and K. J. Wufn. On the photoionization of large molecules. *Journal of the American Society for Mass Spectrometry*, 6(10):883–888, 1995.

[107] M. Marksteiner, P. Haslinger, H. Ulbricht, M. Sclafani, H. Oberhofer, C. Dellago, and M. Arndt. Gas-phase formation of large neutral alkaline-earth metal tryptophan complexes. *Journal of the American Society for Mass Spectrometry*, 19(7):1021–1026, 2008.

[108] J. Tüxen, S. Eibenberger, S. Gerlich, M. Arndt, and M.Mayor. Highly fluorous porphyrins as model compounds for molecule interferometry. *European Journal of Organic Chemistry*, 2011(25):4823–4833, 2011.

[109] J. Tüxen. *Highly Fluorinated Model Compounds for Matter-Wave Interferometry*. Phd.thesis, 2012.

[110] N. L. Stock, D. A. Ellis, L. Deleebeeck, D. C. G. Muir, and S. A. Mabury. Vapor pressures of the fluorinated telomer alcohols limitations of estimation methods. *Environmental Science and Technology*, 38(6):1693–1699, 2004.

[111] P. J. Krusic, A. A. Marchione, F. Davidson, M. A. Kaiser, C.-P. C. Kao, R. E. Richardson, M. Botelho, R. L. Waterland, and R. C. Buck. Vapor pressure and intramolecular hydrogen bonding in fluorotelomer alcohols. *The Journal of Physical Chemistry A*, 109(28):6232–6241, 2005.

[112] O. Kostko, L. K. Takahashi, and M. Ahmed. Desorption dynamics, internal energies, and imaging of organic molecules from surfaces with laser desorption and vacuum ultraviolet (VUV) photoionization. *Asian Journal of Chemistry*, 6(11):3066, 2011.

[113] S. Deachapunya, A. Stefanov, M. Berninger, H. Ulbricht, E. Reiger, N. L. Doltsinis, and M. Arndt. Thermal and electrical properties of porphyrin derivatives and their relevance for molecule interferometry. *The Journal of Chemical Physics*, 126(16):164304, 2007.

[114] A. D.-Wlodarczak, M. Mullneritsch, T. Juffmann, C. Cioffi, M. Arndt, and M. Mayor. Immobilization of zinc porphyrin complexes on pyridine-functionalized glass surfaces. *Langmuir*, 26(13):10822–10826, 2010.

[115] S. Eibenberger, S. Gerlich, M. Arndt, J. Txen, and M. Mayor. Electric moments in molecule interferometry. *New Journal of Physics*, 13(4):043033, 2011.

[116] P. Dupuis, R. Roberge, and C. Sandorfy. The very low ionization potentials of porphyrins and the possible role of rydberg states in photosynthesis. *Chemical Physics Letters*, 75(3):434–437, 1980.

[117] A.C. Jones, M. J. Dale, G. A. Keenan, and P. R. R. Langridge-Smith. Photoionisation and photodissociation of laser-vaporised metallotetraphenylporphyrins. *Chemical Physics Letters*, 219(3):174–180, 1994.

[118] M. J. Dale, K. F. Costello, A. C. Jones, and P R. R. LangridgeSmith. Investigation of porphyrins and metalloporphyrins using twostep laser mass spectrometry. *Journal of Mass Spectrometry*, 31(6):590–601, 1996.

[119] J. B. Morris and M. V. Johnston. Multiphoton ionization of transition-metal tetraphenylporphines. Metal complexes which display molecular ionization. *International Journal of Mass Spectrometry and Ion Processes*, 73(1):175–180, 1986.

[120] S. C. Khandelwal and J. L. Roebber. The photoelectron spectra of tetraphenylporphine and some metallotetraphenylporphyrins. *Chemical Physics Letters*, 34(2):355–359, 1975.

[121] L. Hanley, P. D. Edirisinghe, W. F. Calaway, I. V. Veryovkin, M. J. Pellin, and J. F. Moore. 7.87 ev postionization of peptides containing tryptophan or derivatized with fluorescein. *Applied Surface Science*, 252(19):6723–6726, 2006.

[122] P. D. Edirisinghe, J. F. Moore, W. F. Calaway, I. V. Veryovkin, M. J. Pellin, and L. Hanley. Vacuum ultraviolet postionization of aromatic groups covalently bound to peptides. *Analytical Chemistry*, 78(16):5876–5883, 2006.

[123] M.-H. Ha-Thi, N. Shafizadeh, L. Poisson, and B. Soep. First observation in the gas phase of the ultrafast electronic relaxation pathways of the S2 states of heme and hemin. *Physical Chemistry Chemical Physics*, 12(45):14985–14993, 2010.

[124] D. O'Hagan. Understanding organofluorine chemistry. An introduction to the CF bond. *Chemical Society Reviews*, 37(2):308–319, 2008.

[125] I Pocsik. Lognormal distribution as the natural statistics of cluster systems. *Zeitschrift für Physik D Atoms, Molecules and Clusters*, 20(1):395–397, 1991.

[126] D. S. Anex, M. S. de Vries, A. Knebelkampl, J. Bargonf, H. R. Wendt, and H. E. Hunziker. Resonance-enhanced two-photon ionization time-of-ight spectroscopy of cold peruorinated polyethers and their external and internal van der waals dimers. *Time-of-Flight Mass Spectrometry and its Applications*, 131:319–334, 2012.

[127] X. Lou, J. L. J. Van Dongen, and E. W. Meijer. Generation of CsI cluster ions for mass calibration in matrix-assisted laser desorption/ionization mass spectrometry. *Journal of the American Society for Mass Spectrometry*, 21(7):1223–1226, 2010.

[128] D. Hölscher, R. Shroff, K. Knop, M.Gottschaldt, A. Crecelius, B. Schneider, D. G. Heckel, U. S. Schubert, and A. Svato. Matrix free UV aser desorption/ionization (LDI) mass spectrometric imaging at the single cell level: distribution of secondary metabolites of Arabidopsis thaliana and hypericum species. *The Plant Journal*, 60(5):907–918, 2009.

[129] D. S. Peterson. Matrix-free methods for laser desorption/ionization mass spectrometry. *Mass Spectrometry Reviews*, 26(1):19–34, 2007.

[130] R. C. Beavis and B. T. Chait. Velocity distributions of intact high mass polypeptide molecule ions produced by matrix assisted laser desorption. *Chemical Physics Letters*, 181(5):479–484, 1991.

[131] L. V. Zhigilei and B. J. Garrison. Velocity distributions of analyte molecules in matrix-assisted laser desorption from computer simulations. *Rapid Communications in Mass Spectrometry*, 12(18):1273–1277, 1998.

[132] W Ens, Y Mao, F Mayer, and KG Standing. Properties of matrixassisted laser desorption. measurements with a timetodigital converter. *Rapid Communications in Mass Spectrometry*, 5(3):117–123, 1991.

[133] W. Zhang and B. T. Chait. Radial velocity distributions of molecular ions produced by matrix-assisted laser desorption/ionization. *International Journal of Mass spectrometry and Ion Processes*, 160(1):259–267, 1997.

[134] M. Glückmann and M. Karas. The initial ion velocity and its dependence on matrix, analyte and preparation method in ultraviolet matrix-assisted laser desorption/ionization. *Journal of Mass Spectrometry*, 34(5):467–477, 1999.

[135] R. Knochenmuss. Laser desorption/ablation plumes from capillary-like restricted volumes. *European Journal of Mass Spectrometry*, 15(2):189, 2009.

[136] Y. Hu, B. Hadas, M. Davidovitz, B. Balta, and C. Lifshitz. Does ivr take place prior to peptide ion dissociation? *The Journal of Physical Chemistry A*, 107(34):6507–6514, 2003.

[137] M. Wahl and A. Wucher. VUV photoionization of sputtered neutral silver clusters. *Nuclear Instruments and Methods in Physics Research Section B: Beam Interactions with Materials and Atoms*, 94(1):36–46, 1994.

[138] B. Witzel, C. J. G. J. Uiterwaal, H. Schrder, D. Charalambidis, and K.-L. Kompa. Analysis of multiphoton ionization of metal atoms in the saturation regime using subpicosecond KrF laser pulses. *Physical Review A*, 58(5):3836, 1998.

[139] A. Tramer, C. Jungen, and F. Lahmani. *Energy Dissipation in Molecular Systems*. Springer Verlag, 2005.

[140] F. J. M. Hoeben, P. Jonkheijm, E. W. Meijer, and A. P. H. J. Schenning. About supramolecular assemblies of pi-conjugated systems. *Chemical Reviews*, 105(4):1491–1546, 2005.

[141] J.-L. Bredas, D. Beljonne, V. Coropceanu, and J. Cornil. Charge-transfer and energy-transfer processes in π-conjugated oligomers and polymers: a molecular picture. *Chemical Reviews*, 104(11):4971–5004, 2004.

[142] W. B. Davis, W. A. Svec, M. A. Ratner, and M. R. Wasielewski. Molecular-wire behaviour in p-phenylenevinylene oligomers. *Nature*, 396(6706):60–63, 1998. 10.1038/23912.

[143] C. Devadoss, P. Bharathi, and J. S. Moore. Energy transfer in dendritic macromolecules:Molecular size effects and the role of an energy gradient. *Journal of the American Chemical Society*, 118(40):9635–9644, 1996.

[144] A. Nitzan and M. A. Ratner. Electron transport in molecular wire junctions. *Science*, 300(5624):1384–1389, 2003.

[145] S. Wu, M. T. Gonzalez, R. Huber, S. Grunder, M. Mayor, C. Schonenberger, and M.l Calame. Molecular junctions based on aromatic coupling. *Nature Nanotechnology*, 3(9):569–574, 2008.

[146] S. Nimmrichter, P. Haslinger, K. Hornberger, and M. Arndt. Concept of an ionizing time-domain matter-wave interferometer. *New Journal of Physics*, 13(7):075002, 2011.

[147] N. Dörre, J. Rodewald, P. Geyer, P. Haslinger, and M. Arndt. Photofragmentation beam splitters for matter-wave interferometry. *arXiv1407.0919*, 2014.

[148] W.A. de Heer. The physics of simple metal clusters: experimental aspects and simple models. *Reviews of Modern Physics*, 65(3):611–676, 1993.

[149] K. Fuke, K. Tsukamoto, F. Misaizu, and M. Sanekata. Near threshold photoionization of silicon clusters in the 248 to 146 nm region: Ionization potentials for Si_n. *The Journal of Chemical Physics*, 99(10):7807–7812, 1993.

Curriculum Vitae

Personal information

Name	Uĝur Sezer
Date of birth	01.05.1989
Place of birth	Erzincan, Turkey
Parents	Sevim and Ali Ekber Sezer
Citizenship	Austrian
Languages	Zazaki/Kurdish (native), Turkish, German, English and French

Educational history

01/2013	-	current	Master′s thesis with Univ. Prof. Dr. Markus Arndt, University of Vienna: *Beams of high-mass organic molecules for matter-wave interferometry*
10/2011	-	current	Master′s studies in physics at the University of Vienna
10/2008	-	05/2011	Bachelor study at the University of Vienna. Bachelor degree in physics (with distinction). Bachelor study of Mathematics at the University of Vienna.
09/2000	-	06/2008	General Qualification for University Entrance (with distinction) at the BRG Henriettenplatz in 1150 Vienna.
09/1996	-	07/2000	Primary school in Vienna

Work experience

10/2011	-	09/2012	Internship in the research group of Ass. Prof. Dr. Alipasha Vaziri at the Research Institute of Molecular Pathology (IMP) in Vienna.
07/2011	-	10/2011	Internship in the Fraunhofer Institute for Biomoedical Engineering in St. Ingbert in Germany. Supervisor: Dr. Wigand Poppendieck.
02/2011	-	04/2011	Experimental work for the Bachelor′s thesis in the research group of Univ. Prof. Dr. Markus Arndt at the University of Vienna.
08/2008	-	09/2008	Internship at the Department of Biomedical Engineering of the Medical University of Vienna. Supervisor: Ass. Prof. Dr. Christian Kollmann.
05/2007	-	05/2007	Internship in the Max F. Perutz Laboratories at the Department for Medical Biochemistry.

Additional information

Projects	Participation in the COMENIUS-EUTRAMO project for the analysis and improvement of the urban traffic situation in Europe. Three international meetings.
Honors and awards	My thesis for the school-leaving exam in chemistry was awarded with the Max F. Perutz prize for the best final thesis in biochemistry of the year 2008. Title of the work: *Pyrrol, Porphyrine und Pigmentsteine- Die Bedeutung der Pyrrolpigmente im menschlischen Organismus und deren Pathobiochemie am Beispiel der Gallensteinbildung.*